Characterisation and Functionalisation of Mechanically Fractured Graphene Nanoribbons

A thesis presented in partial fulfilment of the requirements for the degree of

Master of Science

in

Nanoscience

at Massey University, Manawatū

New Zealand

Samuel James Brooke

2017

Abstract

Graphene has been heralded as the supermaterial of the future, boasting incredibly high electron mobility, thermal conductivity, and physical strength – all contained within the world's first true 2D material, only a single atom thick. Graphene nanoribbons (GNRs) broaden this potential further by demonstrating width-dependent band gaps due to confinement effects. In addition, the ability to define the edge geometry and dimensions of GNRs allows control over self-assembly of these novel carbon nanostructures. GNR synthesis has been broadly explored in literature, demonstrating both relatively high yields and atomic-scale precision. Rarely, however, are these two criteria achieved in the same technique. Longitudinal unzipping of carbon nanotubes (CNTs) generates large quantities of nanoribbon material at the expense of quality, while techniques such as chemical vapor deposition (CVD) and bottom up synthesis achieve truly astounding quality, but lack scalability.

Recently, the synthesis of highly ordered GNRs with tunable dimensions and unique geometries has been demonstrated using mechanical fracturing of a block of graphite via simple microtomy techniques. This method offers a top-down approach to GNR synthesis providing highly ordered structure on a much larger scale than efforts to date. In this work, this technique has been altered to use a dry-cut method, and the structural and chemical properties of the material obtained therein have been extensively characterised, demonstrating increased quality, structural order, and quantities obtainable. Further, this work has demonstrated the functionalisation of these dry-cut materials both chemically via simple organic chemistries, and non-covalently utilising filamentous bacteriophage as a route towards biofunctionalisation.

Acknowledgements

Firstly, I would like to formally thank my supervisors, Mark Waterland and Jasna Rakonjac, for their support and guidance throughout the many twists and turns of this research. I would also like to thank all my fellow groupmates, for their assistance and advice throughout this project.

I would like to acknowledge the expertise provided by Jordan Taylor, in understanding and adapting the microtomy-based techniques discussed herein, and the patience and effort spent analysing countless TEM samples.

I would like to acknowledge Ashley Way, for providing me with computational data, Ewan Fisher for running SEIRAS on all my samples, and Haidee Dykstra for her contributions from, and complex analysis of, the Raman data obtained from these mechanical fracturing techniques. Additionally, I would like to thank Callum Hill and Harry Deare for their efforts in refining the SLIPSERS protocols, which were invaluable during my final data collections.

Lastly, I would like to thank my friends and family for supporting me throughout the project, particularly in the last months. I would not have come this far without them.

Table of Contents

Table of Figures

Abbreviations

2D	Two-dimensional
3D	Three-dimensional
AFM	Atomic force microscopy
CA	Cysteamine
$CHCl_3$	Chloroform
CNT(s)	Carbon nanotube(s)
CTAB	Cetyltrimethylammonium bromide
CVD	Chemical Vapor Deposition
DCC	N,N'-dicyclohexylcarbodiimide (catalyst)
DCM	Dichloromethane
DMAP	4-dimethylaminopyridine (catalyst)
DMF	Dimethylformamide
EDC	1-ethyl-3-(3-dimethylaminopropyl)carbodiimide (catalyst)
EtOH	Ethanol
FET	Field effect transistor
GNB(s)	Graphene nanoblock(s)
GNR(s)	Graphene nanoribbon(s)
GNR-CA	Graphene nanoribbons, cysteamine modified
GNR-MPA	Graphene nanoribbons, 3-mercaptopropionic acid modified
GO	Graphene oxide
GO-CA	Graphene oxide, cysteamine modified
GONR(s)	Graphene oxide nanoribbon(s)
GONR-CA	Graphene oxide nanoribbons, cysteamine modified
GQD(s)	Graphene quantum dot(s)

H_2O	Water
H_2O_2	Hydrogen peroxide
H_2SO_4	Sulfuric acid
H_3PO_4	Phosphoric acid
HEPES	4-(2-hydroxyethyl)-1-piperazineethanesulfonic acid (buffer)
HOPG	Highly oriented pyrolytic graphite
I_D:I_G	Ratio of intensities of D band to G band
IPA	Isopropyl alcohol
IR	Infrared spectroscopy
$KMnO_4$	Potassium permanganate
$LiAlH_4$	Lithium aluminium hydride
LPE	Liquid-phase exfoliation
MD	Molecular dynamics
MeCN	Acetonitrile
MPA	3-mercaptopropionic acid
MQ	Milli-Q® $>$ 18 MΩ grade H_2O
MWNT(s)	Multi-walled carbon nanotube(s)
$NaBH_4$	Sodium borohydride
NHS	N-hydroxysuccinimide (catalyst)
PDC	Pyridinium dichromate
Phage	Filamentous bacteriophage
PMMA	Poly(methyl methacrylate)
Raman	Raman spectroscopy/microscopy
rpm	Revolutions per minute
SDBS	Structural Database for Organic Compounds

SEIRS	Surface enhanced infrared spectroscopy
SLIPSERS	Slippery liquid-infused porous surface-enhanced Raman scattering
TEM	Transmission electron microscopy
THF	Tetrahydrofuran
UV-vis	Ultraviolet/visible spectroscopy
ZYA	High-grade HOPG with mosaic spread of $0.4° \pm 0.1°$
ZYB	Medium-grade HOPG with mosaic spread of $0.8° \pm 0.2°$
ΔG	Change in Gibbs energy
ΔH	Change in enthalpy
ΔS	Change in entropy
κ	Thermal conductivity in $Wm^{-1}\ K^{-1}$

Chapter 1: Introduction

1.1 Graphene

Graphene has been heralded as a super-material of modern science and technology. Its composition is unremarkable; a simple 2D hexagonal lattice of sp^2-hybridized carbons, yet it exhibits truly remarkable properties. These include incredibly high electrical conductivity, thermal conductivity, and mechanical strength, which have identified it as an ideal base material for a variety of electronic and structural applications.[1] Further, it exhibits an array of exotic quantum effects which has enabled their study via simple bench-top experiments.[2-3] Consequently, there is an impressive amount of literature focused on the applications of graphene in energy storage,[4] filtration technologies, and chemical and biological sensor technologies,[5-6] typically boasting next-generation capabilities.[7-11]

1.2 Graphene Nanoribbons

Graphene Nanoribbons (GNRs) are thin strips of graphene (see Figure 1. 1b) which offer additional unique properties. GNRs exhibit band gap energies inversely proportional to their widths – a feature which has been a highlight of the literature due to

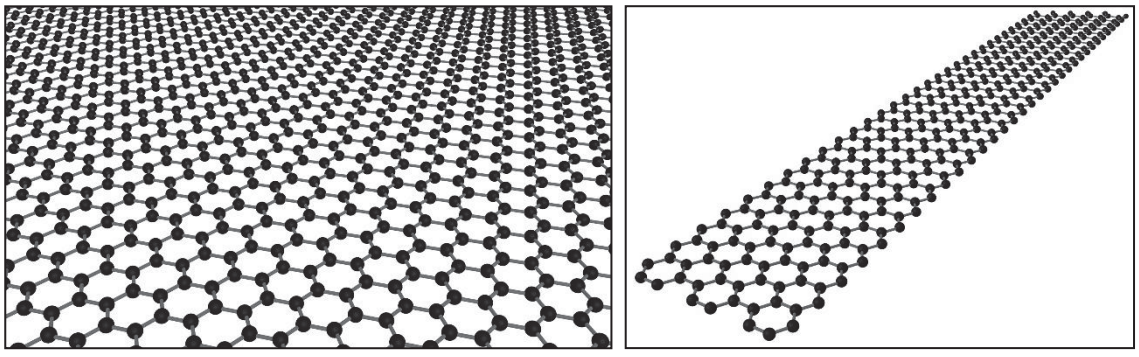

(a) **(b)**

Figure 1. 1 - 3D models of graphene (a) and a graphene nanoribbon (b).

its potential applications in transistor devices. GNRs can be synthesised via a range of techniques;[12-15] the advantages and disadvantages of which are discussed below.

1.3 Technological Significance

Graphene technologies have come a long way in the past 12 years, but two major factors currently limit graphene's incorporation into modern technologies.

First is the seemingly inverse relationship between quantity and quality of material. The physical, electronic, and thermal properties of graphene are all perturbed by material defects.[16-17] Many methods[18-19] can generate large quantities of graphene, but defects are often introduced. The resultant low-quality material is not suitable for long-term or high-performance applications. Conversely, some methods are very good at generating ultra-high quality, pristine material,[15, 20] but these techniques are limited by yields and scalability, not to mention transfer defects which result from the manipulation of material during device integration.

The second major factor is device fabrication and scaling, which is more important for high-performance applications where nanoscale control of design elements is required in high densities. For example, high-performance logic devices such as transistors and nano-circuitry require the highest quality material with nanoscale dimensions and atomic smoothness, densely packed into highly-ordered arrays. Lithographic and CVD techniques have become very proficient in this regard, but the level of control in transferring material without defects, and graphene engineering with appropriate precision on such scales, is simply not feasible with current technologies. Self-assembly might offer a solution, as it provides a means to achieve ordered configurations on larger scales. The field of energy storage has made excellent use of graphene products via simple self-assembly processes to fabricate composite electrodes and supercapacitors with vastly improved performances.[4, 21-22]

1.4 Physical, Thermal, and Electronic Properties

Graphene was originally conceived as a base unit of graphite and other fullerenes, and was first theoretically explored in 1947.[23] Yet early work concluded the material would be thermodynamically unstable as a single 2D layer, and hence its isolation was not considered possible under ambient conditions.[24] Rather, based on our understanding today is quite possible that every time a person takes pencil to paper, they are unknowingly generating small quantities of several, and perhaps even single-layer graphene. While reports of graphene-like properties appeared as early as 1962,[25] Novoselov and Geim provided the first definitive evidence for graphene in 2004.[24] The isolation of graphene allowed for extensive experimental probing of the material's unique properties, and allowed the study of largely unexplored physical phenomena such as the quantum Hall effect at room temperature[2] and the Klein paradox.[3] Since then graphene research has exploded; the number of articles featuring graphene each year has increased exponentially, with over 80% of the now 100,000 publications (since 1991) coming from the last 5 years alone. Graphene-containing products are already commercially available, utilising its unique properties for basic thermal and mechanical applications.[26-27]

1.4.1 Physical Properties

Graphene was the first true 2D material to be experimentally isolated, and sparked interest in other 2D materials such as molybdenum disulfide[28] and silicene.[29] As a 2D material graphene has a very high theoretical Specific Surface Area of $2630\ m^2\ g^{-1}$, similar to that of activated carbon (which is processed with oxygen to increase porosity).[30] Graphene is also unique in that while it has long range crystalline order, the sheets do not lie perfectly flat in a single plane, but instead have intrinsic microscopic roughening due to out-of-plane deformations.[31] These observed corrugations in 3D space may provide

reasons for the material's 2D stability, as a perfect 2D sheet would indeed be thermodynamically unstable.[32] Furthermore, when placed on a substrate such as insulating SiO_2, the graphene mostly conforms to the surface topology,[33] while its intrinsic stiffness prevents complete conformation. It was found that the energy stored in graphene's topological conformation due to the intrinsic stiffness was much less ($\sim$6 times) than the interaction energy between the graphene layer and the SiO_2, favouring the conformation to the surface over its own, free-standing corrugations.

AFM (Atomic Force Microscopy) studies using tips of varying radii probed the mechanical properties of graphene monolayers suspended over lithographically indented silicon holes.[34] They found a breaking strength of $42\,\mathrm{N}$, Young's modulus of $E = 1.0\,\mathrm{TPa}$, and intrinsic strength of $130\,\mathrm{GPa}$. For comparison, the strongest steel has a breaking strength of approximately $1.2\times10^{9}\,\mathrm{N\,m^{-1}}$, which when scaled to the thickness of graphene ($3.35\times10^{-10}\,\mathrm{m}$) gives a 2D breaking strength of $0.40\,\mathrm{N\,m^{-1}}$,[35] meaning pristine graphene is more than 100 times stronger than the same volume of steel.

The following hypothetical example illustrates the mechanical strength of graphene: consider a hammock made of a single sheet of $1\,\mathrm{m^2}$ pristine graphene. This sheet would be almost invisible (optically transparent), could support a $4\,\mathrm{kg}$ cat, and would weigh only $0.77\,\mathrm{mg}$ (or the weight of one of the cat's whiskers).

Despite its high intrinsic strength, graphene has a relatively low fracture toughness of $4.0 \pm 0.6\,\mathrm{MPa}\sqrt{\mathrm{m}}$ (pre-cracked).[36] It was identified that structural defects in the graphene sheet weaken the material to stress, and can result in mechanical fracturing at much lower forces than the tensile and puncture strengths reported for pristine graphene. In this respect, graphene is both incredibly tough, and surprisingly brittle. It was found that when a defect in the material exists, a sharp and straight crack propagation through the lattice originating at the defect is favoured under external strain, which caused pre-

cracked graphene to fracture and cleave into two sheets with relatively straight edges. Molecular dynamics (MD) simulations investigating this effect describe crack propagation through pristine lattices, and at edge boundaries between crystal domains within a single layer (polycrystalline monolayers). These simulations identify alternate scenarios where propagation occurs favourably through new grains (crossing a domain, transgranular), and favourably around the new domain edges (bypassing the domain, intergranular, depicted in Figure 1. 2). These simulations on polycrystalline graphene reveal insight into the dynamics of the mechanical fracturing of GNRs discussed in this thesis.

Further investigation into fracture toughness found that impact forces of supersonic microprojectiles are rapidly delocalised across multi-layered graphene films. Crack propagation occurs upon penetration, absorbing a significant amount of kinetic energy from the projectile. While ineffective on its own in multi-hit scenarios, the impact absorption and energy dissipation properties make graphene an ideal composite component for light-weight ballistic armours.[37]

1.4.1 Electronic Properties

Graphene has an unusual electronic structure, where the conduction and valence bands meet at the Dirac points, making graphene a zero-gap semiconductor.[38] In a pristine graphene lattice, charge carriers are massless Dirac fermions.[39] Zero effective mass means the particles move relativistically, approximately 300 times slower than the speed of light, and are best described by a 2D analogue of the Dirac equation, rather than the almost ubiquitously used Schrödinger equation in nanomaterials.[40] Electron mobility in graphene is remarkably high – in excess of $200{,}000\ \mathrm{cm^2\ V^{-1}\ s^{-1}}$ at a carrier density of $\sim 2\times10^{11}\ \mathrm{cm^{-2}}$ for perfect lattices suspended high over substrates at low temperatures.[41]

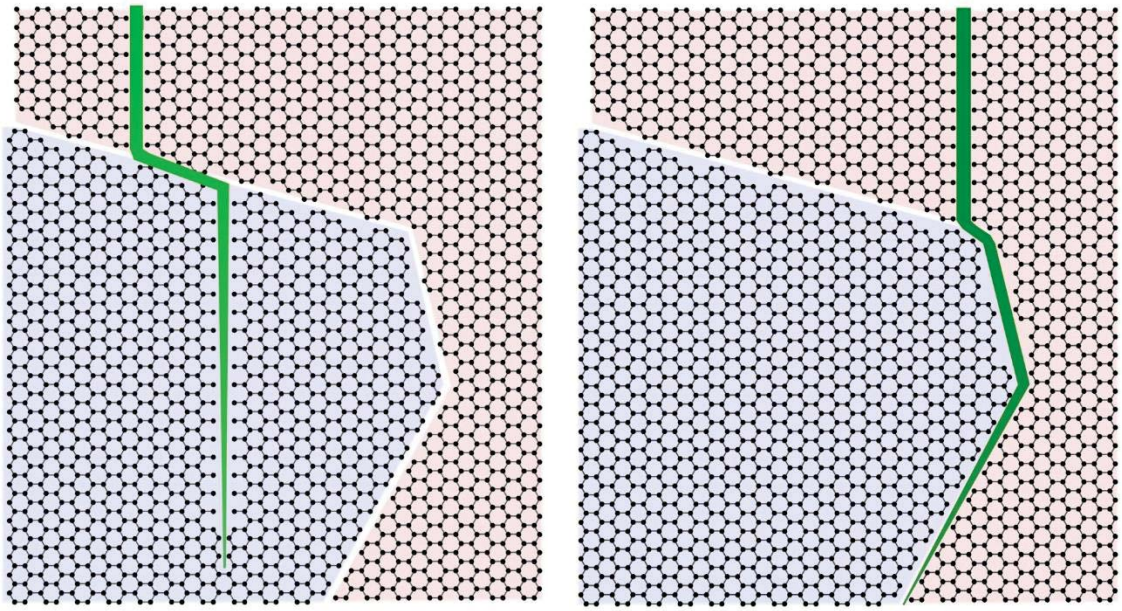

Figure 1. 2 - Schematic representation of fracturing types adapted from Zhang *et al.*[36] (a) Transgranular fracture, (b) intergranular fracture. Red and blue shading indicate distinct domains within a graphene sheet (with the same crystallographic orientation). Green strips indicate direction of fracturing.

This mobility is strongly affected by extrinsic scattering from surface phonons of substrates.[42] Environmental factors also significantly affect mobility due to the 2D nature of the material,[40] as electrons propagate in a medium only one atom thick.

The high carrier mobility makes graphene an ideal material for a range of electronic applications.[16, 40] Consequently, a great deal of effort has gone into inducing band gaps in graphene for transistor devices,[49] using methods such as symmetry breaking,[43-44] uniaxial strain,[45-46] and chemical doping.[47-48] Graphene also exhibits negative differential resistance (NDR) properties which have been utilised in the design of similar transistor devices.[49-50]

1.4.2 Thermal Properties

The thermal conductivity (κ) illustrates another example of how graphene's dimensionality plays a role in its properties. The thermal conductivity of graphene is perturbed by amorphous substrate induced scattering,[51] due to the nature of 2D phonon contributions to κ in graphene. For this reason, a range of thermal conductivities have been reported in literature for both substrate-bound and suspended graphene,[52] ranging from several hundred to an excess of $5000\,\mathrm{Wm^{-1}\,K^{-1}}$. The broad range is also contributed to experimental inaccuracies, but the general consensus regarding the κ of graphene places it above $2000\,\mathrm{Wm^{-1}\,K^{-1}}$, increasing as the number of layers decreases (near $5000\,\mathrm{Wm^{-1}\,K^{-1}}$ at single-layer graphene), making it one of the best room temperature thermal conductors measured (comparable with CNTs). Further, graphene has been shown to demonstrate a length-dependent κ as a result of these phonons, where κ is proportional to the log of its largest dimension.[53] Hence the nature of 2D phonons and how they propagate and interact in graphene is important in understanding its unique properties.

These excellent thermal properties provide immediate applications to micro and nanoscale cooling solutions, such as in high-performance circuits and processor cooling. Experiments using substrates of amorphous SiO_2 to examine the effectivity of graphene as nano-circuitry thermal conductors[51] demonstrate κ values approaching $600\ \mathrm{Wm^{-1}\ K^{-1}}$ – significantly lower than previous reports, but still considerably higher than common thin-film thermal materials used in micro and nanoelectronic systems.[54] For comparison, the κ of copper is $401\ \mathrm{Wm^{-1}\ K^{-1}}$.

1.5 Functionalisation

Functionalisation of graphene and GNRs provides an important mechanism for generating new applications. Graphene has been modified via a range of reactive species to form covalent adducts.[55] Free radicals which attack the sp^2 carbon atoms forming a covalent bond have been utilised from various precursors, such as diazonium salts and benzoyl peroxide,[56-58] thereby introducing functional handles for further modifications. These modifications typically perturb the basal plane which results in a decrease in the material quality.[59] It has been shown, however, that the controlled addition of nitrophenyl groups to graphene's basal plane can induce a band gap, providing a simple route to semiconducting (albeit lower quality) graphene.[60] In addition to radicals, nitrenes,[61-62] carbenes,[63] arynes[64] and dienophiles[65-66] have all been used to introduce a range of functionalities to graphene via covalent attachment to the basal plane. Graphene oxide extends functionalisability by offering a range of chemistries with which to modify the ubiquitous carboxyl,[67-68] hydroxyl, and epoxy[69] residues present therein. These strategies represent more targeted approaches to functionalisation, and provide a basis for the edge-specific functionalisation discussed in later chapters.

Non-covalent functionalisation typically involves interactions of molecules with graphene's basal plane, utilising hydrophobic interactions, π-π stacking, van der Waals

forces, and electrostatic interactions.[70] This can alter physical properties such as solubility and facilitate integration into composite materials without impeding the material's quality.[71] Non-covalent functionalisation allows the manipulation of graphene for a wide range of applications, including the development of electrochemical and electrocatalytic composite films,[72] new materials for solar cells,[73] highly sensitive chemical sensors via binding of analyte-specific graphene-binding peptides,[74] and self-assembled hybrid materials for enhanced energy-storage devices using specifically tailored virus particles.[4]

Bio-functionalisation of graphene allows the utilisation of graphene's unique properties in biotechnologies, advancing current technologies and generating new ones.[75] Graphene has been employed in the detection of cancer biomarkers,[76] the differentiation of stem cells,[77] drug delivery,[78] and much more.[75] With their high aspect ratios (length to width dimensions), GNRs can be utilised as a base for, and component of, self-assembly. GNRs have been used as templates and sensor elements in the assembly of biomolecules for biosensor applications,[5] and for the characterisation and sequencing of DNA molecules.[79] Additionally, basic GNRs self-assembly has been demonstrated in the generation of dense and ordered arrays for supercapacitor[80-81] and energy-storage applications,[82] while more complex self-assembly of GNRs can also be directed via nitrogen-doped analogues (in bottom-up GNR synthesis) for the formation of 2D and 3D metamaterials with unique, tunable optoelectronic properties.[83]

1.6 Graphene Nanoribbons

Owing to their high-aspect ratios, edge structure and confinement effects now play a role in determining the properties of GNRs.[84] The edge structure can take one of two limiting forms – zigzag or armchair (see Figure 1. 3). Armchair edges confer semiconducting properties, with band gap energies inversely proportional to width,[85-87]

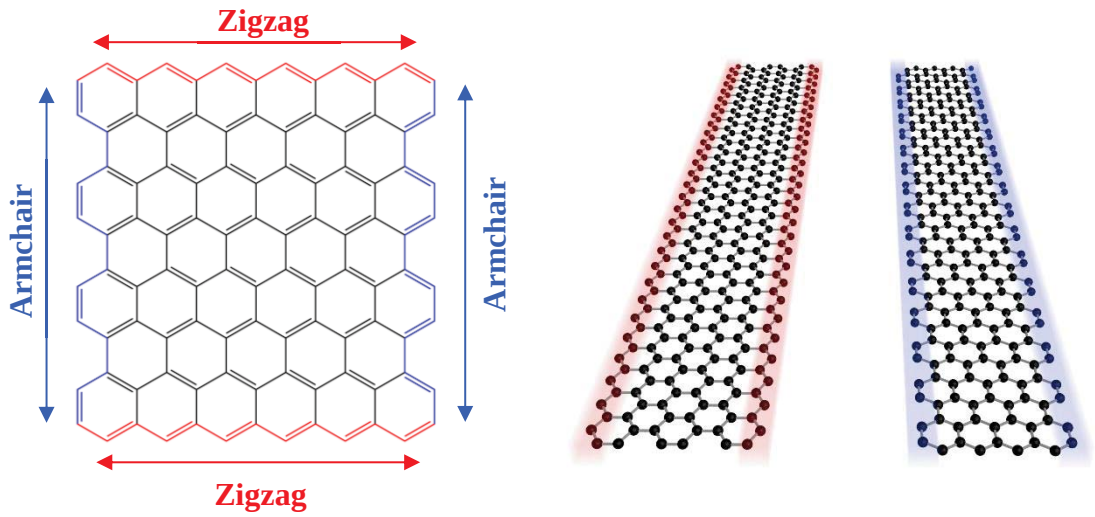

Figure 1. 3 - (a) Schematic diagram and (b) 3D model of graphene and GNR edge types (hydrogen atoms omitted for clarity). Blue indicates armchair and red indicates zigzag edges. Basal plane is in black.

and zigzag edges are predicted to have spin-polarized edge states[88] and half-metallicity.[89] Due to these effects, additional function can be fine-tuned by engineering geometric complexity,[15] with predicted improvements to their thermal[90] and optical properties.[91]

GNRs are uniquely qualified for use in high-performance field-effect transistor (FET) devices due to their width-dependent band gaps,[92-93] and have been identified as a potential solution to overcoming current computational limitations.[50] Consequently, their optimisation in such devices has been a major driving force for GNR literature in both their synthesis and applications.

1.7 GNR Synthesis

1.7.1 Carbon Nanotube Unzipping

The first reported large-scale synthetic route to graphene nanoribbons was CNT unzipping.[12] These methods use a strong acid and an oxidiser to selectively cleave CNTs longitudinally by attacking a defect in the tube. Once attacked, the longitudinal "unzipping" is a thermodynamically favourable process (potentially due to the topological strain and the same mechanism as the crack formation mentioned earlier[36]),

resulting in relatively uniform GNRs. The unzipped GNRs can then be treated via H_2 annealing or reduction by hydrazine (N_2H_4) to improve the quality of the oxidised material.

Homogeneity of the resultant sample is dependent on the homogeneity of the starting material (i.e. how pure/uniform the CNTs are), and multi-walled nanotubes (MWNTs) will always produce a range of widths. Furthermore, the unzipping treatment is relatively harsh, and it is important to optimise reaction time to maximise the GNR yield without damaging the material beyond practical use. Adaptations and improvements to the technique have been demonstrated in literature, such as the generation of additional geometries (rectangles and squares) via an additional radial cleavage step,[94] and improvements to reaction times and quality obtained using ions as catalysts.[95]

It has been demonstrated that GNRs synthesised this way can be efficiently utilised for supercapacitors[21] owing to the homogeneity achievable with pure starting materials and improved quality post annealing. Potential applications have also been demonstrated as a protectant to improve both cyclic lifetimes of $LiMn_2O_4$ electrode materials and their overall performances.[22] While longitudinal unzipping of CNTs provides a relatively simple route to large quantities of GNRs, purity and GNR dimensions are entirely dependent on the starting materials, and the quality of the final material is significantly impaired due to the oxidative processes.

1.7.2 Chemical Exfoliation

An interesting route to GNR synthesis, this method of chemical exfoliation uses polymers and sonication to induce cleavage of graphene flakes into ribbon-like structures.[13] Exfoliation of commercially available graphite is achieved by intercalation of nitric and sulfuric acid between graphite layers, then rapid heating to 1000 °C causing violent expansion the intercalated acid. This process introduces defects which are utilised

in subsequent steps. The exfoliated graphene is then purified and suspended in a solution of 1,2-dichloroethane (DCE) with the polymer, poly(m-phenylenevinylene-co-2,5-dioctoxy-p-phenylenevinylene)(PmVP), which is known to interact with CNT walls via π-π stacking. The suspended solution is then treated to further harsh exfoliation to induce cleavage at defect sites, while the polymer is suspected to strengthen sections of the flakes so that scission occurs along a straight edge. This results in a number of ribbon-like structures, relying on random interactions and the structural effects of the polymer to drive nanoribbon formation. Alongside nanoribbons, a number of distinct structures were reported, including tapered structures and ribbons with boomerang-like kinks which indicate a change of shearing direction through the sheet. Again, the fracture toughness of graphene[36] is likely involved with the driving forces responsible for GNR formation. FETs were fabricated, and sub-10 nm sections showed semiconducting behaviours, but with lower than anticipated performances.

This method demonstrates the use of sonication for the directed scission of graphene precursors to generate an inhomogeneous mixture of relatively low concentration and geometrically unique GNRs. It is also possible that the material quality itself is of poor quality (insufficient quality data), due to the harsh exfoliation treatments and deliberate introduction of defects.

1.7.3 Lithographic Synthesis

Lithographic synthesis of GNRs is a versatile method which uses a masking then etching process to design and generate a range of different shapes, widths and crystallographic orientations.[92-93] The general principal uses a mask covering the material of interest (graphene sheets or flakes) that can be modified to either cover or expose sections of graphene (such as with electron-sensitive films (resist) in e-beam lithography). The mask is patterned into lines and etched with a plasma, which removes only the

revealed areas of graphene not covered by the mask. When the mask is removed, GNRs are left behind.

These methods can generate GNRs below 10 nm in width, but the edge quality of the material is generally poor, irrespective of their size. FETs demonstrated using this material[92] show band gaps inversely proportional to their widths, but suffer from poor overall performances as a result of the irregular edge structures.

Another method shows high-quality edge structures can be generated using CNT precursors embedded in a film of PMMA.[96] The CNTs are applied to a smooth surface, then covered in a film of PMMA. The film is then inverted, exposing a small section of the sidewall at the surface, and etched using a low power Argon plasma. The results demonstrated higher quality material and greater precision than standard lithographic methods, but introduce a dependence on CNT starting material. Regardless, they demonstrated a relatively high degree of width tunability by controlling the type of starting material and etching times. This method could be considered an improved unzipping technique that affords better control and higher quality material, but with lower, lithographically-relevant yields.

Lithography, therefore, is a versatile GNR synthesis tool which can generate any type of shape or pattern desired. The quality of the material is generally high (also dependent on starting material), unless dealing with low widths, due to poor edge quality. Its drawbacks are low yields and residual resist or mask contaminants which, unless thoroughly cleaned, perturb the quality of the material.

1.7.4 Chemical Vapour Deposition (CVD)

Like graphene sheets, GNRs can also be grown via CVD by applying selection criteria to the growth process. This method gives a large degree of control over the patterning of graphene, but instead of etching away from a pristine sheet as in lithographic

methods, it builds up pristine graphene in discrete sections, providing (generally) higher quality material. Few-layer GNRs have been made using templated CVD on a zinc sulfide (ZnS) nanoribbon catalyst,[14] and a similar "barrier guided growth"[97] method which confines catalytic areas by depositing pacifying AlO_2 in patterns. This technique is capable of generating 5 nm feature sizes and 1 nm lateral resolutions.

Nanostructures of catalytic material can also be used to direct the growth of GNRs and patterned graphene.[98] One such method utilises a nickel nano-bar to grow 23 nm wide GNRs directly onto source and drain electrodes for immediate transistor device integration, demonstrating high mobilities but small band gaps due to their (relatively) large widths.

It is also possible to create highly-ordered graphene composite materials by lithographically etching one material and growing graphene in the gaps. This was demonstrated with hexagonal boron nitride/graphene nanocomposites which displayed unique hybrid properties.[99]

Recently, the controlled synthesis of GNRs on germanium wafers has been demonstrated using a slow-growth technique,[20] which is capable of synthesising large numbers of GNRs down to sub-10 nm widths, with near atomically smooth armchair edges. This technique demonstrates the ability to grow near-perfect quality GNRs via CVD in a scalable manner, and can be synthesised directly onto a technologically relevant substrate for electronic devices.

CVD offers a high degree of flexibility in the patterning and design of graphene and GNRs, with high qualities and appreciable lateral resolutions. The high quality, large sheets that can be obtained from this method make it a popular choice in graphene research, but it generally falls short for practical applications due to the cost and low yields. However, the use of patterning and templating for GNR synthesis provides a

means of scalability, and recent advances demonstrate precise edge structures comparable to those of organic synthetic routes.

1.7.5 Thermal Decomposition

Thermal decomposition uses a silicon carbide (SiC) substrate heated up to a graphitization temperature around 1300 °C, whereupon the silicon atoms sublime, leaving a carbon-rich interface from which graphene is able to grow.[100] Like CVD, masks with patterns can be applied to protect the SiC from sublimation and direct the synthesis of defined shapes and strips for GNRs. It has also been demonstrated that the thermal decomposition is catalysed by gold and silicon implantation on the SiC surface,[101] which lowers the graphitization temperature and can be applied in a controlled manner. Carbon ions have also been used to catalyse thermal decomposition in this manner.[102] The catalyst approach allows the synthesis of defined GNRs as small as tens of nanometers, directly onto a technologically-relevant substrate without the need for masking materials like lithographic and CVD methods. Therefore, while other techniques have more precision and can generate higher quality material, these methods offer the potential for direct integration of graphene materials in device fabrication.

1.7.6 Bottom-Up Chemical Synthesis

GNRs can be synthesised with high quality and tunable widths using well-defined organic synthetic approaches.[15, 103-104] Suzuki-Miyaura coupling and subsequent polymerisation via cyclodehydrogenation has been utilised to generate GNR derivatives with modified (increased solubility),[104] and unmodified edges[103] using complex and simple polyphenylene-like precursors. Surface-assisted coupling of halogenated precursor monomers is capable of synthesising well-defined, sub-10 nm, atomically precise and defect-free GNRs,[15] with widths and edge structures defined by the precursor molecules.

These synthetic methods can synthesise high purity, perfect quality sub-10 nm GNRs, demonstrating perhaps the most controlled synthetic capabilities of all the methods discussed herein. Drawbacks of these methods include the reliance on surface-assisted chemistry, potentially low yields as a result, and the need to transfer the material post-synthesis (thereby inducing defects).

1.7.7 Mechanical Fracturing

In 2012, a paper was published that outlined and demonstrated a technique for mechanically fracturing GNRs of high quality from a block of HOPG using a diamond knife mounted in a microtome.[105] This technique can produce a wide range of nanostructured graphene materials, including graphene nanosquares, nanoribbons, nanotriangles and quantum dots. The graphene generated is typically very high quality with relatively smooth edge structures, and can achieve sub-10 nm widths. The quality of the material and its edges, and homogeneity of the samples are dependent on the cutting conditions (speed, alignment, knife-sharpness), and optimisation of these parameters can result in very well-defined, homogenous samples (see chapter 3). This technique allows the synthesis of highly-ordered, precisely controlled graphene nanoribbons via a relatively simple method.

This technique is the basis for the research contained herein, where modifications to this technique provide significantly higher quality, yields and edge smoothness.

1.8 Summary

Graphene is a remarkable material, exhibiting incredible physical, thermal and electronic properties, all packaged into a layer only a single atom thick. GNRs expand upon these properties, introducing unique quantum phenomena resulting from confinement effects. Due to their widescale applicability to modern applications, there is a clear and present desire in literature to find methods which can synthesise large

quantities of high-quality graphene, and to find ways to functionalise it while maintaining this quality. This chapter has outlined an introduction and background to graphene nanomaterials with an emphasis on graphene nanoribbon synthesis and applications, and the challenges associated therein.

1.9 Research Aims

The initial aim of this research was to investigate the functionalisation of GNRs with filamentous bacteriophages for the synthesis of novel hybrid nanomaterials. However, the discovery of an improved mechanical fracturing technique and the insights gained from functionalisation attempts led to a shift in focus towards the characterisation of the materials generated via this method. The aims then became to characterise the quality, geometries, and edge chemistries of GNRs synthesised via mechanical fracturing in air, and to investigate their functionalisation via edge-directed chemistry.

Characterisation of materials generated provided insights to the mechanical fracturing process, and assisted in the optimisation of the synthetic technique. In addition, characterisation also provided a foundation for the functionalisation experiments which were based on the specific chemical identities at the GNR edges. Functionalisation was then demonstrated using both edge-specific, covalent functionalisations and non-covalent, basal plane functionalisation with filamentous bacteriophage, in honour of the initial aims of this research and as a foundation for future research into GNR-phage hybrid materials.

1.10 Thesis Outline

1.10.1 Chapter 2

This chapter details the experimental methods used throughout the work presented in this thesis. It provides specific details of the mechanical fracturing setup, and protocols

for GNR processing and chemical modifications. The purpose of this chapter is to enable the reader to replicate the mechanical fracturing processes and experimental techniques of this work.

1.10.2 Chapter 3

This chapter explores the mechanical fracturing of GNRs with respect to experiments in literature and the theory around graphene fracture strengths. This chapter describes in detail the experimental technique of both wet and dry-cut fracturing. Experimental insights gained from this research are presented and discussed in the context of the fracturing literature, and of characterisation results presented in chapter 4. This chapter aims to establish a clear understanding of the improved dry-cut fracturing method, and the challenges associated with generating high-quality, ordered GNRs.

1.10.3 Chapter 4

This chapter explores the characterisation of dry-cut GNRs using a number of techniques to provide a clear understanding of the type of material this technique generates. AFM and TEM (Transmission Electron Microscopy) are used to probe the general shapes and geometric properties of the GNRs, revealing well-defined edges and high-flexibility consequential of their aspect ratios. Raman spectroscopy and infrared spectroscopy (SEIRS) provide insights into the quality and chemical functionalities of these GNRs respectively, demonstrating notably high overall material and edge quality, and unique edge chemical functionalities. UV-vis spectroscopy is used to investigate the solubility of GNRs in various common solvents, and scission (post-synthetic fracturing or tearing) of GNR material is illustrated via TEM and discussed in the context of sonication and its effects on material quality.

1.10.4 Chapter 5

This chapter explores the functionalisation of GNRs using covalent and non-covalent strategies. These involve using reductive and oxidative treatments to enable edge functionalisation via Steglich esterification and amidation reactions, based on the insights obtained from characterisation results discussed in chapter 4. The difficulties associated with characterising these modifications are discussed, and solutions to these problems are presented via enhanced spectroscopic techniques and reporter techniques using TEM. The successful functionalisation of GNR materials with thiol-bearing moieties is demonstrated via the selective binding of AuNps and changes to SEIRS spectra. An aggressive oxidative strategy is employed to provide enhanced functionality to the GNRs, which results in highly-selective edge-specific functionalisation, but at the cost of general material quality. The potential for optimisation of oxidative protocols to improve functionality whilst maintaining this quality is discussed. Non-covalent, basal plane functionalisation is also demonstrated as an alternative route to functional materials, utilising charge-based interactions with filamentous bacteriophage to provide highly-functionalised GNRs while maintaining material quality. The challenges associated with achieving this level of functionalisation and the potential for future research using these materials is discussed.

Chapter 2: Methods and Materials

2.1 Mechanical Fracturing Setup

The setup is critically important for assuring high-quality GNR materials. A poor cut will increase edge roughness and flake-impurities. Microtome setup as follows:

- Diamond knife included angle fixed at 45°
- 5° clearance angle
- Chuck-holder angle as necessary
- Pivot angle as necessary

Angles depicted in Figure 2. 1. The included angle of the diamond knife is the angle of the receding knife shape, and is therefore fixed at the manufactured angle, in this case, 45°. The clearance angle is the angle between the planes of the back edge of the knife and the cutting face. This angle provides spacing between the knife and block face to allow sufficient clearance of the block as it travels past the knife edge, which prevents potential damage to either element. The chuck-holder angle is altered when first aligning the block, and when adjusted will produce thin or tapered GNRs until the block face is levelled. The pivot angle controls the rotation of the knife edge around a vertical axis (i.e. cutting direction) with respect to the block face. It is rarely altered, but small changes during alignment can facilitate a smooth cut through the block.

2.2 Cutting Parameters

Cutting speeds are typically between 0.4 mm s^{-1} and 0.8 mm s^{-1}. Lower cutting speeds are reported by Mohanty *et al.* to give higher quality edges, but previous work by our group (specifically, Haidee Dykstra) noted insignificant changes in the ratio of intensities of Raman ‘D’ and ‘G’ bands (I_D:I_G) for dry-cut samples between these speeds.

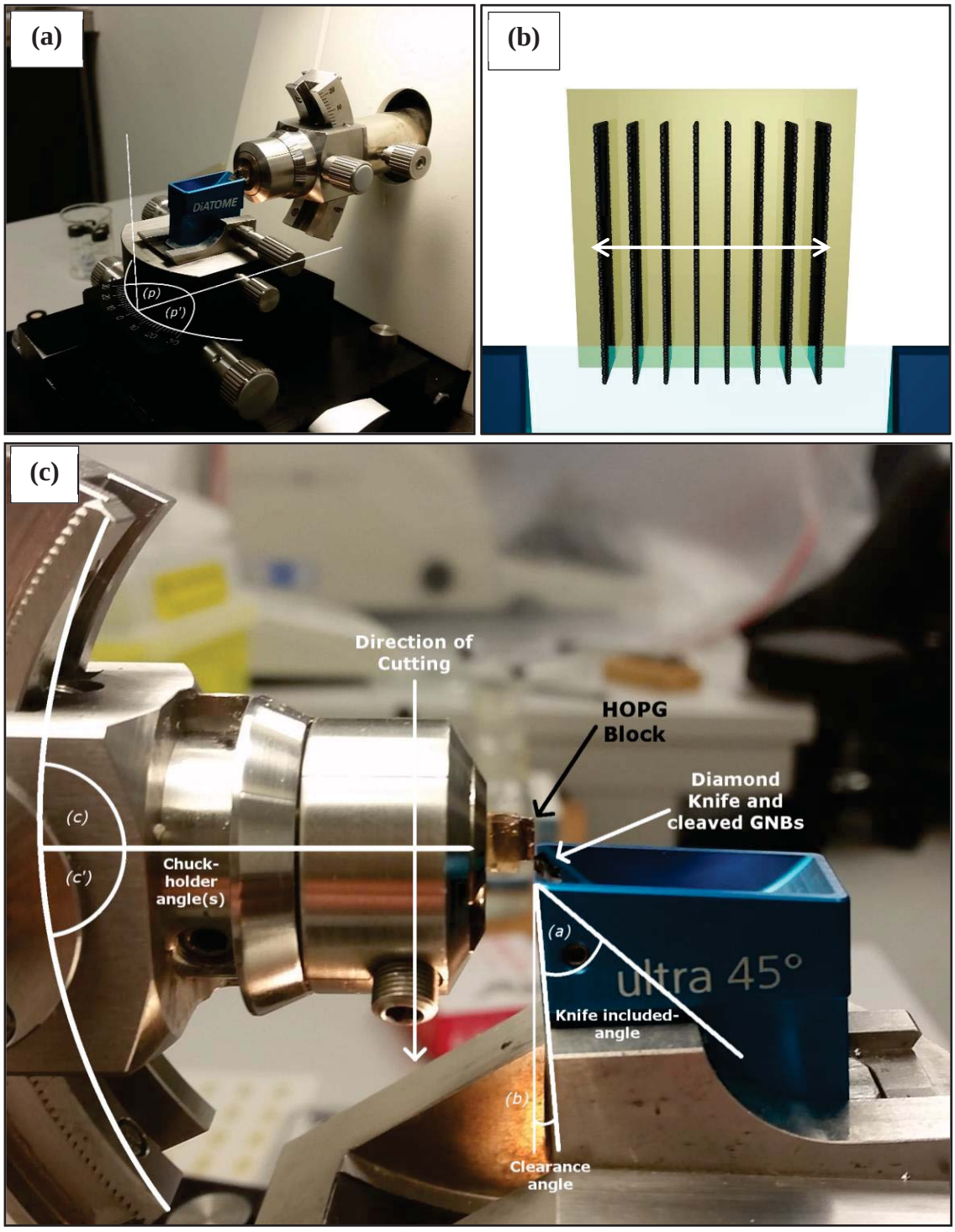

Figure 2. 1 - Microtome setup for mechanical fracturing in air. (a) Microtome apparatus as prepared for fracturing HOPG. Diamond knife and boat mounted in centre of image. Pivot angles displayed as (p/p'). (b) Diagram of cutting face showing orientation of graphitic planes with respect to knife edge (blue section at bottom). Direction of stacking within HOPG indicated by white arrow. (c) Side view of microtome setup with angles overlain: Knife included-angle (a), clearance angle (b), chuck-holder angle(s) (c/c').

The block of HOPG is set in Araldite™ resin and mounted directly into the chuck. The graphite is positioned such that the axis through the stacked basal planes is parallel to the knife edge (see Figure 2. 1b).

The block needs to be trimmed to clean and prepare the block face for cutting. This is done by using a razor blade to cleave off sections of HOPG which are sticking out or loose, so that a clean, rectangular cuboid is produced. The cutting face then needs to be smoothed by manually advancing the microtome wheel. Small tweaks to the pivot and chuck-holder angles may be necessary to achieve efficient cutting.

Yields are dependent on block size and cutting speed (both of which are inversely proportional to material quality/cutting efficiency), but are usually on the order of milligrams per hour. This can theoretically be scaled up using setups which include multiple blocks per knife, and multiple cutting apparatus. Additionally, the inclusion of an automatic collecting mechanism (such as a rotating wheel on the inside edge of the knife) to clear the knife and prevent material folding back would provide a means of long-term automation. The limiting factors for automation would be block-depth, chuck-arm feed, and occasional trimming and maintenance of the block faces.

It is important to maximise cutting efficiency during initial setup, and sufficient time and effort should be dedicated to doing so. An inefficient cut will produce inhomogeneous GNRs and increases the amount of flake impurities. When aligning after this initial setup, the process is relatively mundane, and only requires minor cleaning of the block faces and small changes to the chuck-holder and pivot angles. Nevertheless, sufficient care should be taken to assure the best alignment before cutting on every occasion.

2.3 Instruments and Equipment

Microtome: Leica Ultracut R (Fully Automated). Araldite™ resin is used to fix ZYA or ZYB grade HOPG for cutting.

Diamond Knife: DiATOME Diamond Knife 4 mm 45° EM (Electron Microscopy).

Bath ultrasonicator: Bandelin SONOREX™ Digital 10 P. Modified tap-fed cooling system using copper coils immersed in a salt-ice bath.

Centrifuge: Sigma 1-14 microcentrifuge.

TEM: FEI TECNAI G2 Spirit BioTWIN. Samples prepared on carbon coated and formvar only copper grids.

AFM: Nanosurf easyScan 2, with camera module for scan head. Silicon Tap190DLC and ContAl-G cantilevers were used for tapping and contact mode respectively, purchased from www.budgetsensors.com.

Raman Microscope: Home-built Raman microscope based on an Olympus IX70 inverted fluorescence microscope with 532 nm diode laser excitation. Excitation was directed to the sample by an Iridian Spectral Technologies Raman edge filter or an OptiGrate Volume Bragg bandpass filter and was focused onto the sample with a $NA = 0.65$ ($40\times$ magnification) objective. Typical excitation power at the sample was < 2 mW (to avoid sample damage). Raman scattering was collimated with the same objective and residual Rayleigh scattering was removed with a series of OptiGrate Volume Bragg Notch filters. The Raman scattering was focused into a 50 μm diameter optical fibre and aligned on the entrance of a Princeton LS785 lens spectrograph with detection by CCD camera.

IR Microscope: Nicolet 6700 FT-IR spectrometry with microscope attachment was used to perform absorption measurement in a reflection geometry. An MCT-a

detector was used in conjunction with a KBr beam splitter. Room temperature collection, sample spot size of $\sim 20 \times 20\ \mu m$.

UV-vis spectrometers: Shimadzu UV-3101PC and Sinco S-3100

2.4 Processing

Graphene nanoblocks (GNBs) cleaved from the HOPG can be collected using a simple brush with a single bristle, such as a toothpick and piece of hair. This can then be transferred to a solvent of choice via brief immersion, or into an empty vial by shaking from the brush. The large surface area to mass ratios of these GNBs makes removal from brush easy via a brief shake, but also means care is required when collecting as slight air currents (including moving the GNBs through the air) can suddenly dislodge the sample. The collected samples can then be exfoliated using gentle sonication or any technique of choice.

2.5 Exfoliation

A bath ultrasonicator with variable power outputs ranging from $10 - 100\%$ of $320\ W$ with active heating control was used for exfoliation. The most common parameters were $10 - 20\%$ power at room temperature, for times between 15 minutes and several days. GNR stacks for TEM observation are prepared using 10% power and room temperature for 15 minutes, while the samples in the solvent study (chapter 4.4.1) were sonicated at 50% for 24 hours.

2.6 Centrifugation

Following sonication, purification of GNRs from flakes and unexfoliated debris may be necessary. This is achieved on the basis of mass differentiation by centrifugation at low speeds for long periods of time; typically $500 - 1000\ rpm\ (18 - 73 \times g)$ for 90

minutes. The supernatant, which contains the GNRs, is then pipetted off and the pellet is discarded.

It should be noted that there is often a portion of the sample which remains as GNR stacks, and can be pelleted with the impurities, resulting in lower yields. Conversely, small, well-exfoliated impurities can also remain in solution with the GNRs instead of pelleting. This process is also dependent on solvent systems used for exfoliation, where good solvents require higher speeds to pellet flake impurities, while poor solvents require lower speeds.

2.7 Reaction Workup

Centrifugation is also an important technique for reaction work-up. After functionalisation reactions, GNRs are dispersed in a solution (sometimes precipitated) containing excess reactants and side-products. These are typically solvated, while GNRs are only dispersed and can be pelleted. Therefore, centrifugation is used at high speeds to pellet as much of the GNRs as possible. This is usually done using maximum centrifuge speed ($16162 \times \mathrm{g}$) for $10 - 30$ minutes and is repeated multiple times. This is described herein as "washing" the samples. The material is re-dispersed after each wash to minimise the trapping of impurities within the pellet. GNRs deposit as a pellet or across the side-walls of the centrifugation tubes ($1.5\ \mathrm{mL}$ Eppendorf plastic tubes), but for most circumstances (except where GNRs are highly insoluble in the reaction medium) small quantities of the material are washed away with the discarded supernatant. This can happen if the material is highly soluble (some modifications increase solubility), or when the solvent meniscus is drawn across the side-walls during pipetting, which can draw material off with it into the supernatant. This latter process can be visually observed, especially near the tapered end of the tube. Over the course of several washes, this can result in a substantial loss of product. Conversely, some samples will bind very strongly

to the plastic tubes and can remain stuck even after sonication at maximum power. These effects mean that centrifugation often results in low final yields, and makes multi-step functionalisations difficult to achieve in high quantities.

For reactions in water (EDC-catalysed), dialysis can be used as a purification technique which results in very little product loss. Cellulose dialysis membranes have been used to purify samples in water using passive diffusion (concentration gradient) into a large volume of Milli-Q (MQ) or higher grade water. In most cases, osmotic pressure will cause the dialysis vessel to swell, diluting the sample. Occasionally, a dialysed sample is then taken to a rotary evaporator to reduce this solution back to a practical volume.

2.8 Functionalisation Reactions

Throughout these protocols, exact quantities are often not given due to the difficulties associated with accurately weighing and spectroscopically quantifying GNBs and GNRs, which are outlined in chapter 5. Instead, GNR sample masses are estimated by their time spent cutting before collection, as the size of the block face can be calculated to quantify the graphitic content generated by each cut. This is then checked by observing the colour and opacity of GNR solutions generated. Due to the low number of modifiable edge residues per GNR, there is only $\sim 0.26\ \mu mol$ of edge residues in $1\ mg$ of GNRs (calculations in Appendix 2), and reactions are typically performed on only a few milligrams of GNRs per millilitre. For a 1: 1 molar ratio, this equates to weighing between $54\ \mu g$ and $20\ \mu g$ of reactants per milligram of GNRs, which assumes total edge decoration with modifiable functional groups (such quantities are likely not even achieved with GONR samples). As such, rather than weighing out microgram quantities for each reaction, reactants are simply added in excess where appropriate as a small mound on a spatula tip, or “a few milligrams” as described below.

Most reactions are carried out under constant sonication, as aggregation of GNRs will prevent access by solvated reactants and result in poorly functionalised material.

2.9 Reduction of GNRs

2.9.1 Sodium Borohydride Reduction

1. GNBs were placed in a glass vial and filled with $2-4$ mL of methanol (more for large quantities). This was then dispersed into solution by sonication.
2. Sodium borohydride ($NaBH_4$) was added in excess (a few milligrams).
3. The solution was placed in the sonicator at low power ($10-20\%$) for up to one hour ($NaBH_4$ decomposes before this, and more was added during this time when using large quantities of GNRs).
4. The sample was taken from the sonicator and left to rest at room temperature overnight, which allowed GNRs to precipitate and facilitated the workup.
5. GNRs were washed and purified via centrifugation.

2.9.2 Lithium Aluminium Hydride Reduction

1. GNBs were placed in a glass vial and dispersed in $2-4$ mL of dry tetrahydrofuran (THF) using moderate power sonication ($40-60\%$), then backfilled with argon and sealed with parafilm.
2. In a separate vial, ~ 1 mg of lithium aluminium hydride ($LiAlH_4$) was added to dry THF, which was also backfilled with argon.
3. The solution in step 2 was shaken and added dropwise to the GNR-THF solution on ice.
4. The GNR reaction mixture was backfilled with argon, sealed with parafilm and placed in the sonicator at moderate power with periodic agitation (GNRs have low solubility in THF) for one hour.

5. The sample was removed from the sonicator and left to rest at room temperature overnight.
6. GNRs were washed and purified by centrifugation.

2.10 Oxidation of GNRs

2.10.1 Pyridinium Dichromate Oxidation

1. GNBs were dispersed via moderate power sonication ($40 - 60\%$) in $2 - 4$ mL of dimethylformamide (DMF).
2. Excess pyridinium dichromate (PDC) was added to the solution, which was placed in the sonicator for one hour at low power ($10 - 20\%$).
3. The solution was left to rest at room temperature overnight.
4. The sample was washed and purified via centrifugation.

2.10.2 Hummer's Improved Oxidation

This method was adapted from literature where it is used as an "improved" graphene oxide synthesis method,[106] which was demonstrated to give higher quality and higher yields of graphene oxide over standard Hummer's methods. It generates a range of products, which were purified into fractions based on solubility and exfoliation extent by centrifugation.

1. GNBs were placed unexfoliated in a 50 mL round-bottom flask with potassium permanganate ($KMnO_4$) at a $1:6$ ratio (GNB:$KMnO_4$).
2. 10 mL of $9:1$ concentrated sulfuric acid (H_2SO_4) to concentrated phosphoric acid (H_3PO_4) was added and the flask was placed in the sonicator at 100% power and 50 °C for $1 - 6$ hours (depending on desired oxidation/exfoliation extent).
3. The solution was removed from the sonicator and poured onto ice ($\sim$10 mL) with 200 µL of hydrogen peroxide (H_2O_2).

4. The solution was dialysed into MQ water.
5. Centrifugation was used to isolate various fractions from the sample by incrementally spinning at increasing speeds.

2.11 Thiol Functionalisation

2.11.1 EDC Catalysed Reactions

These reactions require water-dispersible material and as such were only used on GO and GONRs (detergent-stabilised GNRs do not work well as the detergent was found to participate in the reaction, which generated by-products and inhibited functionalisation).

1. A solution of MQ water was buffered with 1M HEPES (4-(2-hydroxyethyl)-1-piperazineethanesulfonic acid) to pH ~7.5.
2. 2 mL of this solution was used to disperse GNRs via brief sonication or mixing, then placed on ice.
3. The sonicator was cooled to 4 °C using ice and a copper coil immersed in a salt-ice bath, through which tap water flowed into the sonicator at a slow rate.
4. A few milligrams each of 1-ethyl-3-(3-dimethylaminopropyl)carbodiimide (EDC), cysteamine hydrochloride (CA), and N-hydroxysuccinimide (NHS) were added to the GNR solution (4 °C) and placed into the sonicator for up to one hour at low to moderate power, depending on the dispersibility of the graphene.
5. The sample was taken from the sonicator and placed in the fridge at 6 °C overnight (leaving overnight gives the reaction time to complete).
6. The sample was removed from the fridge and purified via centrifugation or dialysis.

2.11.2 DCC Catalysed Reactions

These reactions were used on relatively high-quality GNRs which are not water-dispersible.

2.11.2.1 Cysteamine Reaction

1. GNRs (oxidised) were dispersed in $1-2$ mL of DMF.
2. In a separate vial, a N,N'-dicyclohexylcarbodiimide (DCC) and cysteamine were added in excess to $1-2$ mL of DMF.
3. The reaction mixture in step 2 was added to the GNR solution and placed in the sonicator at moderate power for up to one hour.
4. The solution was taken out of the sonicator and left to mix on a shaker or rest at room temperature overnight.
5. The solution was then washed and purified via centrifugation.

2.11.2.2 Mercaptopropionic Acid Reaction

1. GNRs (reduced) were dispersed in $1-2$ mL of DMF.
2. In a separate vial, excess DCC and 4-dimethylaminopyridine (DMAP) were added to $1-2$ mL of DMF.
3. ~ 35 µL of 3-mercaptopropionic acid was added to the reaction mixture in step 2.
4. The reaction mixture in step 2 was added to the GNR solution and placed in the sonicator at moderate power ($40-60\%$) for up to one hour.
5. The solution was removed from the sonicator and left to mix on a shaker or at room temperature overnight.

2.11.3 Oxalyl Chloride Catalysed Reactions

This reaction was performed under argon atmosphere.

1. GNRs (oxidised) were dispersed in 4 mL of DCM.

2. GNR solution was purged in argon.
3. GNR solution was placed in a 2-neck round bottom flask with a magnetic stir bar. Attached vertically was a dropper funnel, and to the side an argon filled balloon.
4. ~200 μL of oxalyl chloride was added to the solution and left to stir for 2 hours.
5. Excess CA was added to the mixture
6. 100 μL of DMF was added dropwise and left to stir for an additional 2 hours.
7. The reaction mixture was washed with excess sodium hydrogen carbonate in DMF.
8. The solution was reduced to dryness on a rotary evaporator then resuspended in 4 mL of H_2O.
9. The solution was dialysed into MQ H_2O.

2.12 GONR-CA AuNp Functionalisation

1. GONR-CA synthesis as above in 2.10.1.
2. GONR-CA solution was diluted in MQ H_2O to a barely visible grey colour.
3. 50 μL of GONR-CA was added dropwise while stirring to 100 μL of optical density 1 (OD1) 10 nm AuNps.
4. The solution was left overnight to complete functionalisation.
5. The solution was resuspended via vortexing before characterisation.

2.13 AuNp Synthesis

AuNps were synthesised using the Turkevich method as refined by Frens.[107] Briefly, solutions of chloroauric acid ($HAuCl_4$) (0.01% by weight, solution 1) and

trisodium citrate (1% by weight, solution 2) were prepared, and 50 mL of solution 1 was heated to boiling. Next, $0.8 - 1$ mL of solution 2 was added (quantity determines particle size, less makes larger) to solution 1. Synthesis was complete after 5 minutes of boiling.

2.14 Filamentous Bacteriophage Functionalisation

1. Prepared CTAB stock solution by saturating 25 mL of MQ with CTAB at 50 °C and left to cool to room temperature.
2. 1 mL of the stock solution was added to a vial with GNBs and 1 mL of MQ.
3. Solution was sonicated at 100% power for 1 hour, then left at 20% power overnight.
4. GNR CTAB solution was removed from the sonicator and dialysed into 5 L of MQ overnight (single dialysis).
5. Sample was centrifuged then maximum speed for 15 minutes.
6. Supernatant was discarded and pellet was resuspended in 500 µL of MQ by low power ($10 - 20\%$) sonication for 5 minutes, then left to rest overnight.
7. 100 µL of the supernatant of this sample was added to a 1.5 mL plastic tube, along with 2 µL of 1M HEPES buffer (pH 7.4), 78 µL of MQ, and 20 µL of phage solution (at $\sim 2 \times 10^{10}$ phage μL^{-1}).
8. The mixture was left to functionalise overnight, and was used as the impure sample.
9. The impure sample was washed twice in MQ to give the purified sample.

Chapter 3: Mechanically Fractured GNRs

As discussed in chapter 1, GNRs can be synthesised via a range of unique techniques, however, few are capable of generating high quality material in a scalable and efficient manner. Mechanical fracturing of graphene represents a simple synthetic method for generating a range of nanostructured graphene materials of remarkably high quality. While typically generating low yields, the dry-cut adaptation introduced in this chapter improves upon this significantly. The ability to cleave graphene into pristine, highly ordered fragments is attributed to the material's relatively low fracture strength – and while the mechanisms governing this process are not well understood, this chapter examines them in the context of the literature, and discusses their significance and consequences in the mechanical fracturing setup.

3.1 Mechanical Fracturing

Microtomy is commonly used for making thin sections of a sample (usually biological) for TEM analysis. In 2014, however, Mohanty *et al*. demonstrated the use of simple microtomy techniques to cleave highly-ordered GNRs from a block of highly-oriented pyrolytic graphite (HOPG).[105] In this method, a diamond knife is mounted in a microtome cutting block, while a block of HOPG is fixed to a cube of resin, and mounted in the microtome chuck head. The chuck head is brought down over the diamond knife edge serially with a step distance determining the amount of block fed over the knife. Each cut cleaves stacks of "graphene nano-blocks" (GNBs) consisting of millions of GNRs (see Figure 3. 1). A boat of water is positioned behind the knife, such that the meniscus is in contact with the knife edge (Mohanty *et al.* version only). The GNBs are fed onto the water boat, held afloat by surface tension and pushed away by the movement

and subsequent cleavages from the block. Our method, as depicted in the following figures, does not use water in the knife boat.

The chuck is positioned so that the graphitic planes are aligned perpendicular to the knife edge (see Figure 3. 1 for representation). The angle of the block face with respect to the cutting direction is controlled such that an angle of 0° will cut evenly through the face generating parallel GNRs, while a non-zero angle will (for initial cuts) begin cutting shallow then deepen (or vice versa) as the block face continues down. In this respect, a non-zero angle can afford one degree of control over structure by allowing the generation of tapered GNR products. The microtome automates the cutting process by bringing the chuck down linearly over the diamond knife in the direction marked in Figure 3. 2c. At the end of this movement, the chuck is brought back and up, then forward and up, tracing a "D" shape in the air (backwards "D" with respect to Figure 3. 2c). As the chuck reaches the top of this arc, it steps forward a set distance then begins another linear pass over the block. This process continues until manually stopped, and the cutting speed is controlled typically between $0.4\ \mathrm{mm\ s^{-1}}$ and $0.8\ \mathrm{mm\ s^{-1}}$. By controlling the step distance, GNRs of set widths can be cleaved. The limits of widths achievable using this method are dependent on the microtome's limits, generally ranging from $20\ \mathrm{nm}$ to several micrometres. Thinner structures can be generated via control of cutting angles – for instance, by rotating the knife around the pivot angle, the block can be cleaved from one corner inwards, generating a small number of sub-$10\ \mathrm{nm}$ GNRs where the outermost sections of knife edge meet the block faces. In addition, the process of block levelling has been observed to generate tapered GNRs as thin as $10\ \mathrm{nm}$.

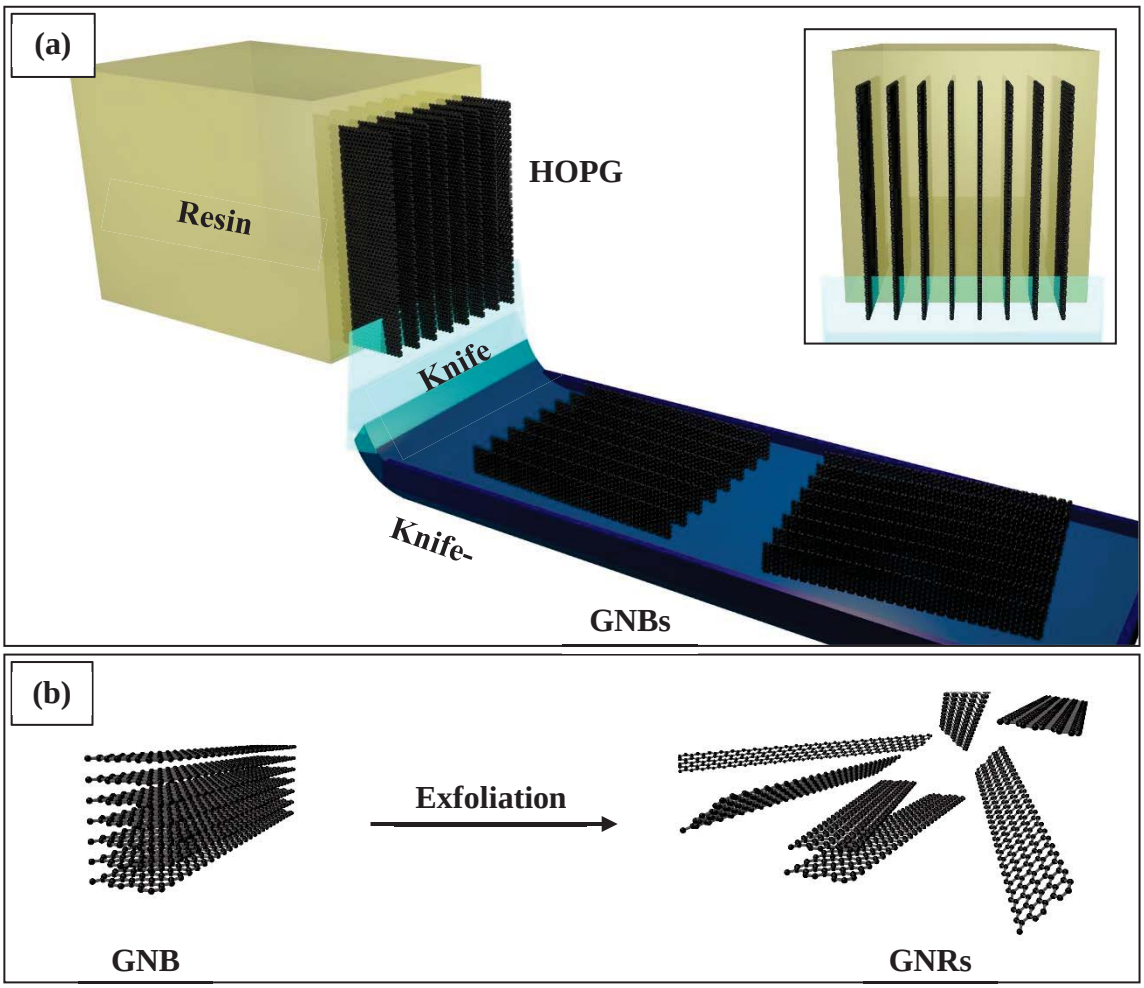

Figure 3. 1 - 3D representation of GNR synthesis via mechanical fracturing in air. (a) Cutting of GNBs from HOPG block mounted in resin and microtome. Inset: front view representation of block face showing direction of graphitic planes. (b) Exfoliation procedures generate multi and single-layer GNRs. No liquid or solvent is present in the boat during dry cutting and collection.

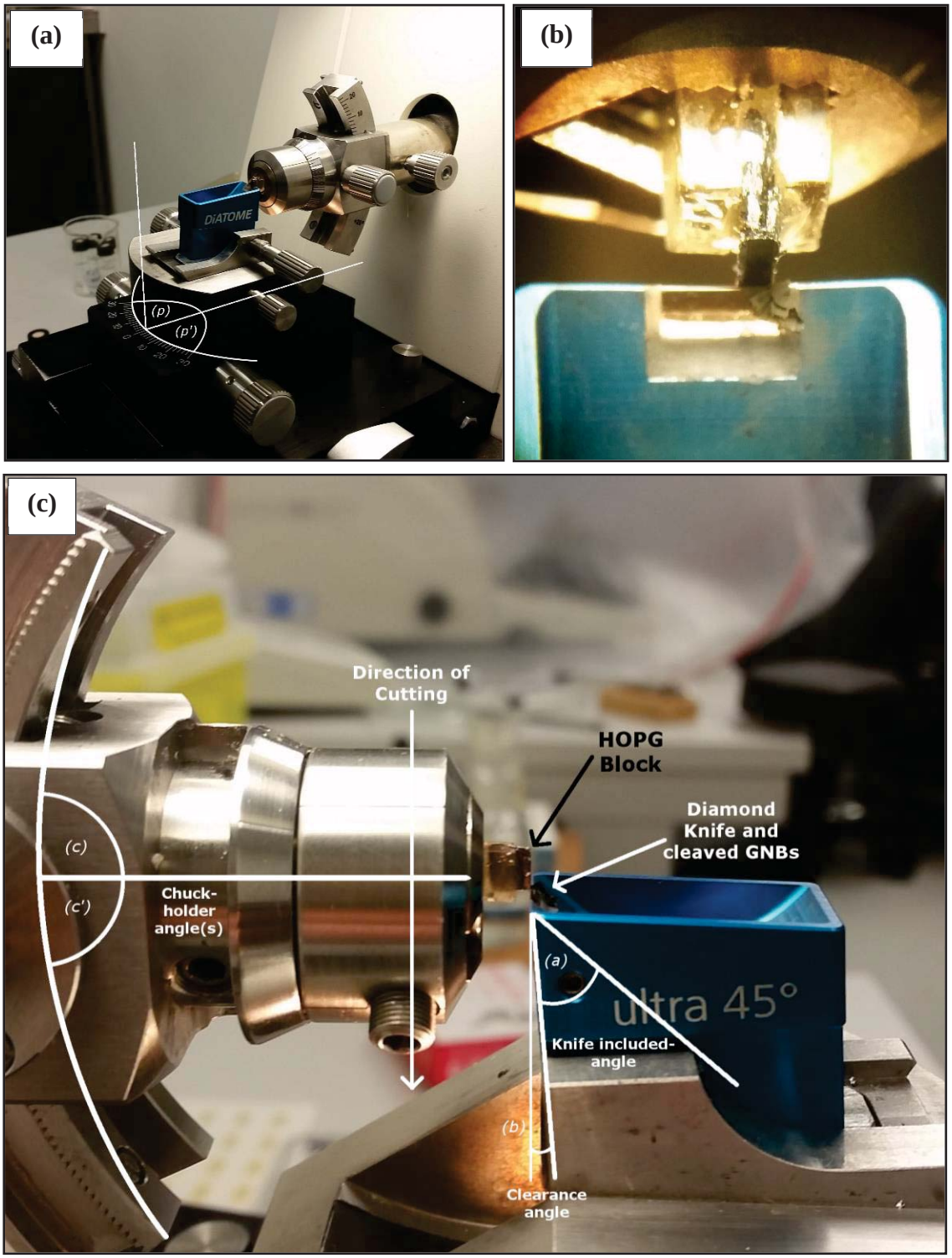

Figure 3. 2 - Microtome setup for mechanical fracturing in air. (a) Microtome apparatus as prepared for fracturing HOPG. Diamond knife and boat mounted in centre of image. Pivot angles displayed as (p/p'). (b) View of the cutting process down the microtome eyepiece. HOPG block is in contact with knife edge (central clear section of boat), and GNBs can be seen collecting on the side of the knife (out of focus). (c) Side view of microtome setup with angles overlain: Knife included-angle (a), clearance angle (b), chuck-holder angle(s) (c/c').

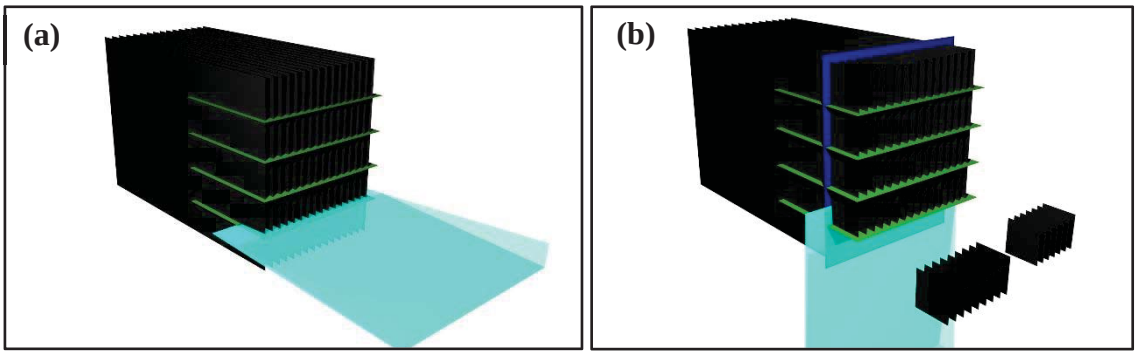

Figure 3. 3 - 3D representation of how GQD "nanosquares" can be synthesised using mechanical fracturing. Green planes show initial partial cuts into the cutting face. Figure adapted from Mohanty *et al.*[105] Blue plane shows secondary cut bisecting initial cuts, and the GNBs generated.

Further degrees of control can be introduced to produce additional geometries. Consider a scenario where a block has multiple parallel partial incisions into the cutting face, each spaced apart by a single set distance (Figure 3. 3a). By now cutting the block face at a set distance equal to the initial cut spacing, graphene nanosquares can be generated (Figure 3. 3b). This approach was used by Mohanty *et al.* to create a range of graphene nanostructures, including graphene quantum dots (GQDs), of square, rectangular, and triangular shapes. The triangular GQDs can be generated by altering the pivot angle.

GNBs can be collected by draining the boat entirely or by carefully drawing off the surface using a small metal loop. Subsequent exfoliation then generates multi and single-layer GNRs.

3.2 Mechanical Fracturing in Water

Using this method, we made important observations which led to the subsequent optimisation of the cutting procedure (full details of setup in methods). Proper alignment of the HOPG block with the diamond knife is critical for obtaining high-quality GNRs, which was alluded to by Mohanty *et al.* Improper alignment provides poor cutting (see Figure 3. 5), and thus realignment is required before each cutting session for the best results, and was typically performed by the microtomy technicians via minor adjustments

to the angles in the setup. The quality of the cut can be qualitatively judged by the way material is cleaved from the block (smooth cut or rough powdering), and how the block face reflects light. Poor-quality cuts will generally be less reflective, and may cause larger broken sections to cleave from the block, which was termed “powdering” due to its physical appearance. Powdering generates large flake and aggregate impurities.

Excessive block wetting is a problem where the water from the knife boat is drawn onto the block face and surrounding sides via capillary action. It is expected that the cutting face will become wet, and in doing so facilitates a clean cut. However, wetting of the other faces is not desirable and generally causes a decrease in cutting quality. Excessive wetting can also produce powdering at either end of the knife edge, as this material is more prone to physical displacement from the block via shearing and peeling rather than fracturing.

Occasionally, GNBs will not cleave away from the knife edge, and will instead begin to clump near it. This can inhibit access to the knife edge and decrease the quality of subsequent cuts. Occasionally, this clumping will cause material to spill back over the knife edge, which then artificially blunts the knife edge and can get caught between the knife and block face, potentially causing damage to both. Constant supervision is required to prevent clumping and is relieved by tugging at the ends of the material to clear it from the knife. Care is required to not touch the diamond knife as this can also damage it.

Regular trimming of the non-cutting block faces is also important to remove flaking sheets which contribute to powdering. This is a relatively mundane process which can be performed during alignment.

3.3 Mechanical Fracturing in Air

While looking for solutions to problems associated with the presence of water in the cutting process, we discovered that the water in the boat is unnecessary for cutting and that fracturing in a dry environment affords a number of significant advantages.

Immediately observable is that the cutting process is visibly cleaner with less powdering. Edge powdering which is observed in wet-cutting is almost unnoticeable in dry cutting (with a trimmed block face). Instead of being drawn away by the surface tension of the boat, GNBs tend to fold and stack on one another, making their way down the inside of the knife face (see Figure 3. 4b). The material closest to the knife edge is then pushed down and replaced by material from the next cut. The result is a pencil-shaving-like wafer of GNB material shown in Figure 3. 4, and can be left to automatically cut before collection for much longer periods than wet-cutting procedures. Occasionally, a section of light GNBs will fold back towards the knife edge, and needs to be cleared manually. This usually only happens during the first few cuts, as the weight of previous cleaved sections helps pull the material away from the knife edge.

The collection of GNBs is much easier, and is achieved by picking up the stacks of GNBs with a fine brush (toothpick and hair) and placing in a vial either dry or with a solvent of choice. Mohanty *et al*. mention 100% efficiency in collection, although we found this to be less in practice due to the way the GNBs break-apart upon physical agitation and stick to the sides of the boat, owing to the hydrophobic nature of the material. This dry-cut method achieves much closer to 100% yields in this regard, as very little material preferentially sticks to the walls over the GNB stacks themselves.

Upon study of the dry-cut GNRs via Raman spectroscopy and TEM, we observe that the quality of the material is significantly higher than that of the wet-cut technique,

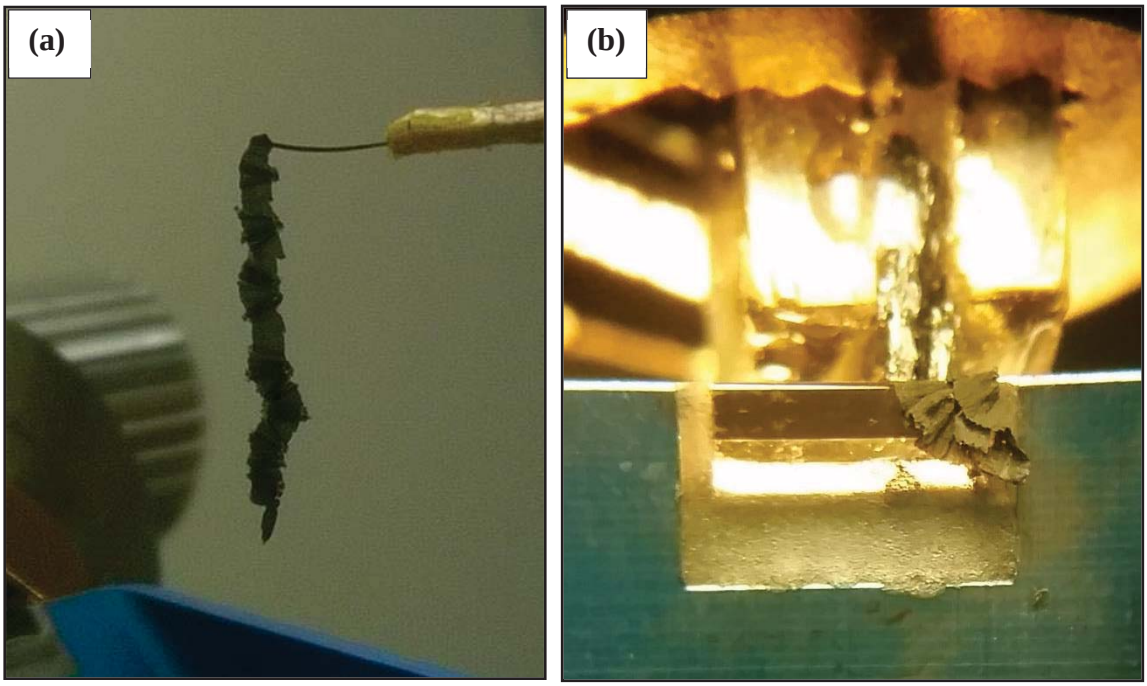

Figure 3. 4 - (a) Strip of dry-cut GNBs collected on brush. (b) View down the eyepiece of the microtome at the knife edge, where GNBs can be seen (in focus) stacked and folded over.

as identified by the I_D:I_G ratios of experimental and reported data. This is discussed in more detail in chapter 4.

3.4 Discussion of Mechanical Fracturing

Mechanical fracturing of GNRs is possible due to the low fracture toughness of graphene.[108] The MD studies done by Mohanty *et al*. predict that when the knife edge presses into the graphene it generates localised tensile stress perpendicular to the cutting direction, and compressive stresses in the direction of cutting at the point of contact. This stress eventually overcomes the bond strengths in the lattice and a crack occurs. Crack propagation was shown by Mohanty *et al.* to occur in the direction of cutting, generating straight edges regardless of crystallographic orientation. On an atomic level, edge structures are defined by the pattern of bond breaking in both armchair and zigzag directions. Rearrangements, such as those that generate Stone-Wales defects (which involve the 90° rotation of a carbon-carbon π bond within a graphene lattice, resulting in two 5-membered and two 7-membered rings surrounding the bond), are also predicted to occur from the dangling bonds and energetically unfavourable conformations caused by the violent fracturing events, resulting in non-crystalline edge structures.

Additional MD studies by Mohanty *et al.* on tensile shearing of graphene sheets under different crystallographic orientations identified a tendency to cleave along zigzag edges perpendicular to uniform stress loading. This was also identified in MD simulations which model the fracture toughness of graphene.[36] When zigzag edges are perpendicular to the stress loading, straight cracks propagate directly through the lattice generating clean zigzag edges. Armchair oriented sheets show crack formation and propagation in alternating patterns through the lattice, generating a mixture of zigzag and armchair edges. These simulations provide a more accurate representation of the kinds of fracturing that occur within the 3D HOPG, because they simulate an overall tensile stress applied

across the graphene. This may be because, in a 3D block, the section of GNBs which has passed the knife is being deflected away from the rest of the block (to which it is still attached) at the knife's receding angle (45°). This will generate tensile stress perpendicular to the block face and laterally through the basal plane, which favours crack propagation via fracturing. Therefore, the driving force for mechanical fracturing of GNRs is likely a combination of the in-line compressive and in-plane perpendicular tensile forces.

Another factor to consider is the possibility of intergranular fractures, as described by Zhang *et al.*,[36] which bypass the direction of cutting at domain boundaries by fracturing around the next crystal domain within a polycrystalline layer, rather than through it (see Figure 1. 2b). Such a scenario needs to be considered in 3D, where stacking interactions may help brace fragments against intergranular fracturing. Therefore, this would be most likely to happen when an intergranular fracture allows the freeing of a large, weakly bound fragment of the HOPG. Such a fracture could be thought of as microscopic shearing rather than cutting or fracturing, and is likely the kind of scenario that causes powdering at the edges of the block (where the block may be frayed or damaged and is less rigid), and when improperly aligned. Debris build-up on the knife edge or block face may also favour intergranular fracturing, due to a larger distribution of knife pressure by an artificial blunting effect. Such a blunting effect has been observed to cause powdering during cutting, and has been remedied by cleaning the knife. Another investigation of fracture forces at grain boundaries[109] found that boundaries between two distinct crystallographic orientations within the same crystal increase the forces required to continue the fracture, but only along the boundary itself, with the fracture forces returning to normal after passing it. A similar effect was noted by Zhang *et al.*, where Stone-Wales defects act to partially stabilise graphene against fracturing, but not prevent

it. Other MD studies have also identified a strong correlation between fracture strength and the types of geometries that distribute the stresses.[110] These results suggest that during the cutting process, boundaries between grains and crystal domains may resist fracture propagation, and could facilitate the generation of defects or strain-induced shearing. This means using a higher grade HOPG (i.e. ZYA) with lower mosaic spread and fewer grain boundaries will generate higher quality material (on average). The significance of these fracture resisting effects will likely depend on the efficiency of cutting. When improperly aligned, poor cutting results and generates a large amount of powdering, as the forces impacting on the block favour a grinding or crushing effect, rather than fracturing. In such cases, IR spectroscopy has been able to identify characteristic signatures of CVD-like* graphene edges, which are distinct from graphene edges generated via the directed cleavage of clean fracturing. Unlike cleanly fractured GNRs, which show signs of edge-rearrangement and the incorporation of nearby gas molecules, these CVD-like pieces cannot have been formed by bond-breaking fractures. Hence, they are believed to be evidence of intergranular fractures, which are capable of cleaving crystallographic domains intact from the HOPG block face.

Similar to powdering, an inefficient cut may also cause uneven fracturing of GNRs through the block face. This has been observed in TEM multiple times (see Figure 3. 5) but is not as noticeable during cutting as powdering is. The result is a strip of graphene with a high-aspect ratio but microscopically uneven and irregular edges. These types of fractures may be caused by improper alignment, or a blunt or blocked knife edge, which are unable to adequately focus the force of cutting, favouring poorly-directed fracturing through the block due to higher overall compressive stresses.

* This refers to the kinds of edges generated by controlled CVD growth of graphene, which are pristine, crystalline (all aromatic 6-membered rings), and hydrogen terminated, with a mixture of armchair and zigzag edge structures.

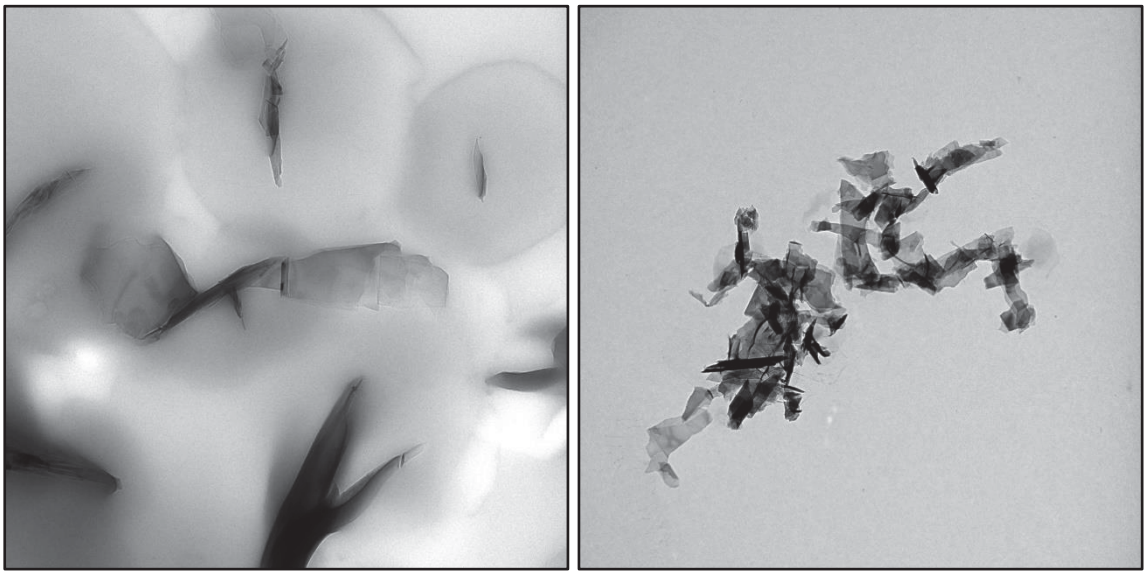

Figure 3. 5 - TEM images of GNRs generated via incorrect alignment. Note the uneven edges, yet overall ribbon-like appearances. These images indicate irregular fracturing through the block.

3.5 Summary

Mechanical fracturing of HOPG demonstrates a relatively new approach to top-down synthesis of GNRs, and boasts high-quality material, tunable dimensions, and scalability. Adaptation of this technique for cutting in air improves the quality of the material, the scalability, and further simplifies the method. This technique exploits the low fracture strength of graphene by applying localised stresses to induce directed fracture through a block of graphite, thereby generating stacks of graphene with high geometric purity. This technique is, however, highly-sensitive to the setup conditions, requiring careful alignment, regular cleaning and maintenance of materials, and precision instrumentation. Careful consideration of these conditions and the materials used is required to minimise intergranular fractures which generate non-uniform impurities of "sheared" material. Regardless, this dry-cut adaptation improves the cutting efficiency and provides higher-quality material than the wet-cut version.

Chapter 4: Characterisation

Mechanical fracturing in air provides a more convenient and efficient method towards the synthesis of GNRs over wet fracturing. Therefore, characterisation is necessary to identify the quality, structure, and physical properties of the materials generated to validate this new method of synthesis, and is the focus of this chapter. An effective fracturing technique is expected to generate uniform, clearly defined GNR strips with smooth edge structures and few defects. Therefore, the main techniques utilised for characterisation herein are Transmission Electron Microscopy (TEM), Atomic Force Microscopy (AFM), Raman Spectroscopy, and Surface Enhanced Infrared Spectroscopy (SIERS). Together, these techniques provide a detailed description of the materials generated, and form the basis for functionalisation experiments discussed in the next chapter.

4.1 Physical Characteristics – AFM and TEM

AFM and TEM are used to identify the structures and geometries of the materials generated by this dry-cut method. AFM is a scanning probe technique which drags a sharp tip across the surface of a sample whilst measuring its displacement.[111] The tip is attached to a cantilever, off which a laser is deflected onto a photodiode to record deflections. This enables remarkably high *z*-resolution (out of scanning plane), and is capable of resolving physical dimensions on the order of a single atom – ideal for graphene characterisation. The *x*,*y*-resolutions (lateral, in scanning plane) are limited by the tip radius, as a blunt tip is unable to reach between features in a sample and results in convolution artefacts. For this reason, tip radii are typically on the order of nanometers, with some ultra-high resolution tips boasting < 1 nm lateral resolutions.

TEM is a microscopy technique that measures the transmission of a beam of electrons through a sample prepared on a thin film, identifying areas of increased electron-density where the beam is obscured or scattered.[112] The transmitted electrons are then focused and magnified onto a detector to generate an image, which is essentially a 'shadow' of the observed sample. The use of electrons as the beam source affords high resolution but often suffers from poor contrast of thin samples (such as single-layer graphene). This can be improved by lowering the electron accelerating voltage at the cost of resolution. By exploiting the particle-wave duality of electrons, diffraction experiments can be performed to identify crystalline features within a sample, such as the hexagonal lattice of graphene. High-resolution TEM uses higher accelerating voltages, electron wave interference patterns, and aberration correction techniques to achieve atomic-scale resolutions.[113]

It is difficult to obtain an appreciation of the physical flexibility of these materials from literature alone, as published images usually depict flattened GNRs to demonstrate their aspect ratios and geometries.[105] Experiments with larger graphene flakes show they generally lie relatively flat when deposited on clean surfaces, as doing so facilitates solvent exclusion during deposition and maximises the adhesion forces between the two surfaces. As expected, this effect is not as significant with GNRs due to their reduced surface areas.

Figure 4. 1 shows AFM analysis of a section of GNB which is only very gently exfoliated. Low-power (~32 W output) bath sonication in isopropyl alcohol (IPA) was used to achieve this degree of exfoliation, and the terraced facets of unexfoliated multi-layer flake impurities can be seen flanking the GNRs. Immediately visible is the flexibility of the GNB, as the material is able to fold and twist across the substrate.

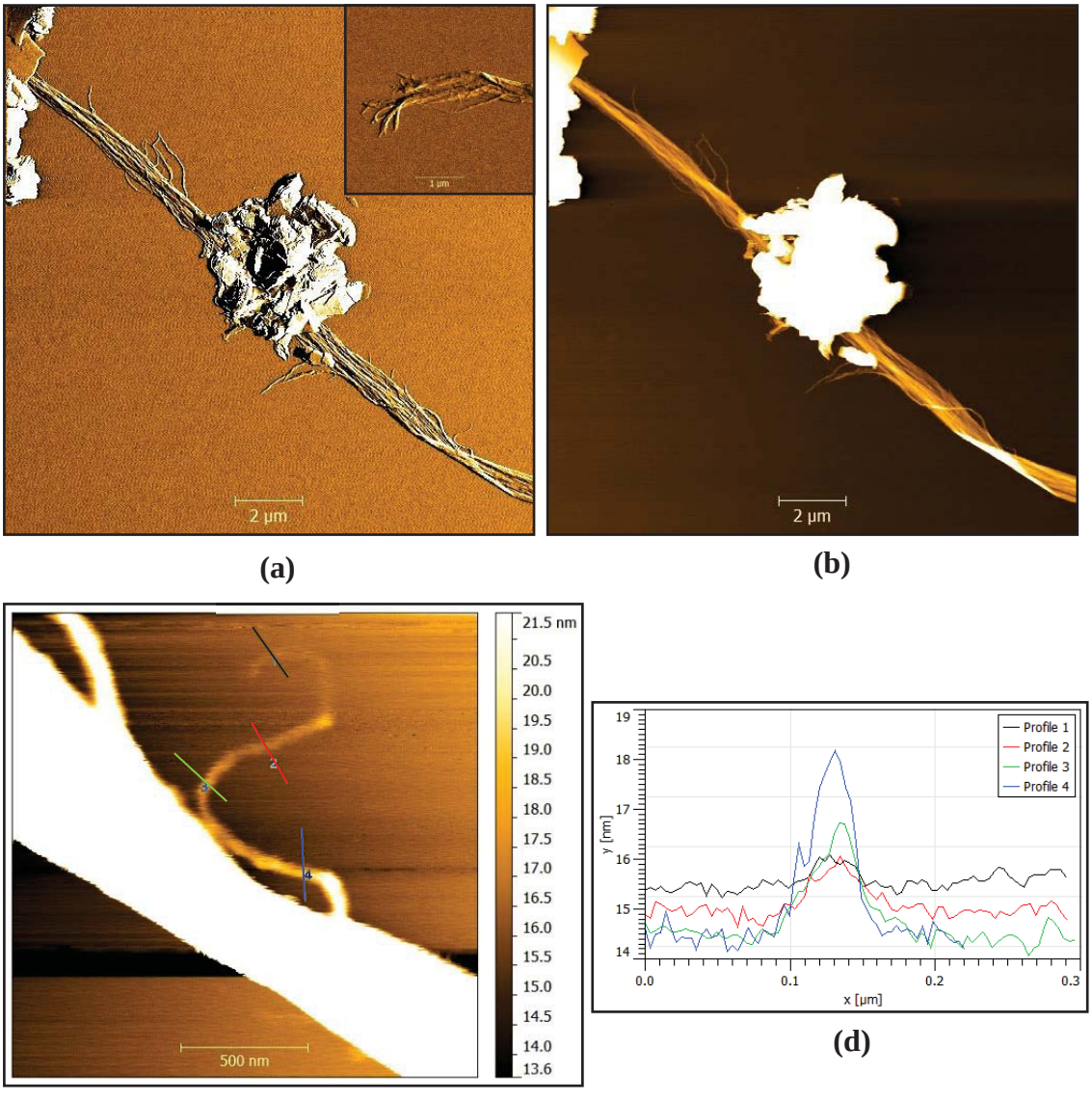

Figure 4. 1 - Tapping mode AFM images of a partially exfoliated GNB on mica. (a) Amplitude channel scan of GNB and aggregate. Inset is amplitude scan of end of GNB stack (see Appendix 1, Figure A1. 1b for relationship with this area). (b) Topography channel scan of (a). (c) Zoom on lower right section of (a/b), contrast-adjusted to highlight fraying GNRs. Coloured bisections correspond to profiles in (d). (d) Cross-section profiles of the fraying GNRs in (c), 1 – 4 from top of image (faintest section) to bottom (brightest).

Z-displacements between 10 nm and 40 nm (see Appendix, Figure A1. 1 for cross-sections) indicate that there are a range of thin and overlaying sections – many of which will not be flat with respect to the substrate. The non-uniform morphology of this GNB across the surface may be explained, in part, by unfavourable interactions with mica. Mica has a net negative surface charge when exposed to solutions due to ion-exchange reactions,[114] while graphene also exhibits a slight negative charge in the basal plane due to the localisation of electrons in the π orbitals.[115] Therefore, on the basis of charge interactions and conformational freedom, GNRs can be difficult to deposit smoothly on mica surfaces for characterisation. Zooming in on a fraying section, (c), shows thicker multi-layer segments thinning down to single layer material at the edge of the AFM's resolution limits. This fraying section shows GNRs curving and folding across the surface, rather than lying straight and flat. Discrete folds can be identified by a sharp change in direction and a raised height across the folded section. This can be seen occurring between profile lines 1 and 2 of this image.

This flexibility is also seen in TEM analysis of exfoliated samples (see Figure 4. 2). These images show GNRs which are many layers thick and are still capable of folding, twisting, and coiling into pseudo-nanotubes on the TEM grids. The contrast of the GNR material gives an estimate of the thickness, however other techniques have been employed for quantification. Tilting the TEM grid holder allows imaging of samples at angles steep enough to identify the edges of upper and lower layers of the GNR stack (Figure 4. 3). Subsequent AFM of these TEM grids using low-set-point contact mode allows the quantification of the height of multi-layered stacks without piercing the thin formvar layer of the TEM grid (Figure 4. 4). These GNR stacks show *z*-displacements ranging from $10 - 20$ nm, indicating these GNR stacks are tens of layers thick ($\sim 29 - 58$ for this range).

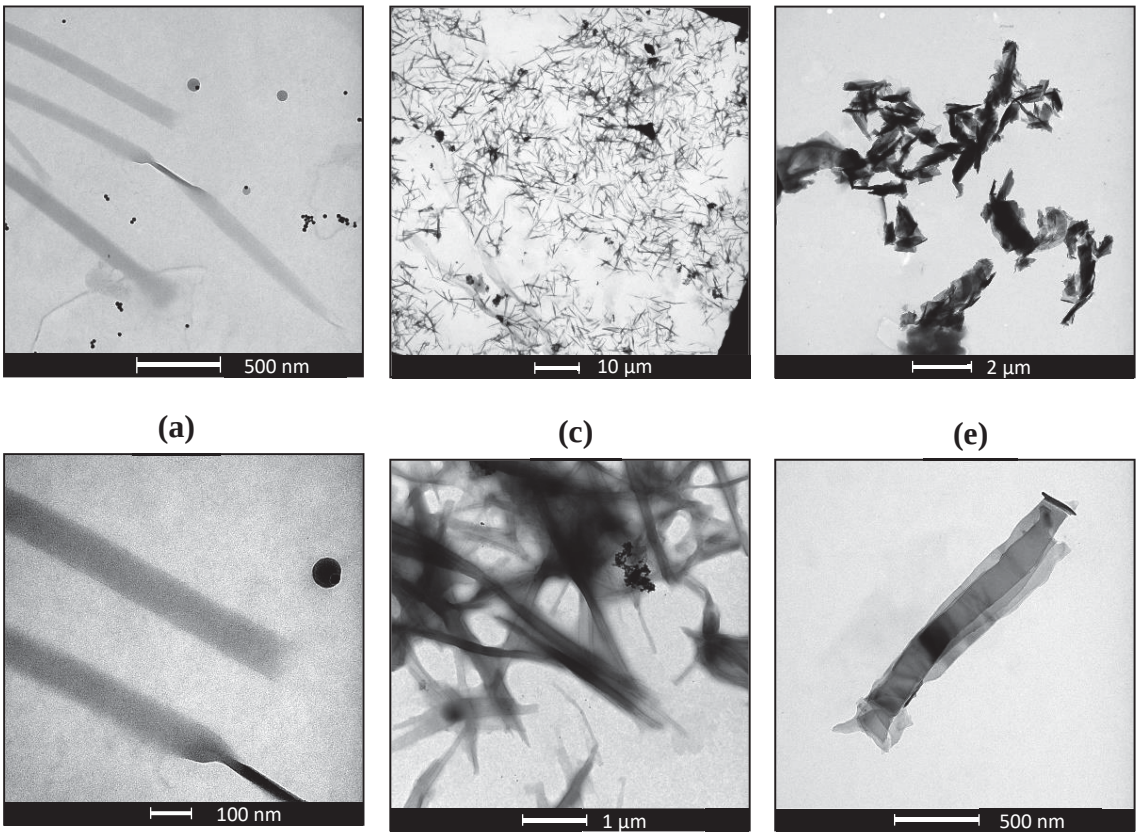

Figure 4. 2 - TEM images of GNRs with respect to exfoliation extent. (a/b) Minimal exfoliation. (c/d) Moderate exfoliation. (e/f) Extensive exfoliation.

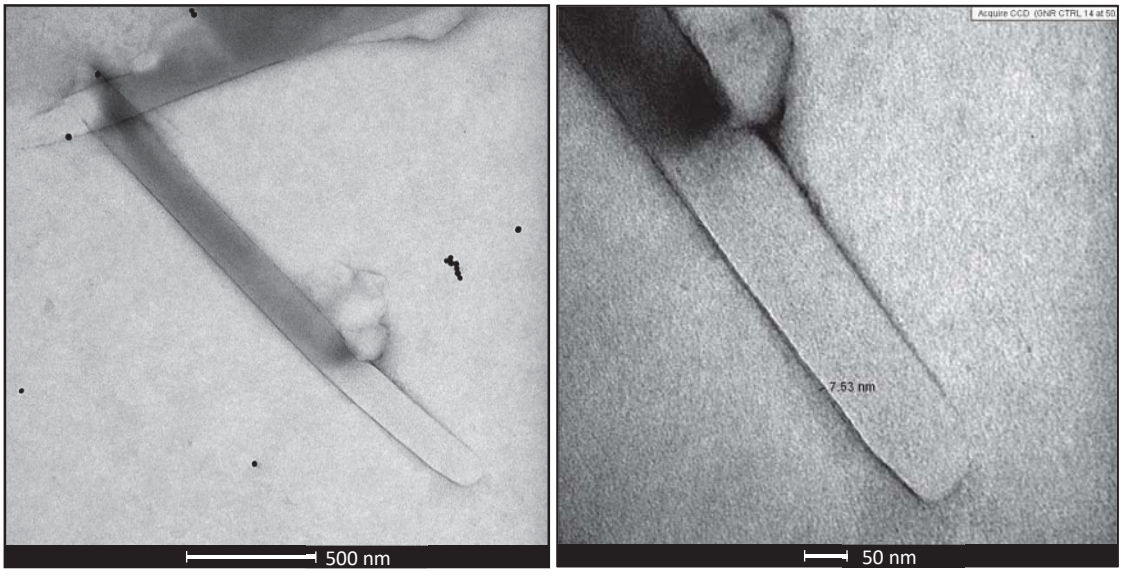

Figure 4. 3 - TEM images of GNR stack as viewed (a) perpendicularly (usual imaging angle), and (b) at 50° to perpendicular. Distance of drawn line between top and bottom layers shown as 7.53 nm. Actual stack height will be larger. See Figure 4. 4 for stack-height quantification. Note the decreased contrast near the ends of the stack due to beam-excitation and evaporation of solvent trapped between layers.

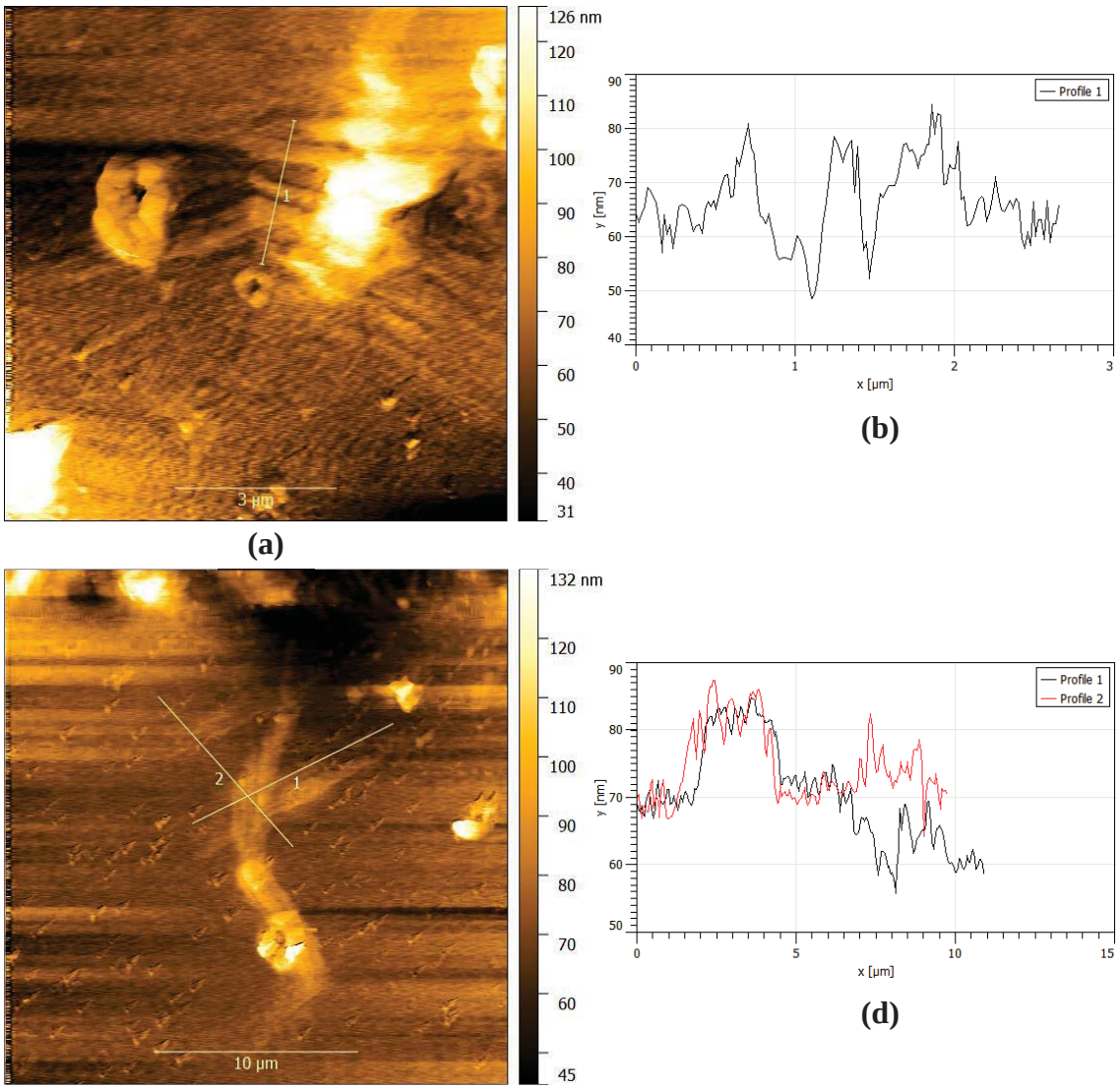

Figure 4. 4 - GNR stack height determination using contact mode AFM of the TEM grid in Figure 4. 3. (a) Topography scan of a row of GNR stacks. (b) Cross-section profile of the row of GNR stacks in (a). Stack heights estimated around $10 - 20$ nm ($30 - 60$ layers). (c) Topography scan of another grouping of GNR stacks. (d) Cross-section profiles of (c), with GNR stack heights estimated around $10 - 20$ nm also.

Control over the extent of exfoliation leads to different microstructures of GNRs, with accompanied changes to flexibility seen in TEM images (Figure 4. 2). Minimal exfoliation (left column) shows rigid multi-layer GNR stacks with straight edges. Moderate exfoliation (middle column) provides GNR stacks which are more flexible, but still rigid enough to retain a relatively flat shape. Extensive exfoliation (right column) reveals thinner GNR stacks which can coil and fold into stable conformations. These coils are also observed in thicker stacks (see (a) and (d)), indicating that despite induced strain these twisted conformations are favourable. Considering their thermodynamic stability, a flat stack is a low entropy conformation, while twists and coils are much higher due to the many ways they can be generated. In addition, coiling and folding allow intramolecular (in this case a molecule is a single GNR sheet or stack) contacts to be made between the hydrophobic sheets, lowering surface area, excluding solvent, and providing van der Waals attraction forces between them. Therefore, these factors provide both positive ΔS (entropic) and negative ΔH (enthalpic) contributions, which favour a negative ΔG (Gibbs energy) for folding. Aggregation of GNRs and stacks into large bundles can be described as the intermolecular consequence of the above effects. The intense coiling observed in the extensively exfoliated samples may also be explained in part by solvent interactions, as literature has reported that graphene sheets have been observed via optical and Raman microscopy to wrinkle and roll in the presence of ethanol (EtOH).[116] The Raman spectra of these samples also showed the development of a D band and broadening of the G and 2D bands, indicating an increase in disorder attributed to inducing topological strain within the graphene.

Figure 4. 5 illustrates GNR flexibility further by showing how GNR stacks under 100 nm wide can curve laterally across the TEM grid whilst lying mostly flat. These images show tapered GNRs which become visibly more flexible as their widths decrease

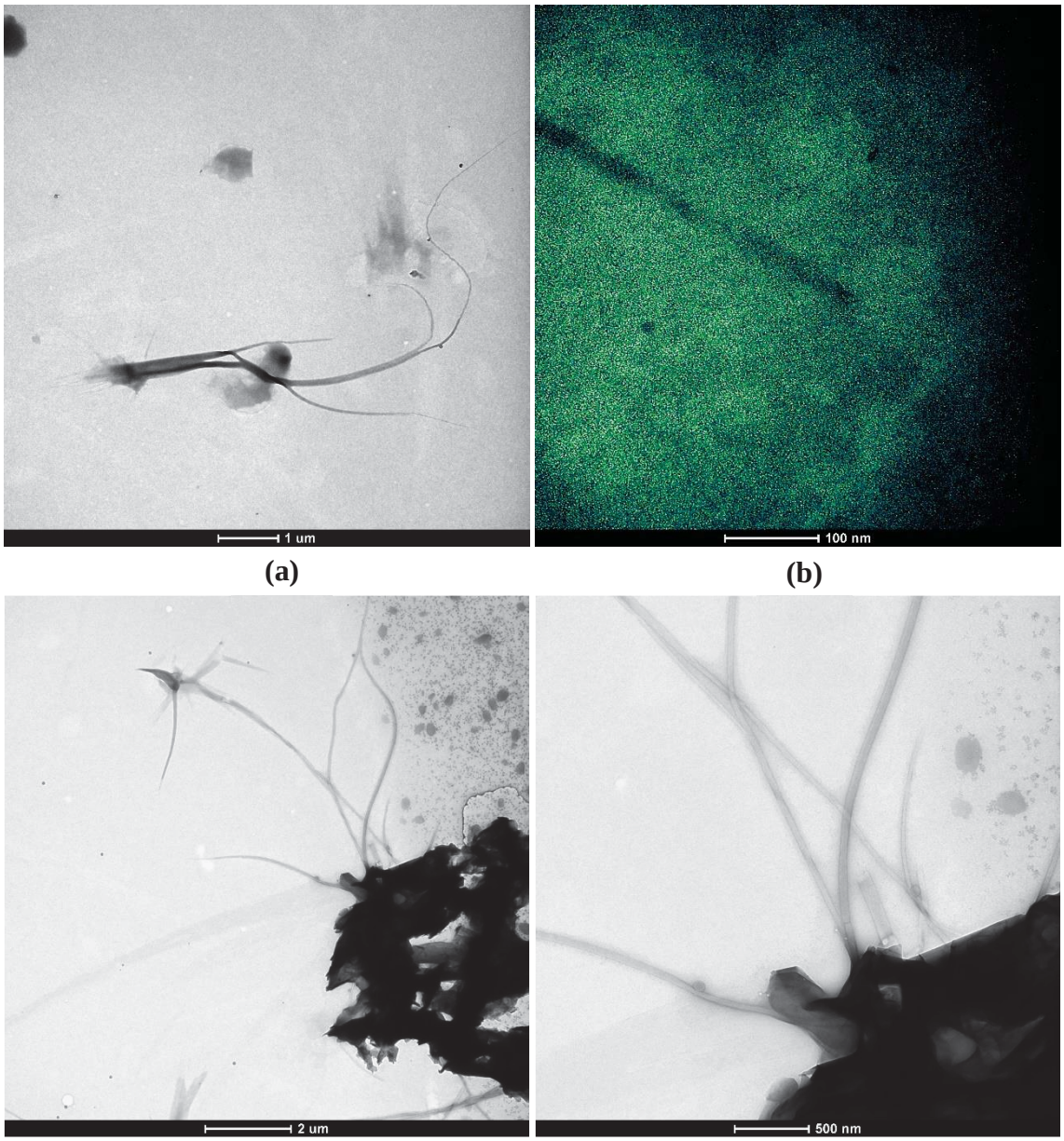

Figure 4. 5 - TEM images of tapered GNR stacks. These stacks are generated during block face levelling in the initial cuts after alignment. (a) GNR stacks with a particularly long section of tapering GNR demonstrating increasing flexibility with decreasing stack width. (b) False colour image (to improve contrast) of near 10 nm wide end of a tapered GNR stack. (c) Multiple GNR stacks demonstrating high-flexibility next to a large aggregate. (d) Zoom of (c) showing stacks of varying widths.

((a) illustrates this nicely). This is likely a result of lower in-plane strain due to a decreased width, allowing greater conformational freedom. Further, the lateral curving across the grid may be facilitated by coiling and folding (see Appendix, Figure A1. 2 for magnification).

Paying close attention to Figure 4. 2a/b, the stacks of GNRs follow a straight direction microscopically and seem to have very smooth edges, at least at the low resolution of these images. It has been demonstrated in the literature that while graphene edges may seem microscopically smooth with well-defined edges, their atomic structures can still be quite disordered.[117] Mohanty *et al.* describes a global edge direction, regardless of crystallographic orientation as a consequence of the cutting process and the edge-rearrangements therein. Preliminary high-resolution TEM images shown in Figure 4. 6 demonstrate that these dry-cut multi-layer GNRs have relatively low edge roughness's of less than 1 nm. However, due to poor instrument focusing in these images, further high-resolution studies are necessary to quantify this accurately. Edge-polarisation studies using Raman spectroscopy performed by Haidee Dykstra indicate the edges are a mixture of armchair and zigzag, with a slight predominance for zigzag. This agrees with

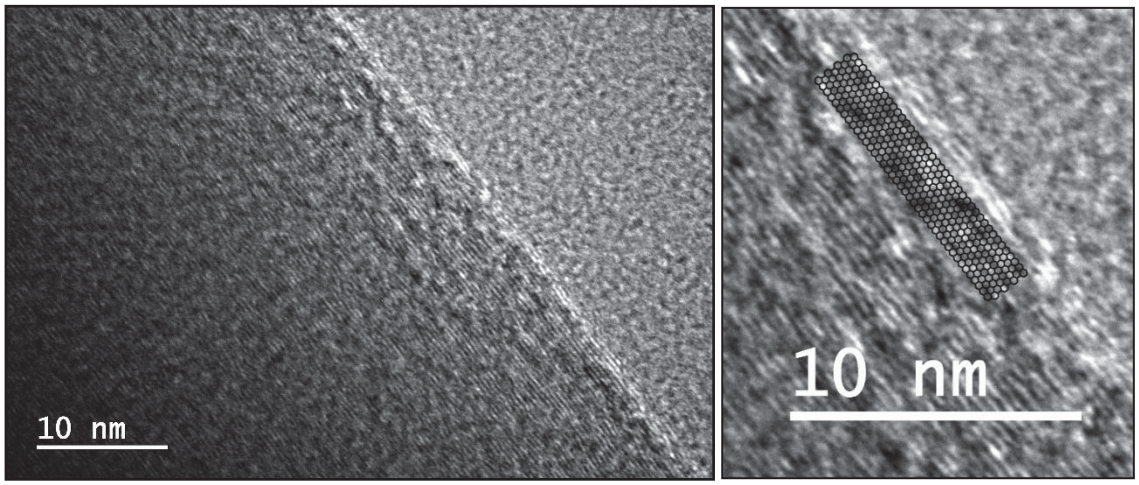

(a) **(b)**

Figure 4. 6 - (a) High-resolution TEM image of GNR (stack) edge. (b) zoom of (a), with honeycomb schematic overlain for atomic-scale perspective. Images are slightly unfocused, but edge-smoothness is observable and predicted to be < 1 nm.

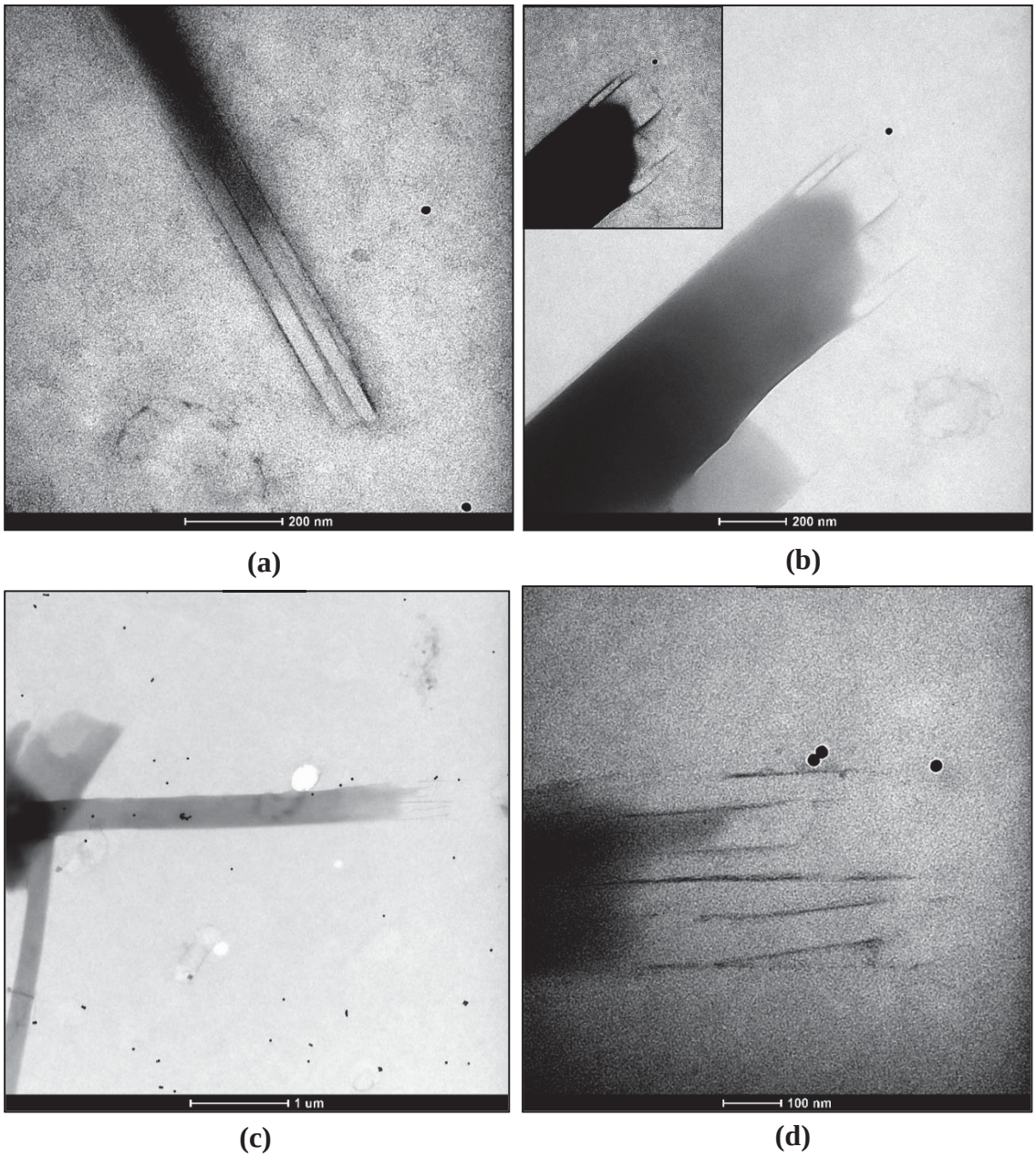

Figure 4. 7 - TEM images of GNR stacks exhibiting diminished scattering at ends and perceived broadening of stack widths. (a) Fraying GNR stack end. (b) Fraying GNR stack end. Inset shows high-contrast image of (b) at the end of the stack. (c) Stack of significantly broadened GNRs with fraying end. (d) Zoom on the end of (c) showing fraying ends. Black dots in each image are AuNps.

the conclusions drawn by Mohanty *et al.*, whose MD simulations show rearrangement after bond-breaking and zigzag favoured edges.

TEM analysis of partially exfoliated stacks also shows fraying intermediates where the layers within a stack spread laterally but remain as part of the stack, overlapping each other. This effect can be seen in Figure 4. 7 and is important to note when assessing GNR dimensions and sample homogeneity. Visible in these images is a decrease in contrast near the ends of these stacks. We believe the darker areas contain solvent trapped between the GNR layers, which increases electron scattering through these stacks. At the fraying ends, this solvent is less-insulated by the surrounding GNRs and is thus more susceptible to evaporation under vacuum and beam-excitation. Bubbles of evaporated solvent have been observed forming under beam-excitation of GNR aggregates and stacks (see Appendix, Figure A1. 7 for images). These lighter areas allow the fraying and overlapping GNRs to be individually identified via their outlines, and show how a stack of GNRs can appear wider than its constituents. Solvent expulsion in via beam-excitation has also been observed at the ends of un-frayed GNR stacks, which is visible in Figure 4. 3.

4.2 Raman Spectroscopy

Raman spectroscopy can be used to probe the crystallographic vibrations in graphene, providing many insights into the material's structure.[117] For graphitic materials, there are two main peaks which describe quality as a function of defects, edges and the basal plane carbons. The "G" band is a lattice mode which rises from carbon-carbon stretching modes within the basal plane. The "D" band is a peak arising from defects and the atomic edge structures. More specifically, the D band arises from inelastic scattering of charge carriers by phonons, and further elastic scattering by a defect or zone boundary, resulting in recombination which provides the D band.[118] Of the two types of edge

structures, zigzag does not give rise to a D band because it cannot elastically scatter charge carriers. In practice, anything but a perfect zigzag edge will have some D band signal owing to edge roughness and intrinsic defects, allowing for elastic scattering to occur. When the intensities of the D and G bands are taken as a ratio (I_D:I_G), this can be used to quantify the overall quality of the material.

With graphene nanomaterials, there is often a larger D band, owing to the increased ratios of edges to basal-plane atoms. Therefore, with low defect starting material (such as ZYA grade HOPG), the D bands of as-cut GNB samples collected from the same block are provided almost exclusively by the edge atoms. Therefore, by averaging the I_D:I_G ratios across a sample, the quality of the material can be quantified. Our group, and specifically Haidee Dykstra, has analysed the Raman spectra of wet-cut materials in detail.[119] Figure 4. 8b is an excerpt from her work, showing experimentally obtained I_D:I_G ratios for both wet-cut and dry-cut material at varying widths. The wet-cut ratios match well with those reported by Mohanty *et al.*, and the dry-cut I_D:I_G ratios are significantly lower (by ~25%) for GNR widths between $20 - 500$ nm, which suggests

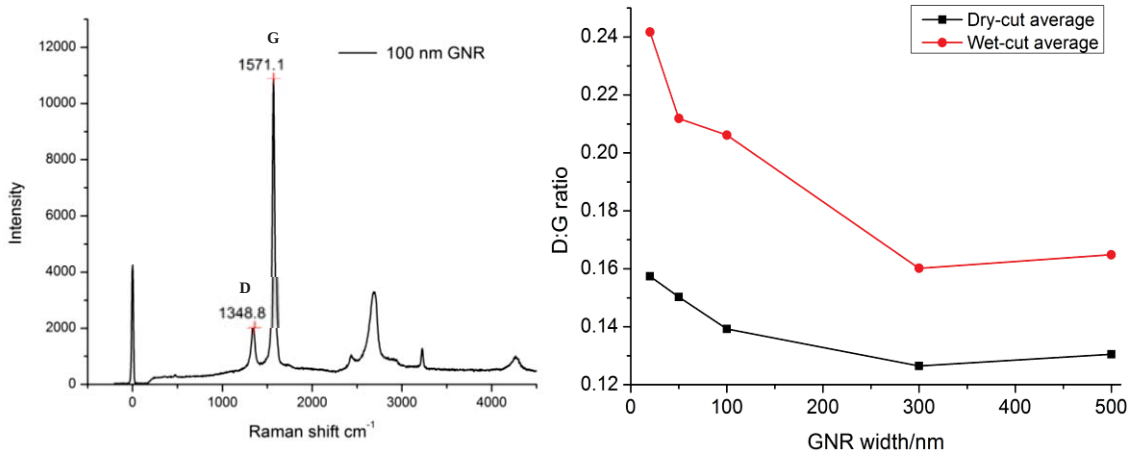

Figure 4. 8 - (a) Raman spectrum of 100 nm wide GNR. D and G bands marked at 1348.8 cm^{-1} and 1571.1 cm^{-1} respectively, with an I_D:I_G ratio of 0.143. (b) Averaged I_D:I_G ratios as a function of width for wet and dry-cut GNRs. Data points from left to right are 20 nm, 50 nm, 100 nm, 300 nm, and 500 nm. Wet-cut I_D:I_G ratios agree well with values reported by Mohanty *et al.* (0.28, 0.24, and 0.22 for 15 nm, 25 nm, and 50 nm wide GNRs respectively). Data and image provided with permission by Haidee Dykstra.[119]

smoother and more ordered edge structures. The I_D:I_G ratios of dry mechanically fractured GNRs presented here are the lowest values, and hence indicate highest material quality, of any top-down synthetic method discussed herein (see chapter 1.7), and to my knowledge reported in literature to date. Bottom-up synthetic approaches usually do not provide I_D:I_G ratios owing to the very narrow (< 10 nm) products involved, and instead demonstrate quality with more direct techniques such as X-ray photoelectron spectroscopy and high-resolution microscopies.

4.3 Infrared Spectroscopy

Infrared spectroscopy (IR) uses infrared excitation to induce changes in a molecule's vibrational state. The frequencies of these vibrations are specific to the atoms and types of bonds involved, allowing the assignment of specific functional groups and vibrational modes to features in an infrared spectrum. These modes reveal important details about the kinds of functional groups and chemical structures within a molecule or material, and therefore makes IR a useful tool for identifying chemical features and modifications in GNRs. Our group has developed a form of solid state enhanced FT-IR Microscopy (SEIRS) which is highly sensitive to changes in the edge structures of our GNRs. For example, Figure 4. 9 shows spectra for two different samples of GNRs, both cut dry at 100 nm wide. These two samples were prepared using the same setup parameters from the same block, but on different days, and at different positions within the block of HOPG. There are several differences between the spectra, but the key differences are, from dry-cut 1 to dry-cut 2: the appearance of combination modes between $1600\ \mathrm{cm^{-1}}$ and $2000\ \mathrm{cm^{-1}}$, and loss of X-H stretches above $3000\ \mathrm{cm^{-1}}$ (where X is an oxygen or nitrogen). We believe that these combination modes arise from edge structures resembling CVD-grown graphene, which is terminated with hydrogen and methyl residues. These modes are referred to as "benzene fingers", due to their "four-

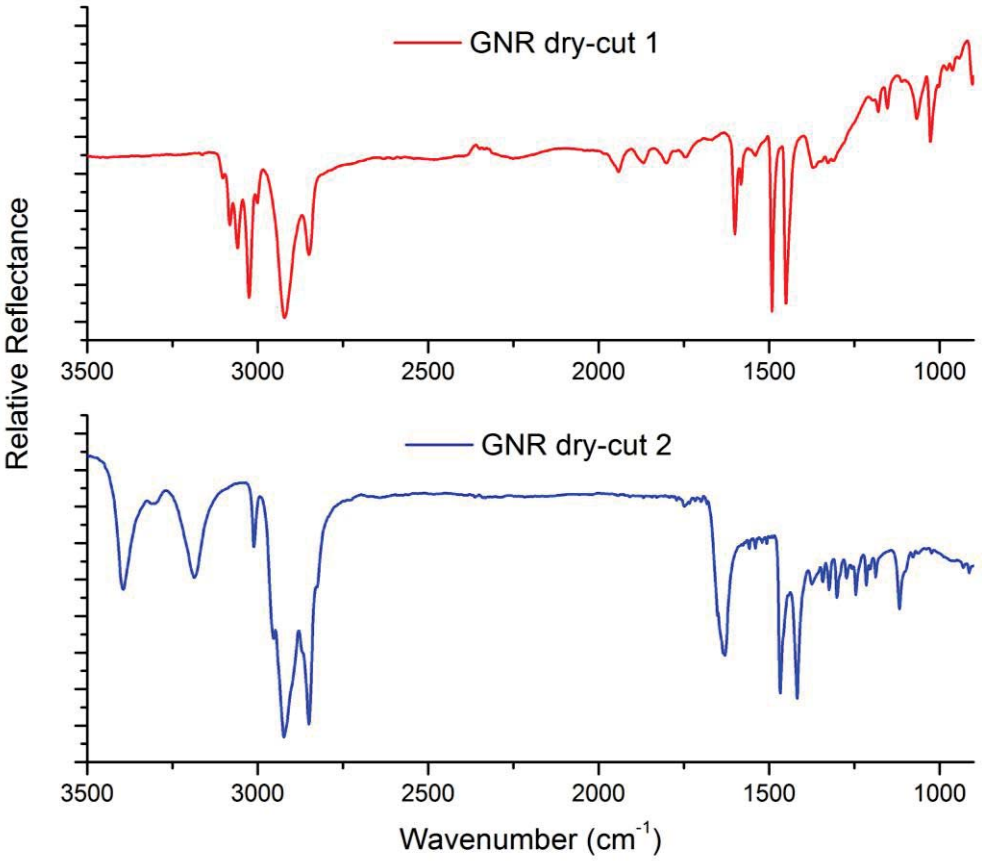

Figure 4. 9 - SEIRS spectra of dry-cut GNRs, prepared using identical procedures on different days. Peak differences between the two samples demonstrate differing edge structures and functional groups in each sample.

digit" structure, and they are ubiquitous throughout substituted aromatic compounds.[120-121]

Figure 4. 10 shows the dry-cut 1 spectrum from Figure 4. 9 overlain onto a number of Spectral Database for Organic Compounds (SDBS) spectra.[122] The combination modes match those of toluene and a cleaved HOPG standard. Such a spectrum could arise in samples via cutting events which shear the HOPG (rather than cleave through it) such as powdering and intergranular fractures (as discussed in chapter 3), or from atomic rearrangements following cleavage. Consequently, these spectra demonstrate how inadequate cutting can result in the generation of impure by-products.

The sharp X-H stretches in the dry-cut 2 spectrum are believed to be caused by oxygen and nitrogen groups, which are consequences of atmospheric nitrogen and oxygen terminating highly-reactive fractured carbon-carbon bonds. Due to the relative abundances in the atmosphere, nitrogen containing residues are expected to dominate. Indeed, when compared with database spectra in Figures 4. 11 and 4. 12, the GNR spectrum matches well with various amino-hydroxy benzene derivatives, indicating the presence of amines, methyl, and hydroxyl groups, which supports the edge-rearrangement hypothesis. There are three peaks in the X-H stretching region, two strong at $3185\ \mathrm{cm^{-1}}$ and $3396\ \mathrm{cm^{-1}}$, and one weak shoulder at $3311\ \mathrm{cm^{-1}}$. Standard IR vibration frequencies suggest that two of these are symmetric and asymmetric N-H stretches, while the last one may be an O-H stretch. Using the database comparisons, it would seem there are a mixture of primary amines, secondary amines, alkyl groups and perhaps hydroxyl groups. However, the lack of similarity between the GNR spectrum and database benzoic acid derivatives is noteworthy (see Appendix 1, Figure A1. 3). It was considered that edge rearrangement processes might bond with both oxygen atoms of O_2 molecules, resulting in the formation of carboxylic acid residues. However, based on these results and the lack

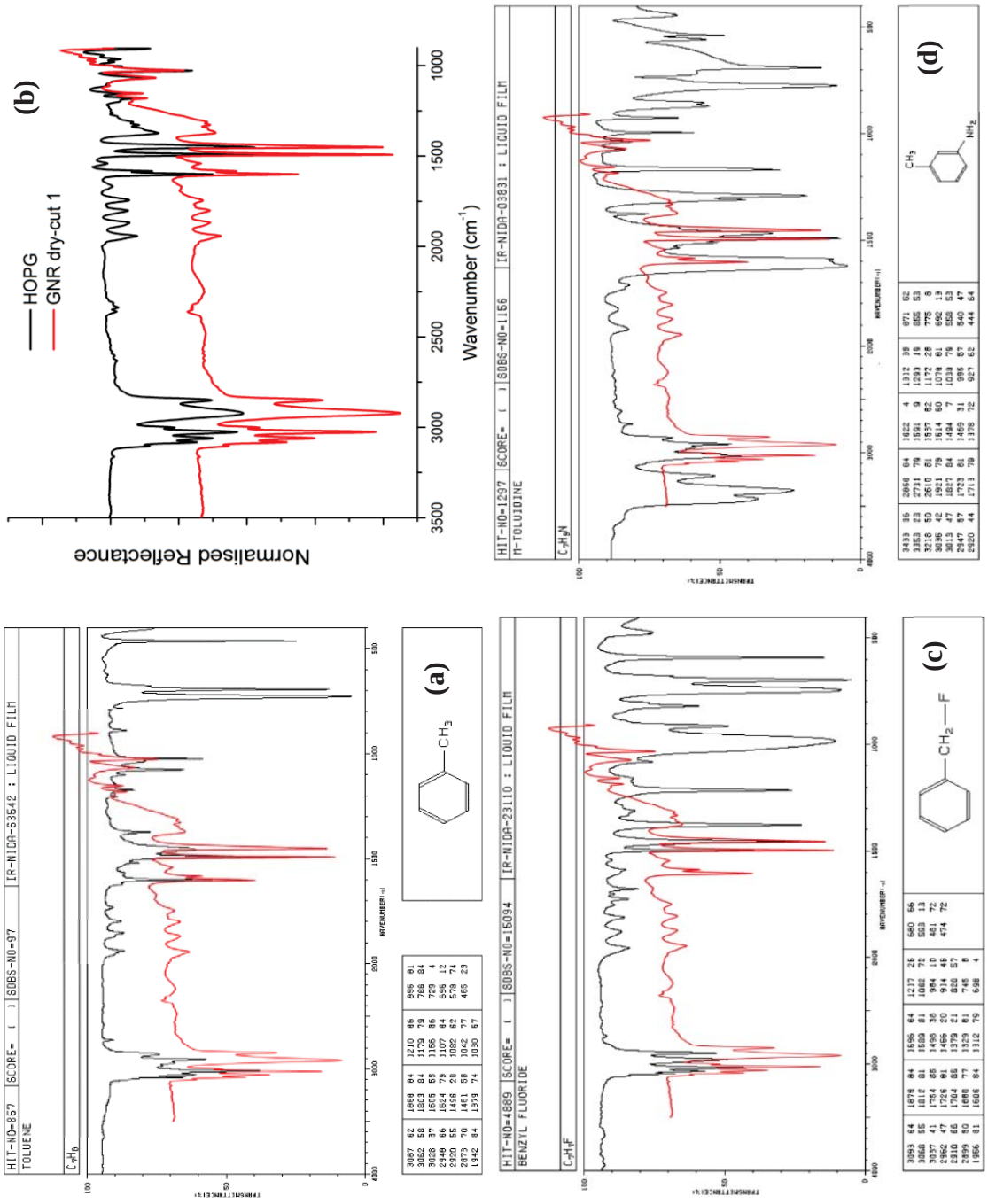

Figure 4. 10 - IR spectral comparisons between dry-cut (CVD-like) GNRs and: (a) toluene (SDBS), (b) mechanically cleaved HOPG experimental standard, (c) benzyl fluoride (SDBS), (d) m-toluidine (SDBS). Database spectra accessed from SDBSWeb.[118] SDBS comparisons were chosen based on the presence of combination modes in the 1600 cm^{-1} to 2000 cm^{-1} region.

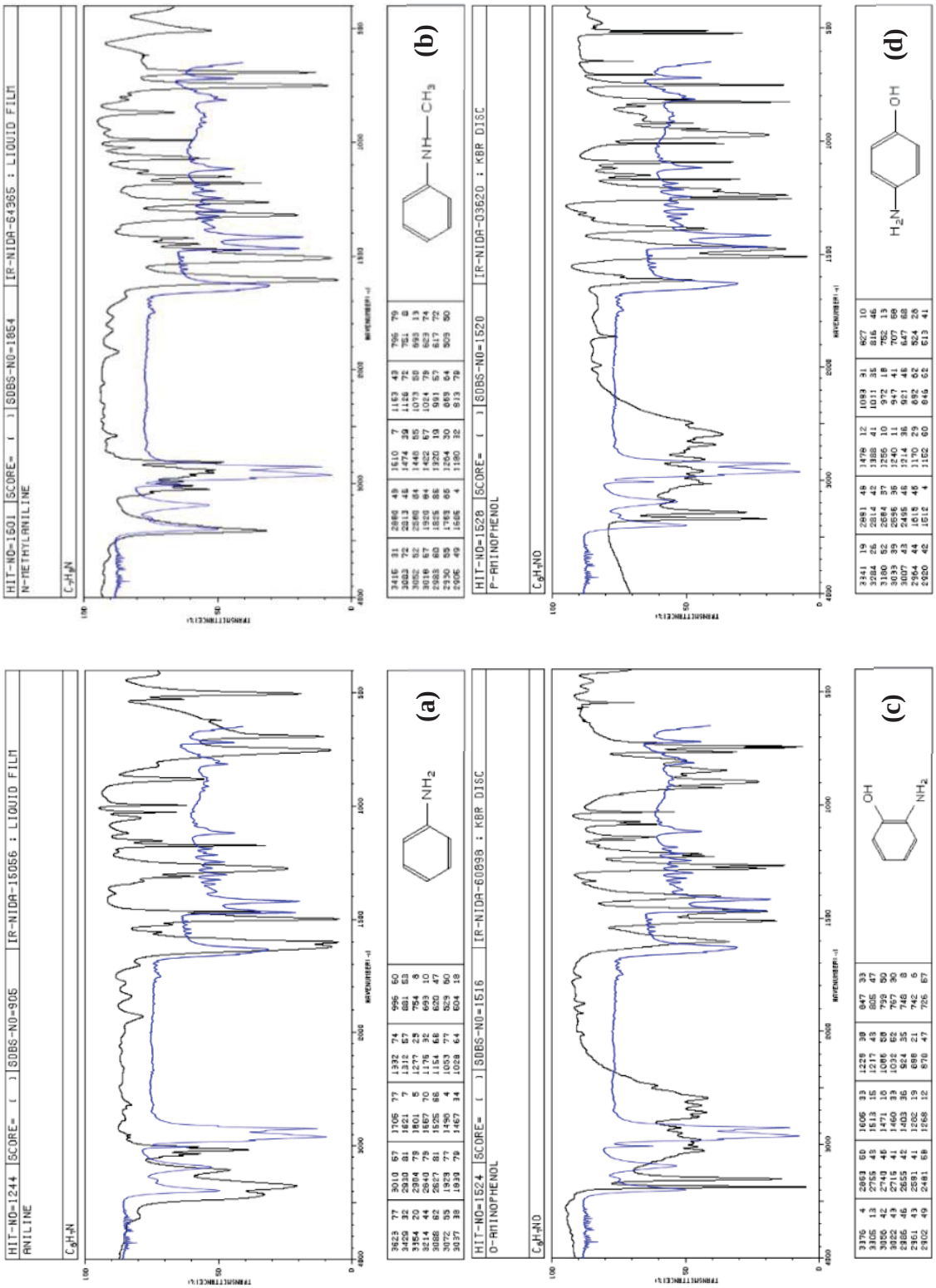

Figure 4. 11 - IR spectral comparisons between GNRs (dry-cut 2) and SDBS spectra of: (a) aniline, (b) N-Methylaniline, (c) *ortho*-Aminophenol, (d) *para*-Aminophenol. Database spectra accessed from SDBSWeb.[118] SDBS comparisons were chosen based on identity to peaks over 3000 cm^{-1}.

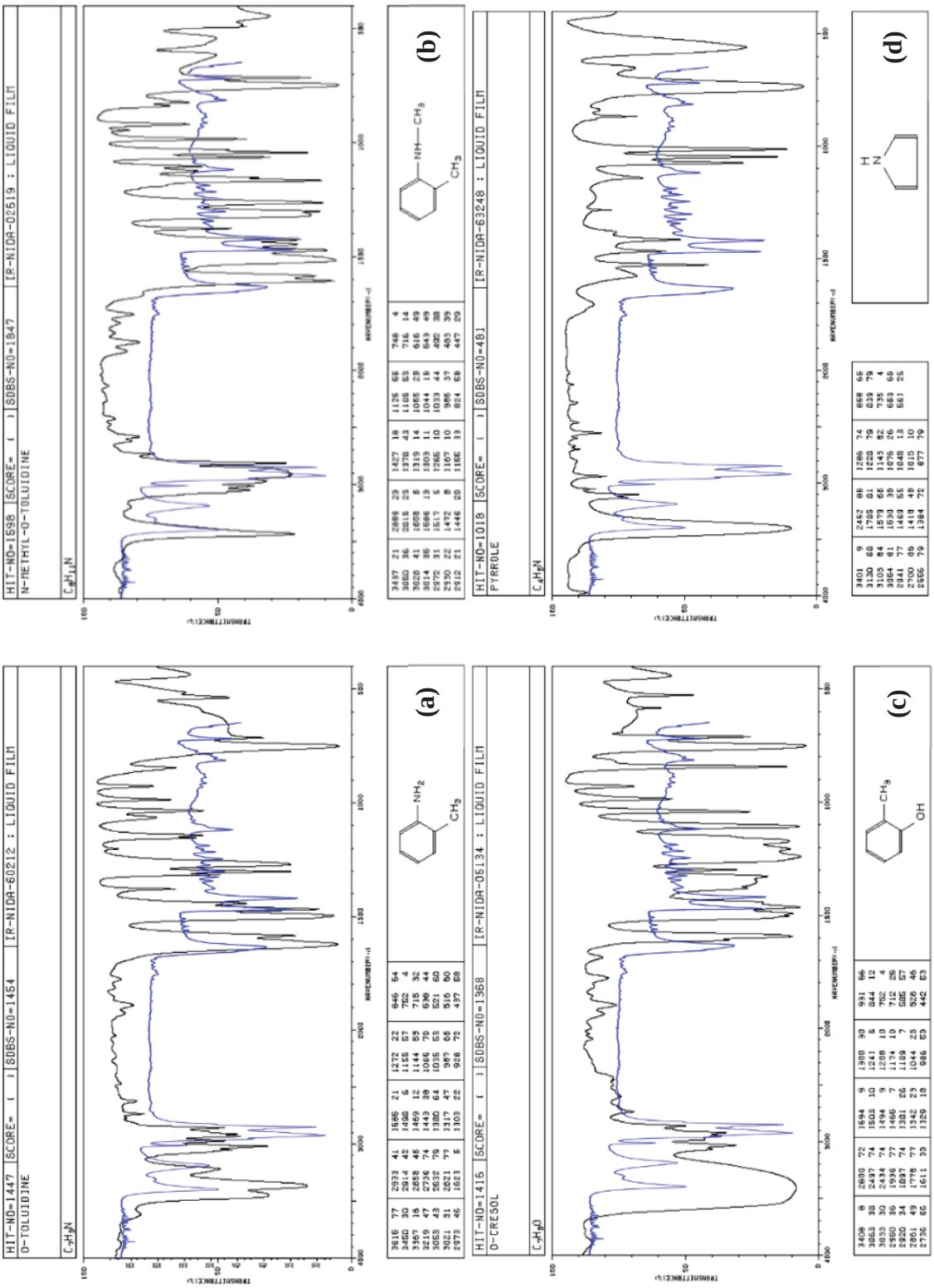

Figure 4. 12 - IR spectral comparisons between GNRs (dry-cut 2) and SDBS spectra of: (a) *ortho*-Toluidine, (b) N-Methyl-*ortho*-Toluidine, (c) *ortho*-Cresol, (d) pyrrole. Database spectra accessed from SDBSWeb.[118] SDBS comparisons were chosen based on identity to peaks over 3000 cm^{-1}.

of characteristic carboxylic acid peaks, this process seems rare, and may indicate a more complex mechanism to the incorporation of gas molecules at the edges. It should be noted that the exact identity of the functional groups causing each stretch is speculative, as the processes involved in edge rearrangement are not well understood, and changes to edge geometries and strain induced therein may alter vibration frequencies and the accuracy of peak assignments. Regardless, it is highly probable that various amine residues are present on the edges, as well as perhaps a variety of alcohol, alkyl and cycloalkane, and aromatic functional groups.

An interesting note is the relative sharpness of these X-H peaks when compared with functionalised material in chapter 5. These sharp peaks suggest there is a low degree of hydrogen-bonding (which typically broadens the signal of these peaks in IR) between the residues on as-cut material. This could indicate that these residues are sterically hindered and unable to interact, or spaced too far apart to hydrogen bond with their neighbours when unmodified (average H-bond distance is 3.0 Å).[123] The latter hypothesis may suggest a relatively low number of edge residues available for modification, which is discussed further in chapter 5.

4.4 UV-vis Spectroscopy

UV-vis spectroscopy measures the absorption of light from near-ultra-violet, visible, and near-infrared regions as it passes through a sample. These absorptions correspond to discrete electronic excitations within the molecules present, and define the perceived colour of a sample. UV-vis spectroscopy is often used to quantify the concentrations of molecules in solution.

Graphene absorbs at all wavelengths along the UV-vis spectrum (see Figure 4. 13), which is one of its unique optical properties.[124] While single layer graphene is nearly

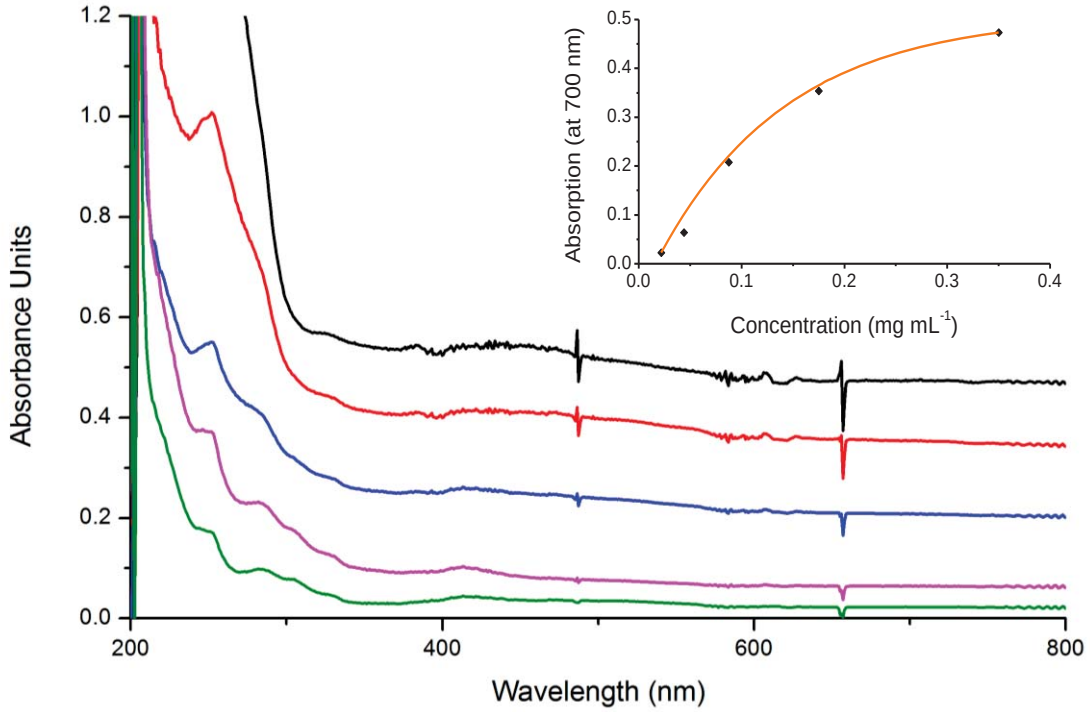

Figure 4. 13 - UV-vis absorption spectra of varying concentrations of GNR dispersed in IPA. The top trace (black) is at a concentration of 0.35 mg mL^{-1}, and each following trace (red, blue, pink, then green) is half the concentration of the one above it. Inset: GNR absorbances at 700 nm with respect to concentration. Note the non-linear relationship, which is discussed in section 4.4.

optically transparent, large quantities of graphene in solution or as a film are an intense black. This broad-spectrum absorption makes it difficult to isolate a single excitation peak for quantitative analysis, and there are several other challenges associated with the UV-vis spectroscopic quantification of liquid-phase exfoliated (LPE) graphene (explained below). Regardless, it is still often used in literature to quantify graphitic content in solutions.[125-127]

UV-vis spectroscopy has been used here mainly as a means of qualitative characterisation. When it has been used quantitatively (such as in the solvent exfoliation experiments) it has done so with respect to other solutions as relative absorptions. This is because it has been observed that the UV-vis absorption of graphene, especially GNRs and GNBs, is dependent on not only concentration, but also the exfoliation extent and aggregation. When exfoliated, more surface area is exposed and distributed through the solution resulting in greater absorption. This has been observed experimentally as the continued darkening of GNB solutions undergoing exfoliation well after particles are no longer visible. Literature has demonstrated that the transmittance of visible light through multi-layer graphene decreases exponentially with increasing layers.[128] This relationship also holds true for multi-layer graphene which is transferred serially post-synthesis to make larger stacks. This indicates aggregates will also behave this way. Therefore, the absorbance of one aggregate will be less than the sums of the same aggregate split in two, meaning there is a size-dependent masking of graphitic content by aggregates to UV-vis quantification. Moreover, poor dispersants are sometimes unable to sufficiently exfoliate GNR material, resulting in (faintly) cloudy solutions containing light-scattering particles which further decreases quantification accuracy.

4.4.1 Liquid-Phase Exfoliation of GNRs

Owing to the significantly reduced surface areas between layers in a GNB when compared to bulk graphite, mechanically fractured GNRs require less energy to exfoliate. As such it has been found that GNRs are easily dispersible in many of the common graphene solvents used in literature via low-power bath sonication. Many other common solvents which are not normally used for graphene have also been shown to disperse GNRs (see Figure 4. 14). Current techniques for liquid phase exfoliation of graphitic nanomaterials require harsh techniques which often induce damage. However, low-power sonication is a relatively gentle technique, and can be performed in a wide range of solvents. An exfoliation study was conducted using UV-vis spectroscopy to demonstrate the relative efficiencies of many common solvents, and is presented in Figure 4. 14.

The results of the solvent study agree with many observations made during this research. Low boiling point alcohols are generally effective at dispersing GNRs. Of those, EtOH showed the highest concentrations of dispersed material in the solvent experiments, and was observed throughout this research to be useful for quickly dispersing material for characterisation. This may be in part due to solvent-induced wrinkling and coiling mentioned earlier,[116] which would help to physically peel and exfoliate the graphene without the requirement of external forces. While an effective solvent for dispersing GNRs, EtOH is relatively ineffective at maintaining a stable dispersion over time. When exfoliated by sonication, EtOH solutions are slightly cloudy, indicating light-scattering aggregates are still present even after long periods of higher power sonication, which may explain the poor stability over time. Conversely, dichloromethane (DCM) and chloroform ($CHCl_3$) are not as effective as EtOH at initial dispersibility, but are very effective at maintaining stable dispersions, with some stock solutions retaining their grey colour after many months. Dimethylformamide (DMF), a common literature solvent for graphene,

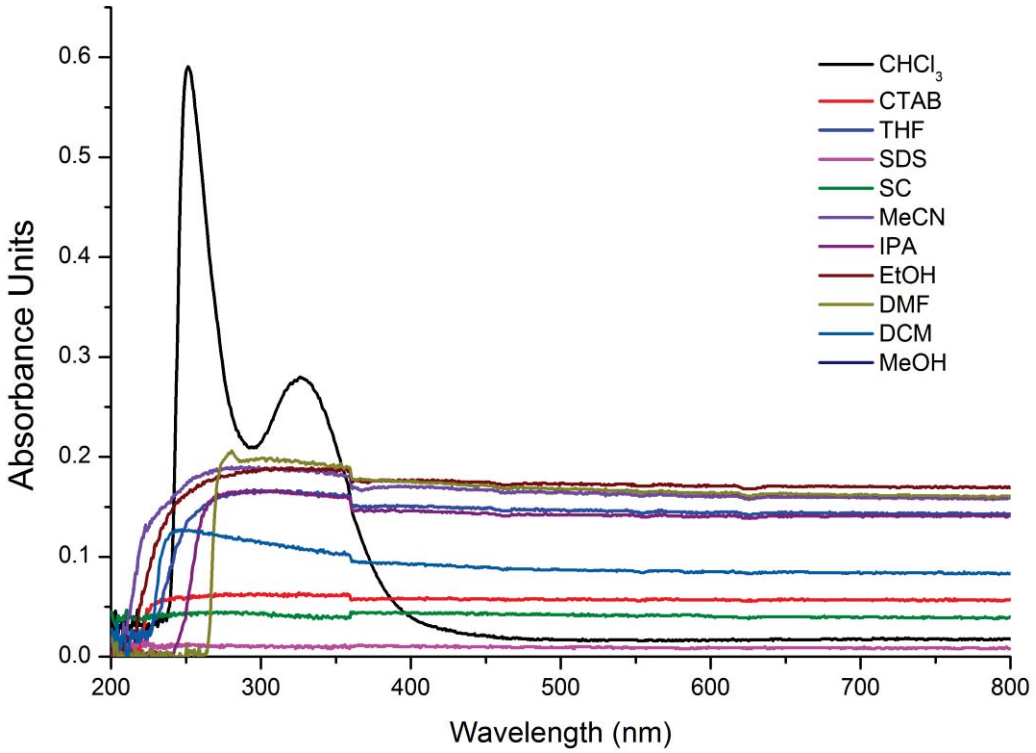

Figure 4. 14 - UV-vis quantification study on the dispersibility of GNRs in various common solvents. GNRs dispersed via bath-sonication at 50% power for 24 hours.

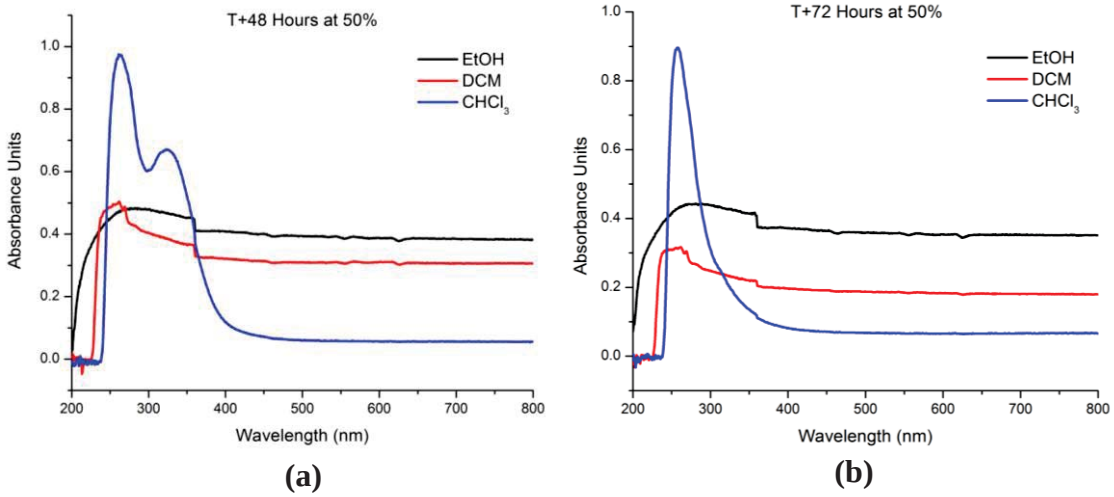

(a) **(b)**

Figure 4. 15 - UV-vis spectra of DCM and $CHCl_3$ dispersed GNRs after (a) 48 hours of sonication at 50% power and (b) 72 hours of sonication at 50% power.

was also found to have good dispersibility and stability. The three detergent-water solutions (CTAB (cetyltrimethylammonium bromide), sodium cholate (SC), and sodium dodecyl sulfate (SDS)) performed poorly in initial dispersibility, mainly because surfactant-water solutions tend to have low saturation concentrations.

The UV-vis spectrum of $CHCl_3$ is unique from the rest, as was the solution's appearance, which became pale yellow in colour. The spectrum of DCM is also different, showing a decreasing absorbance from $250 - 350$ nm and a faint yellow tint in an otherwise pale grey solution. Repeat samples of GNRs in $CHCl_3$ and DCM sonicated at 50% power for 48 hours show very little difference, but at 72 hours the peak in $CHCl_3$ around 330 nm is lost (Figure 4. 15). Over 72 hours, the physical appearance of the $CHCl_3$ solutions changes slightly, becoming more intensely coloured but still a pale yellow. These solutions showed good stability, with no significant precipitation over several days, other than a small coating of graphitic powder which slowly built up on the inside of the glass vial, above the level of solvent. The slight decrease in absorption for DCM from 48 to 72 hours is attributed to this effect. Due to the remarkable stability of the $CHCl_3$-dispersed GNRs, sonication induced scission (see below) was considered as a possible cause of the colour change, but the Raman spectrum of this sonicated material shows very little change to the I_D:I_G ratio (see Appendix 1, Figure A1. 6). After evaporating the solvent, the dried powder was a grey colour (much like ordinary graphene), and re-suspending in EtOH then gave a grey solution. Therefore, the yellow colour is likely caused by solvent interactions. $CHCl_3$ induced p-doping via adhesion to graphene has been identified in literature,[116, 129] and it has been shown that the doping of graphene quantum dots results in the appearance of UV-vis peaks between 260 nm and 360 nm based on the type of doping, and the dopant molecule used.[130] These results suggest that the $CHCl_3$ molecules are packing densely on the surface of the GNRs in a

highly-ordered fashion, which alters its polarity and dielectric properties, thereby altering the optical response of the material. Solvent removal causes the $CHCl_3$ to desorb as it evaporates and thus restores the normal properties of the GNRs.

4.5 Scission

The sonication-induced scission of graphene refers to the random fracturing of relatively large sheets when exposed to strong shear forces while sonicating, which generates smaller, less ordered graphene fragments. Scission has been reported a number of times in literature,[131-132] and can be identified via a number of consequences, including increased I_D:I_G ratios,[125] the presence of oxygenated species (e.g. GO),[133] decreased average flake size, and increased solubility and dispersion stability. Therefore, it was assumed that scission would occur in GNRs, but to a lesser extent, as the high aspect ratios and relatively low masses of GNRs mean shear forces generated by sonication are not as significant.[105] While scission of small GNRs is yet to be observed, scission of relatively wide GNRs ($500 - 1000$ nm) has been directly observed using TEM, and is shown in Figure 4. 16. Their larger sizes mean they will be more prone to scission events than the $50 - 100$ nm wide GNRs typically used.[105, 134-135]

The GNRs in Figure 4. 16 were prepared by exfoliation with CTAB surfactant in water. Cracks in the GNR are clearly visible in these images, some running all the way through, and some only part way. Consider the details in Figure 4. 16a: a piece to the left looks like it has fallen off, and a piece to the right has a crack and fold which matches the adjacent section nicely. It is unlikely that these cleavage events happened solely during sonication, due to the nature of Brownian motion dispersing these fragments in solution. One possible scenario is that the CTAB acts similarly to the polymers used in the sonication-induced synthesis of GNRs from graphene flakes[13] by stabilising parts of the GNR and allowing fracturing to occur along non-stabilised sections. It is also possible

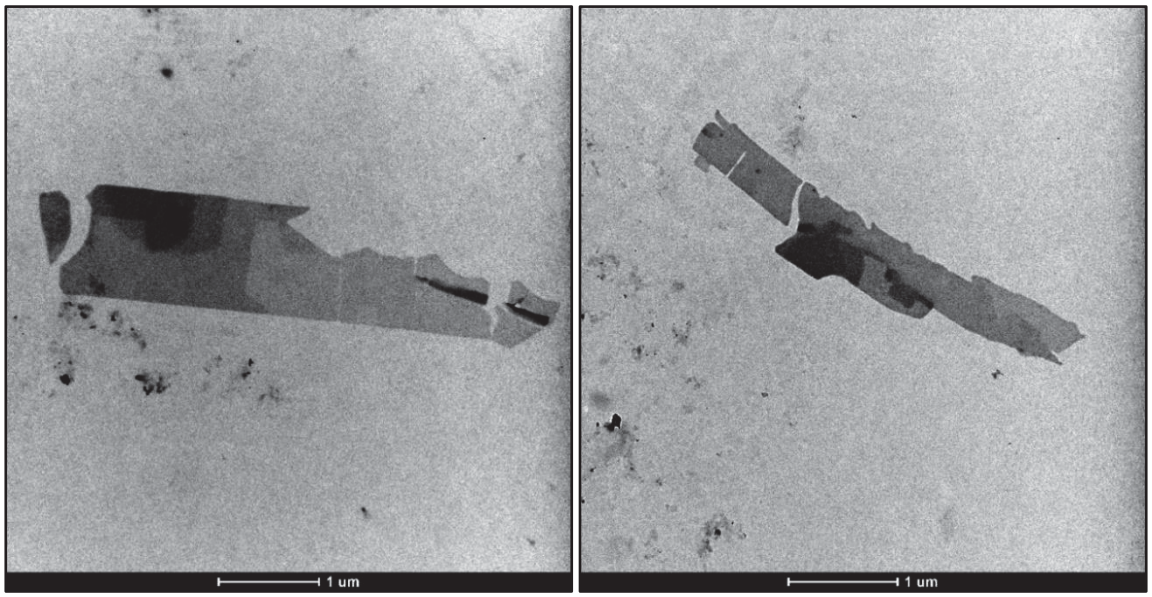

(a) **(b)**

Figure 4. 16 - TEM images illustrating sonication-induced scission of large width GNRs. These GNRs were dispersed using CTAB surfactant in water. (a) A 1 μm wide GNR and (b) a 500 nm wide GNR which have been damaged by scission events.

that CTAB could be acting like a coating or glue, protecting and holding sections of the ribbon together. The folds on the right-hand side of the GNR in, (a), seem to be matching, as do the edges between them. These sorts of folds typically form upon deposition (GNRs and flakes are assumed to be constantly flexing in solution), so it is most likely that the fracture separating the two folds happened after deposition. It is possible that the formvar may be enacting micromechanical stresses onto the GNR after deposition, during drying and handling or upon exposure to the vacuum of the TEM. In fact, this could be a single-molecule example of mechanical fracturing of graphene. Regardless, at some point in the sample preparation after GNR deposition, stress is applied to the GNRs to induce fracturing. Looking at the top section on the right, it seems that a piece of GNR is missing – that it has already cleaved off before deposition. Therefore, sonication must be capable of inducing scission on its own, and the observed GNRs in Figure 4. 16 must be the result of sonication-induced scission, defect introduction, and subsequent fracturing via external stresses. The fact that scission has only been observed to this degree in large samples, and the overwhelming abundance of intact GNRs observed indicates that such scission events are relatively rare, especially for smaller GNRs. Sonication-induced scission of 100 nm wide GNRs has been explored in EtOH and $CHCl_3$ using Raman to quantify the changes in I_D:I_G ratios of the samples. The results found no significant changes over 72 hours of sonication at 50% power in EtOH or $CHCl_3$ (see Figure 4. 17). From these results, I conclude that scission of smaller GNRs in EtOH and $CHCl_3$ is negligible, but further studies are required to determine whether scission is facilitated or catalysed by detergents such as CTAB or the contents of reaction mixtures during functionalisation. This can be investigated using Raman to probe overall quality and follow the generation of new edges, while IR can be used to identify chemical changes in edge species.

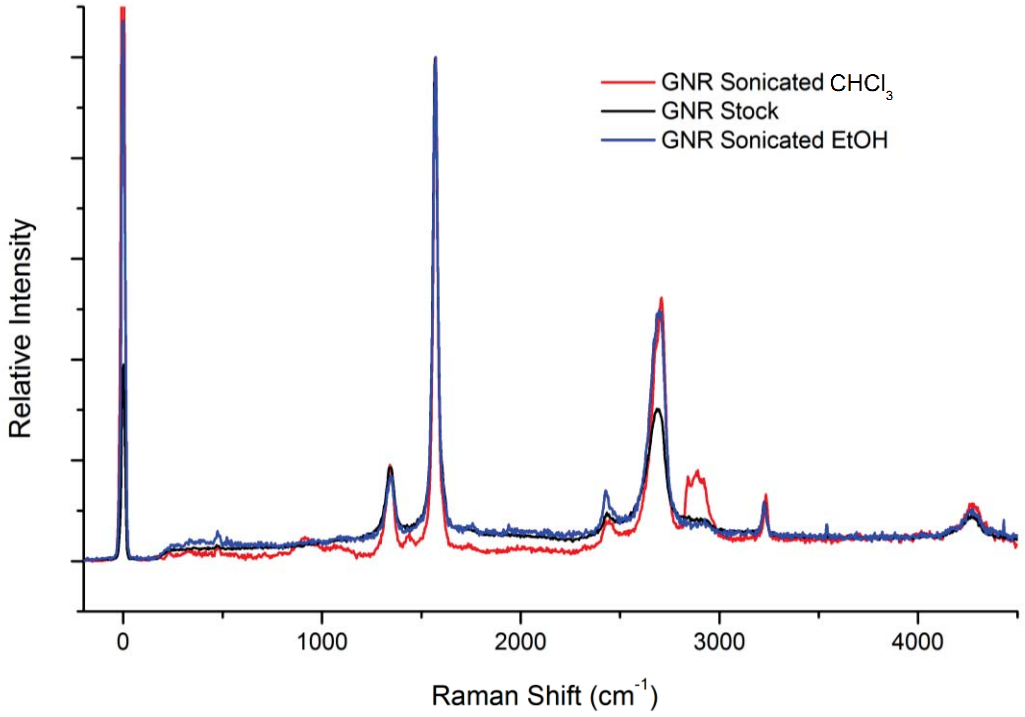

Figure 4. 17 - Raman spectra of unsonicated stock GNR (black), and GNRs after 72 hours of sonication in $CHCl_3$ (red) and EtOH (blue). Spectra normalised against G band. No significant changes in I_D:I_G ratios observed. Note the increase in 2D peak ($\sim 2650\ cm^{-1}$) of sonicated spectra, which indicates fewer layer material and a higher degree of exfoliation.

4.6 Summary

The structural properties of GNRs synthesised from mechanical fracturing in air have been characterised and compared to wet-cut materials and published literature methods. The unique flexibility of GNR products has been demonstrated via AFM and TEM, and the ability to control the conformations of these materials via exfoliation has been discussed. The quality of dry-cut material has been shown to exceed that of wet-cut, showing ~25% lower I_D:I_G ratios in Raman spectroscopy, which is, to my knowledge the lowest, and therefore represents the highest quality, of any top-down synthetic method reported in literature to date. While mechanical fracturing in air generates relatively smooth edges, the nature of the fracturing technique and resulting edge-rearrangements mean these GNRs will likely not match bottom-up synthetic approaches for edge quality and structural purity. Evidence for this edge-rearrangement hypothesis discussed by Mohanty *et al*. has also been provided using SEIRS data, which shows bands indicative of various N-H stretches from the edges of dry-cut GNRs incorporated from the atmosphere during rearrangement. The exfoliation of these GNRs into manageable dispersions and solutions has been demonstrated in a range of common solvents, with $CHCl_3$, DCM, and EtOH demonstrating high dispersibility and/or stabilities over time. Sonication-induced scission events of large-width GNRs have also been identified via TEM imaging, although this effect is negligible for smaller GNRs. More research is required to identify the potential catalysts of scission observed in larger GNRs.

Chapter 5: Functionalisation

Functionalisation of graphene via covalent and non-covalent strategies modifies graphene's properties and enables and facilitates application integration. Covalent modification can be achieved using reactive species which typically target the basal plane,[59-66] and more benign organic synthetic techniques which target defect sites and edge residues,[67-69] such as those in graphene oxides. Non-covalent functionalisation involves modifying graphene without perturbing the material's quality,[71] typically adhering to the basal plane using hydrophobic interactions, electrostatic interactions, π-π stacking, and van der Waals forces.[70] These types of modifications are often used to increase solubility, facilitate self-assembly, and generate composite materials.[4, 72-74] Additionally, graphene has found many uses in biological systems,[75-78] where biofunctionalisation utilises the above strategies to tailor graphene for specific biotechnological applications.[75] This chapter explores the functionalisation of mechanically fractured GNRs using organic synthetic routes and non-covalent interactions.

5.1 Covalent Functionalisation

Modifying the edge residues of graphene provides accessibility via the vast and established toolkits of organic and materials chemistries. Edge functionalisation allows modification for applications without disrupting the sp^2 network, thus preserving graphene's unique properties.

Previous work by members of our group has demonstrated that wet-cut GNR material can be modified using Steglich esterification protocols which target nucleophilic residues on graphene's edges, similar to GO esterification and amidation protocols in literature.[67-68] When cut, a range of oxygen and nitrogen containing residues are

incorporated into the edge structures during rearrangement. As such, a variety of edge moieties are believed to be present in as-cut material. The first step in modifying edges, therefore, is to change as many residues as possible into a single functional group. This is typically done via oxidation or reduction. Reduction uses sodium borohydride ($NaBH_4$) or lithium aluminium hydride ($LiAlH_4$) to reduce the edges to nucleophilic residues depending on the situations. $NaBH_4$ is generally used when carboxylic acid functionality is desired, such as when restoring quality to GO or when preserving esters and amide residues. $LiAlH_4$ is used when attempting to direct as many edge residues as possible to nucleophiles. Molecules of interest bearing carboxylic acid residues can then be functionalised to the edges.

Alternatively, oxidation of as-cut GNRs can be used to generate carboxylic acids on edge residues. The advantage of carboxylic acids on the edges is that they can react with both alcohols and amines to form esters and amides respectively, allowing for a wider range of chemical functionalisations. In addition, the ability to form amides provides a much more stable linker, which is useful for applications involving water where hydrolysis of ester linkers will cause loss of the functional groups. The challenge with oxidising edges is to do so without damaging or perturbing the basal plane. This requires careful consideration of oxidising agent, reaction duration, and chemical environment to ensure the material quality and structure are maintained. For oxidation reactions, pyridinium dichromate (PDC) was used in DMF to produce carboxylic acids from aliphatic oxygen-containing residues. Potassium permanganate ($KMnO_4$) was also used in a variant of a Hummer's oxidation procedure[106] to aggressively oxidise GNRs to graphene-oxide nanoribbons (GONRs). These GONRs are discussed further below.

5.2 Functional Standard – Graphene Oxide

A unit cell which contains two carbon atoms per $\sim 6.98\times10^{-20}$ m^2, as illustrated in Figure 5. 1, can be used to calculate the approximate number of carbon atoms in a GNR. For a GNR 100 nm wide and 1 μm long (1: 10 aspect ratio), the number of carbon atoms is calculated to be approximately 2.85×10^{6} (see Appendix 2 for full calculations). This GNR will have a perimeter of 2.2 μm, and assuming perfect zigzag edges along all sides, there will be at most ~8,950 edge atoms available for functionalisation. As a ratio of edge to basal plane atoms, this comes to $\sim 1: 320$. Even if assuming perfect functionalisation of each edge residue, this incredibly small percentage (0.3125%) of functional residues makes characterisation of edge modifications extremely difficult using spectroscopic methods, as their signals are usually dwarfed by those coming from the basal plane. In practice, the actual identity of edge structures, steric hindrances and reaction yields make this percentage much lower, and the challenge much more difficult. Consequently, enhanced spectroscopy techniques such as SERS and SEIRS techniques have been employed to varying degrees of success. For this reason, non-spectroscopic

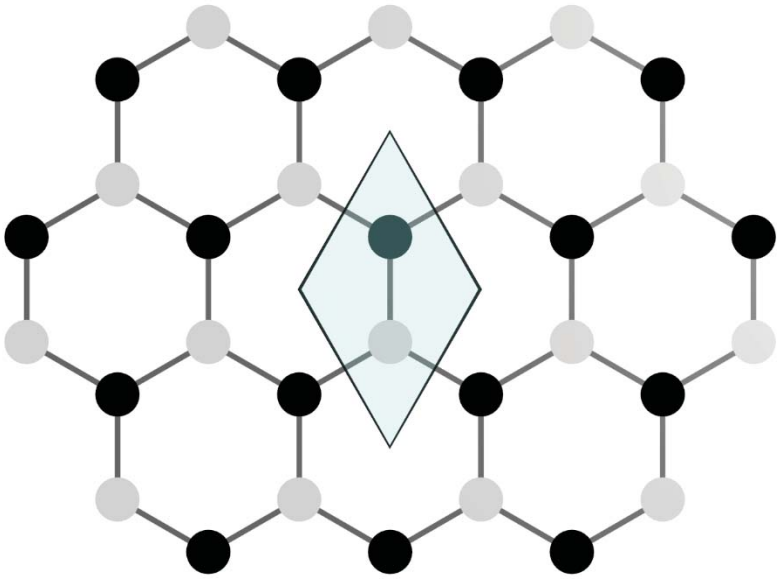

Figure 5. 1 - A unit cell of graphene (shaded rhombus) gives 2 carbon atoms per $\sim 6.98\times10^{-20}$ m^2 of surface area.

methods utilising gold nanoparticles (AuNps) as characterisation reporters for TEM and AFM have also been utilised to identify modifications.

Graphene oxide (GO) is a form of highly-oxidised graphene which is typically generated from low-quality graphitic material. The oxidation process significantly diminishes the unique properties of graphene and confers water solubility through oxidised basal plane and edge defects. Consequently, GO has a large number of carboxylic acid residues, making it a very useful analogue for trialling chemical reactions. Figure 5. 2 shows a schematic for the modification of GO with cysteamine (CA) molecules, which form amide bonds with the carboxylic acid residues on the GO surfaces. This modification was performed using 1-ethyl-3-(3-dimethylaminopropyl)carbodiimide (EDC) or N,N'-dicyclohexylcarbodiimide (DCC) catalysts in buffered water or DMF respectively. Highly-oxidised GO material is quite soluble in water, but poorly soluble in non-polar organic solvents. Reactions performed in DMF required purification of less oxidised material from the water-soluble GO samples, but are simpler to perform and do not need strict control over pH and temperature. Functionalisation with CA provides a thiol (SH) residue available for bonding with gold. Therefore, AuNps are added to bind to functionalised residues via covalent bonds to the sulfur atoms, acting as a reporter for successful functionalisation.

Nanoparticles of 10 nm and 20 nm diameters were used, which are large enough to be easily identified using AFM, and electronically dense enough to be clearly identified using TEM. Figure 5. 3 shows AFM scans of GO-cysteamine (GO-CA) samples where, in the topography scans, the bound AuNps are visible as bright spots on faint GO-CA flakes. The flakes become easier to identify in the phase scan, which shows them darker than the background mica. These scans and subsequent TEM images (c-h) show that AuNps selectively bind to the GO-CA flakes, indicating successful functionalisation.

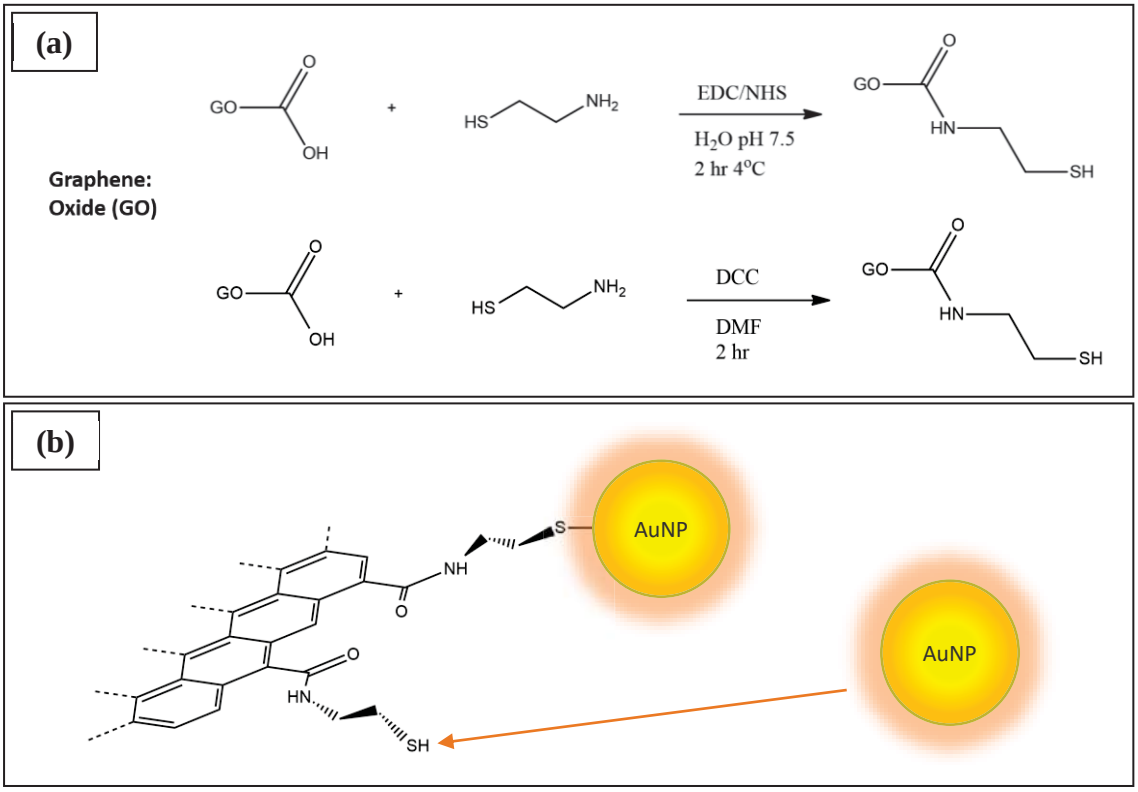

Figure 5. 2 - (a) Reaction schemes of GO-CA modifications. (b) Schematic diagram of GO-CA functionalisation by AuNps. See Appendix 1, Figure A1. 4 for catalyst structures.

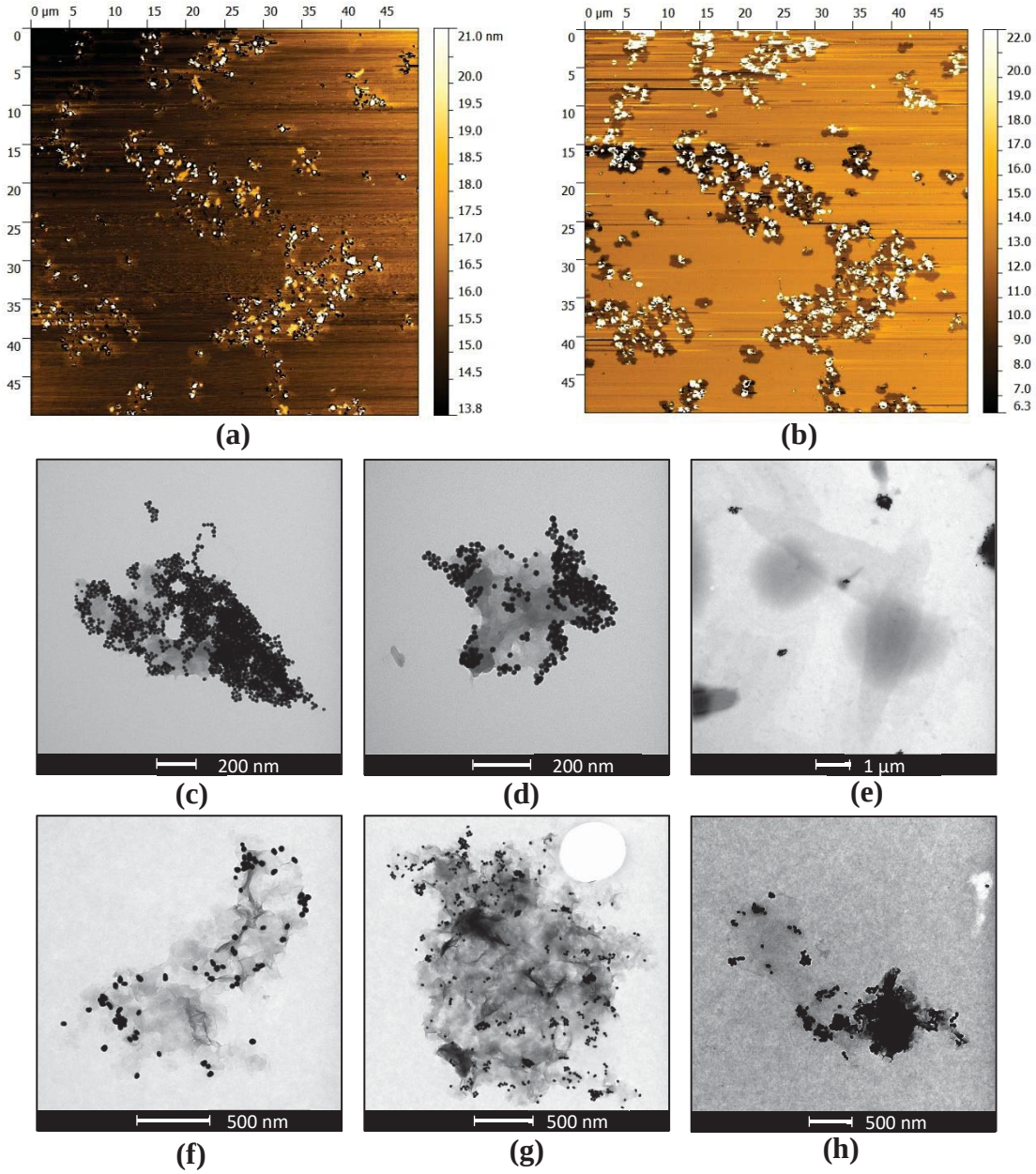

Figure 5. 3 - AFM and TEM images of thiolated GO (GO-CA) and AuNps. (a) Topography scan of AuNp-decorated GO-CA. (b) Phase contrast scan of (a). (c-e) TEM images of GO-CA AuNp via the H_2O EDC synthetic route. (f-h) TEM images of GO-CA AuNp via the DMF DCC synthetic route.

Closely examining the phase contrast data reveals that many of the smaller flakes have less gold attached than larger ones. These larger flakes also seem to have holes throughout them. TEM identifies these larger flakes as multi-layer, terraced particles (as determined by the contrasting layers in the flake). Such a terraced GO flake is formed when multi-layer graphite sections are oxidised but not fully exfoliated under the acidic conditions in the GO synthesis procedure (also observed for GONRs using same protocol). These flakes will have edges along each of the terraced layers and a significantly larger surface area than exfoliated 2D GO. Consequently, these will have a large number of exposed residues that can be modified to allow AuNps to bind over most of the flake. Well-exfoliated GO such as the flake in Figure 5. 3e does not bind AuNps effectively. In fact, there are very few AuNps bound to the surface or edges of the flat GO shown here, and relatively low amounts bound to the flattened section of the flake in (h). The reason for this may be due to the relatively large size of the nanoparticles, which is investigated with GONRs below. AuNps will be anchored by far fewer bonds on flat edges than terraced flakes. Gold-thiol bond strengths have been investigated in the literature, where the forces involved in single and multiple thiol-gold interactions have been quantified.[136] This study found that under mechanical stresses the inter-particle gold-gold bonds will typically break before the gold-thiol bond. This suggests that low densities of thiol residues on graphene may be unable to anchor relatively massive particles, and shear forces could result in nanoparticle cleavage. Cleavage would likely passivate those residues by leaving a few atoms of gold behind, and has been observed macroscopically in functionalised GO, using sonication to drive cleavage and generating an insoluble white precipitate.

Graphene functionalisation with gold (and other) nanoparticles has been demonstrated in literature via many mechanisms,[63, 137-141] most of which utilise multiple

points of contact or a combination of covalent and non-covalent interactions to maximise binding strengths. Methods using pre-synthesised nanoparticles and covalent interactions usually take advantage of the functional groups of capping agents on the surface of the nanoparticle to form bonds with the graphene. This can be achieved via reactive species, electrostatic interactions, and organic chemistries – the latter of which often uses GO or reduced GO due to the abundance of epoxy and carboxylic acid residues. These studies are difficult to compare to this work, as these nanoparticle functionalisations are fundamentally different with respect to the number and strengths of anchor points, and the specificity of functionalisation (edges or basal plane). However, one study demonstrates a similar method to this work, using GO and reduced GO to selectively bind AuNps with CA linkers and gold nanoparticles.[142] This study used an inhomogeneous mixture of AuNp sizes, ranging from ~ 5 nm to ~ 25 nm, and demonstrated both general and edge-specific binding of AuNps on GO and reduced GO flakes respectively. Binding of large nanoparticles is seen, but smaller AuNps seem to dominate tightly-packed edges. This may suggest smaller nanoparticles bind to these thiol residues easier, but does not exclude the capability for larger particles to bind. The binding efficiencies of AuNps with respect to size was examined experimentally with GONRs (see below), using commercially obtained 10 nm and 20 nm AuNps, and 20 nm lab-synthesised AuNps (see chapter 2.13 for synthetic details), but these results are inconclusive. It was observed that the 20 nm lab-synthesised AuNps were able to bind very well to thiolated GNRs, while the bought 20 nm AuNps showed very little significant selective binding (see Appendix 1, Figure A1. 5 for comparison). Further work is required to determine the cause of this discrepancy.

5.3 GNR Functionalisation

After optimising the reactions on GO, the procedures were adapted and repeated for GNRs. TEM data of CA-modified, PDC-oxidised GNRs in Figure 5. 4 show the same effects as GO-CA when mixed with AuNps, where the gold seems to bind preferentially to the flake impurities. While some GNRs were found with nanoparticles, these were in the minority, and most flakes were well decorated. GNR stacks would be expected to contain a high-density of functionalised residues along the edges of the layers, so it is surprising that these are not more decorated. Based on the images in Figure 5. 4, graphitic material is being successfully functionalised. The preferential binding to flakes and aggregates may be a consequence of increased surface areas. As for the lack of functionalisation on GNR stacks, it is likely that these sections were not well-exfoliated, and have remained as stacks throughout the functionalisation procedures (which are performed under constant sonication). Therefore, the ribbon edges would not have been fully exposed to the reaction mixture and consequently are expected to be relatively unfunctionalised. In addition, those exfoliated and functionalised single-to-few layer GNRs may not have sufficiently high densities of functional groups to anchor the AuNps. It should also be noted that single-layer graphene is difficult to see using this relatively low-resolution TEM.

To assist with data interpretation, IR and Raman spectra of small molecule analogues of graphene (TBDBPP-ovalene, Figure 5. 5) and CA modified graphene were calculated and used to predict spectral changes associated with CA functionalisation of GNRs. Density functional theory calculations were performed using Amsterdam Density Functional (ADF) software,[143] with Perdew-Burke-Ernzerhof (PBE) functional and a double-zeta basis set with one polarisation function (DZP). These simplified analogues use a single cysteamine edge residue as it is expected to appear on a pristine GNR edge

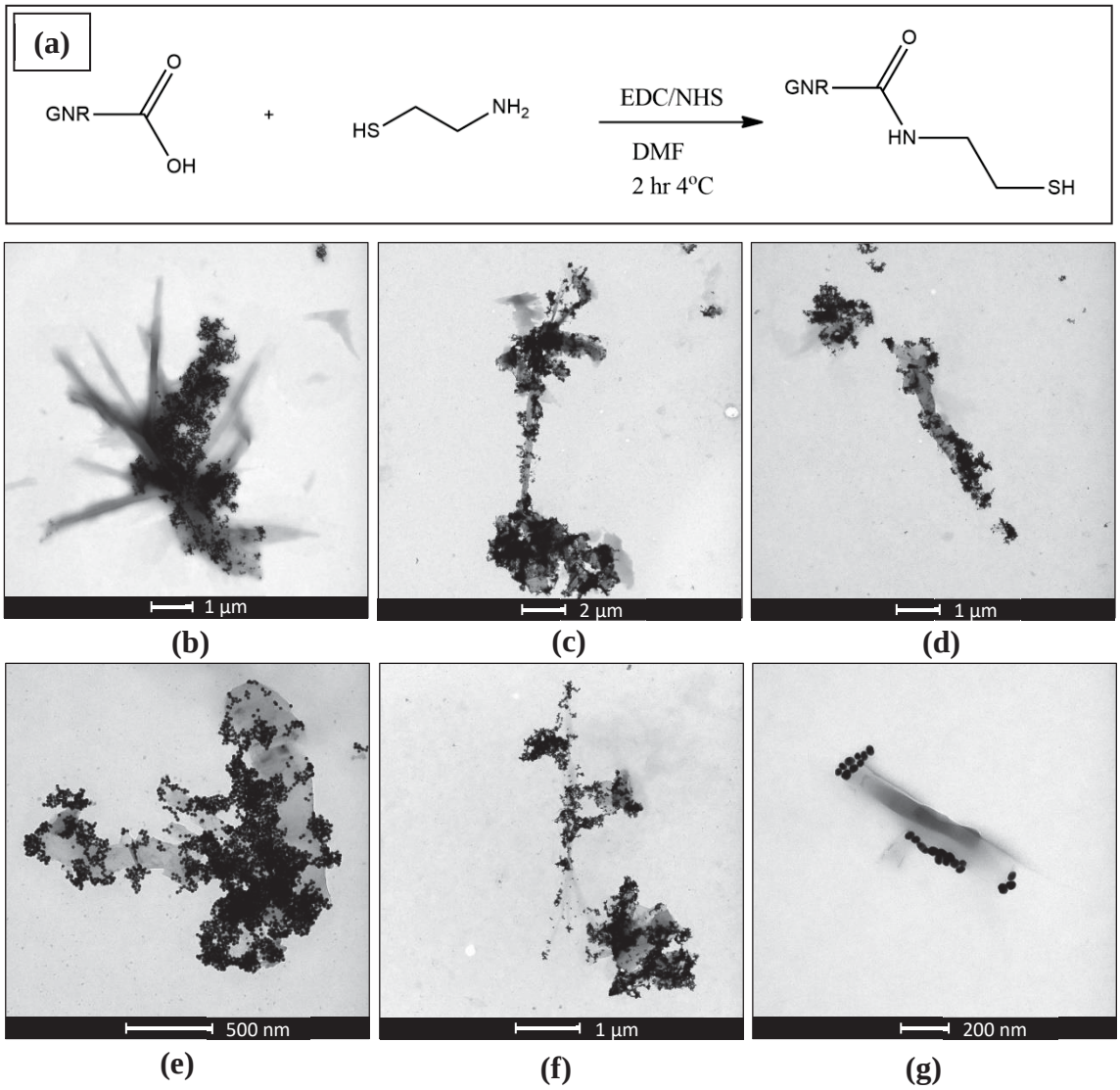

Figure 5. 4 - GNR functionalisation with CA. (a) Reaction scheme for the modification of GNRs with CA. (b-g) TEM images of AuNp-functionalised GNRs and flake impurities.

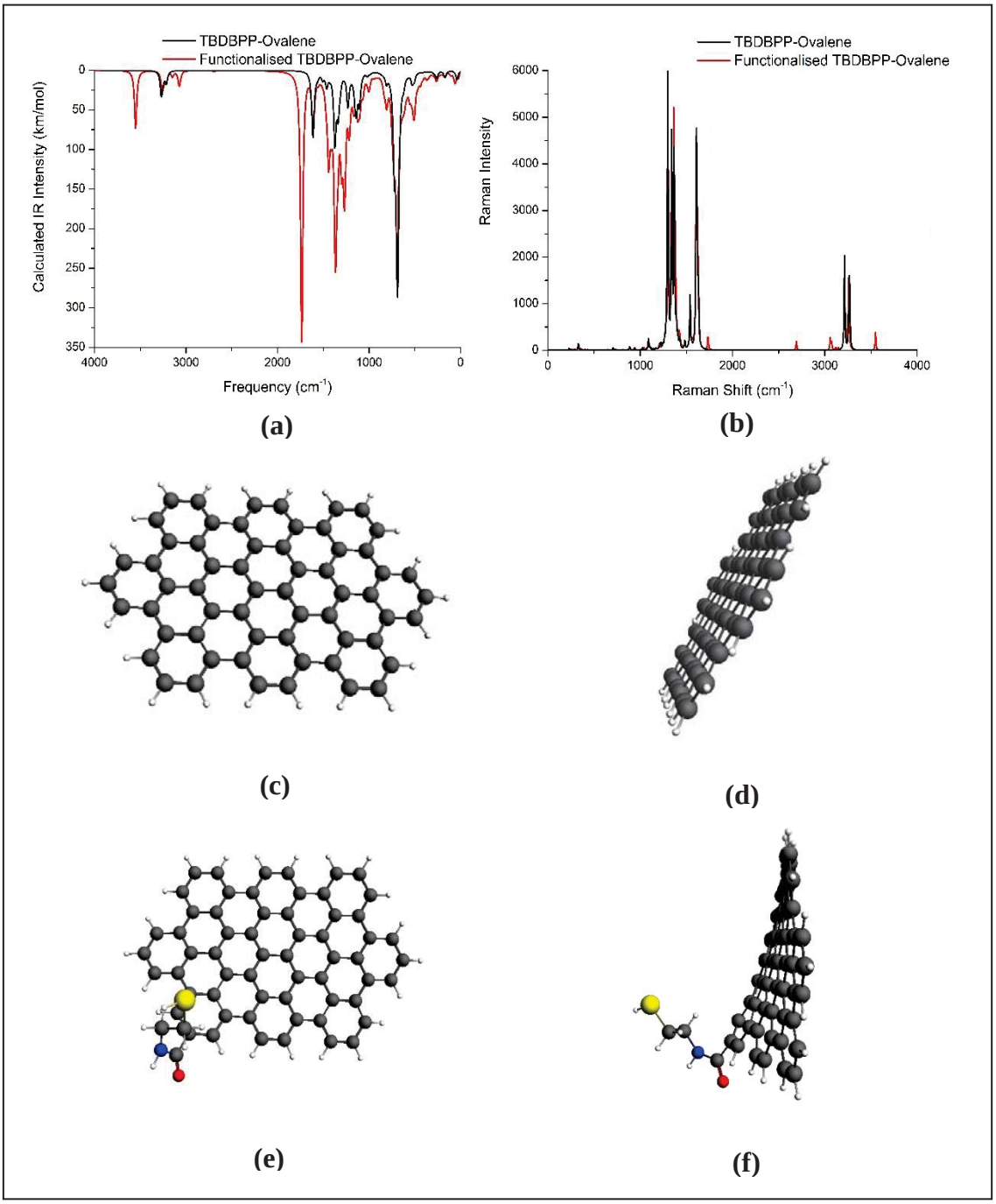

Figure 5. 5 - DFT calculations with PBE functional and DZP basis set, performed for CA-functionalised graphene analogue TBDBPP-ovalene. (a) Calculated IR spectra of modified (red line) and unmodified (black line) ovalene. (b) Calculated Raman spectra of modified (red line) and unmodified (black line) ovalene. (c) Unmodified ovalene viewed square and (d) side on. (e) Modified ovalene viewed square and (f) side on to show the functional group conformation and warping of graphitic plane.

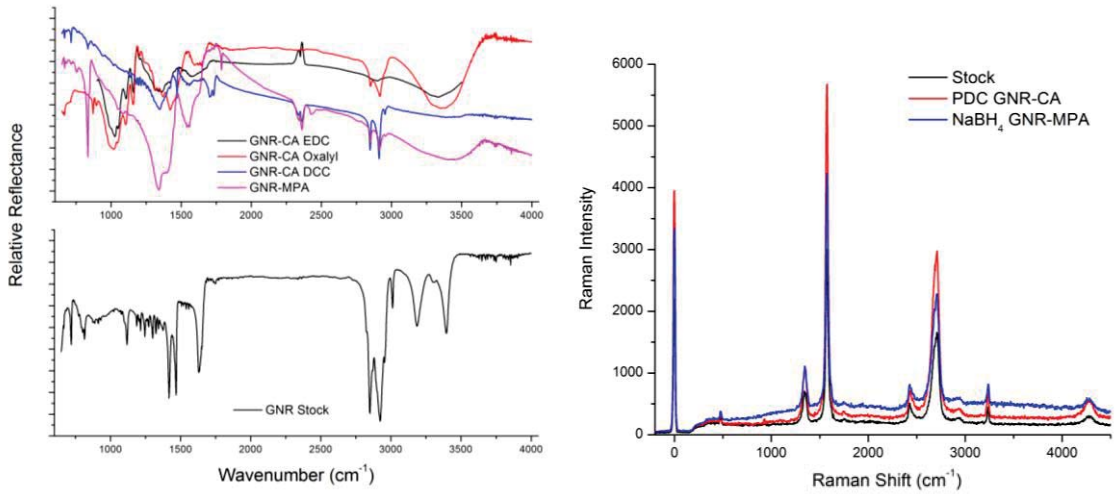

(a) **(b)**

Figure 5. 6 - (a) IR spectra comparisons of (top) various GNR thiol modifications and (bottom) unmodified GNRs. GNR-CA EDC used the EDC/NHS catalysts, GNR-CA DCC used the DCC catalyst, GNR-CA Oxalyl used an oxalyl chloride catalyst (see methods for details), GNR-MPA used reaction of 3-mercaptopropionic acid (MPA) with $NaBH_4$-reduced GNRs. (b) Raman spectra of stock and functionalised GNRs, with (black) unmodified, (red) PDC oxidation then CA functionalised, and (blue) $NaBH_4$-reduced then MPA functionalised.

(see Figure 5. 5), and predict small but noticeable changes to the IR and Raman spectra. A number of new, albeit weak peaks are predicted to arise. In particular, new peaks at $3550\ \mathrm{cm}^{-1}$ and $1735\ \mathrm{cm}^{-1}$ correspond respectively to the amide N-H stretch, and a combination of unique stretches along the O=C-N section of the amide bond.

The $3550\ \mathrm{cm}^{-1}$ peak is already observed in the IR spectrum of as-cut material as part of the amide (NH) peaks (see Figure 4. 10). In functionalised material, however, this peak is significantly broadened, indicating a much higher density of functional groups allowing hydrogen bonding between neighbouring residues (see Figure 5. 6a). Raman analysis of the functionalised material did not identify any novel peaks (see Figure 5. 6b). The calculated intensities of the new peaks were low, and due to the low ratios of functional groups to basal plane atoms, a signal from modified residues was likely too small to identify.

5.3.1 Graphene Oxide Nanoribbon Functionalisation

In light of these findings, it was considered that the initial number of functionalisable residues on the GNRs may not provide enough final, functionalised residues to sufficiently decorate the edges. In order to increase the quantity of functionalised edge residues on GNRs, GONRs were synthesised using a modified Hummer's technique which utilises concentrated acid in the presence of oxidisers to produce water-soluble graphene. Here, the reaction was run for a much shorter time, with the aim of "lightly" oxidising the material to increase the number of functionalisations, while minimising the overall damage. The reaction is quenched on ice and yields a dilute mixture of products. This is then concentrated and purified by centrifugation at increasing speeds to yield fractions of GONRs with varying degrees of oxidation. A full range of products were generated, from unexfoliated GNBs to stable water-soluble GO fragments.

Centrifugation fractions from the mid-range of speeds were collected and used in functionalisation experiments, as they were expected to contain lightly oxidised (but still exfoliated) GONRs.

These fractions were dispersed in buffered H_2O and modified with CA using the EDC-catalysed reaction (details in methods). These were then mixed with 10 nm AuNps to maximise chances of bonding and viewed using TEM. Figure 5. 7 and Figure 5. 8 show these GNRs exhibiting a much higher degree of functionality than previous attempts, as AuNps can be seen binding selectively to both GONR stacks and to well-exfoliated GONRs, with preferential binding to edges. Figure 5. 8b shows a very thin GONR with AuNps decorated mostly around the edges, and only a relatively small number bound to the basal plane. The contrast in this image is too low to see the GONR alone, which suggests few to single-layer material. The contrast in, (a), however, is high enough to see the GONR material with AuNps decorating the edges in the same ordered patterns as (b). Closer analysis of the contrast levels in (a) suggests that this GONR stack has been partially eroded through the basal plane, making it similar to the type of GO flakes identified in Figure 5. 3. This is accompanied by an increase in the number of surface-bound AuNps, which would be bound to defects and ridges generated by the erosion through the sheets. Looking closely at the pattern of AuNps assembled in Figure 5. 8a/b (and assuming they are bound mostly at the edges), an overall direction and structure of the GONR can be observed, but the local edge roughness has increased significantly compared to the more pristine edges observed in the functionalised GNR stacks in Figure 5. 7c-f. However, these stacks are not as well-decorated as the more oxidised material, suggesting there is a relationship between oxidation extent and functionalisability, which was expected. This relationship is illustrated further in Figure 5. 8c, which shows both relatively pristine ribbon-like stacks of GNRs and fraying sections of very thin, oxidised

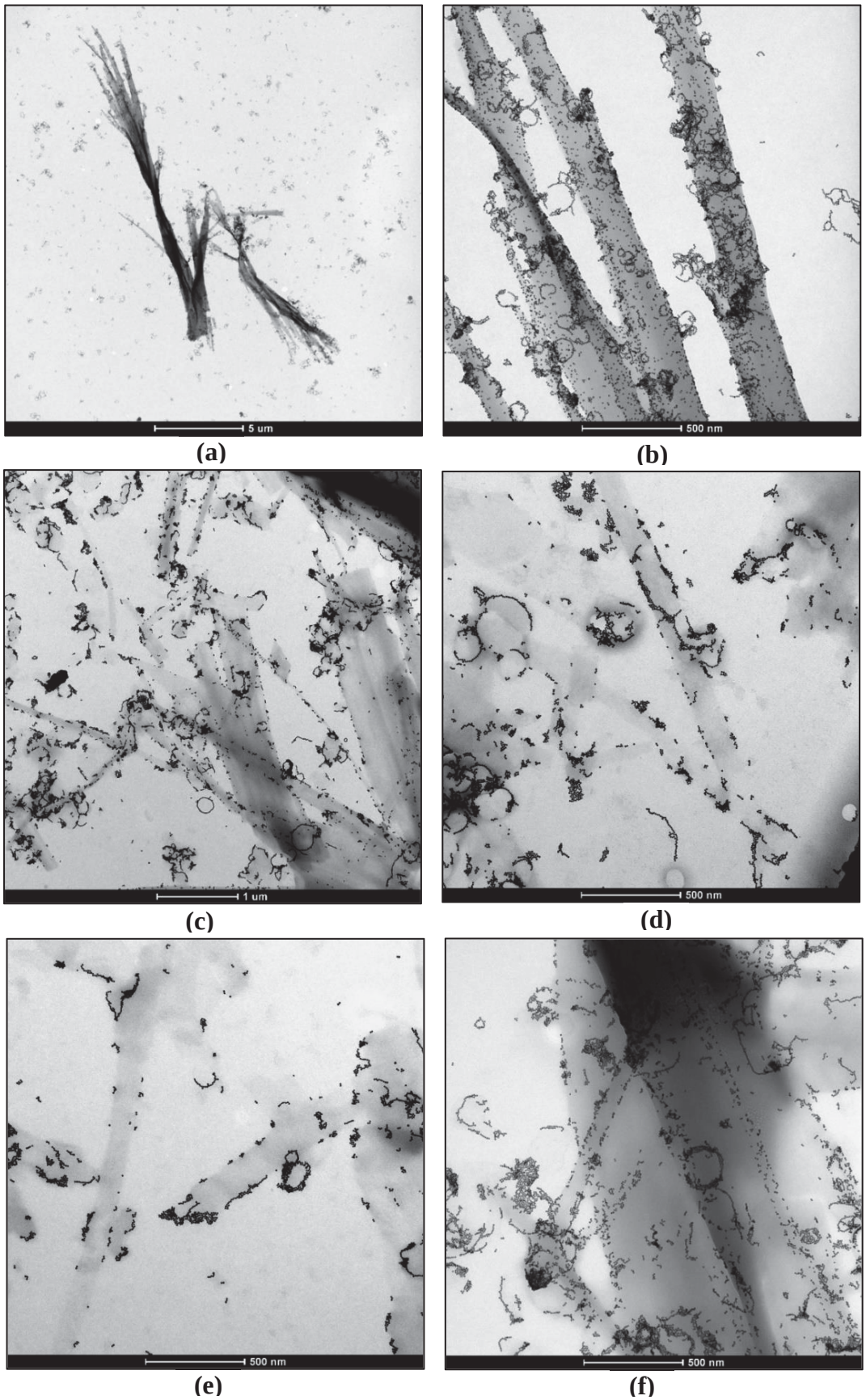

Figure 5. 7 - TEM images of AuNp functionalised GONR-CA. (a) Large stacks of GNRs/GNBs with AuNps decorated over its surfaces. (b) Zoom of (a). (c-f) Thin stacks of GNRs showing high edge-selectivity of bound AuNps

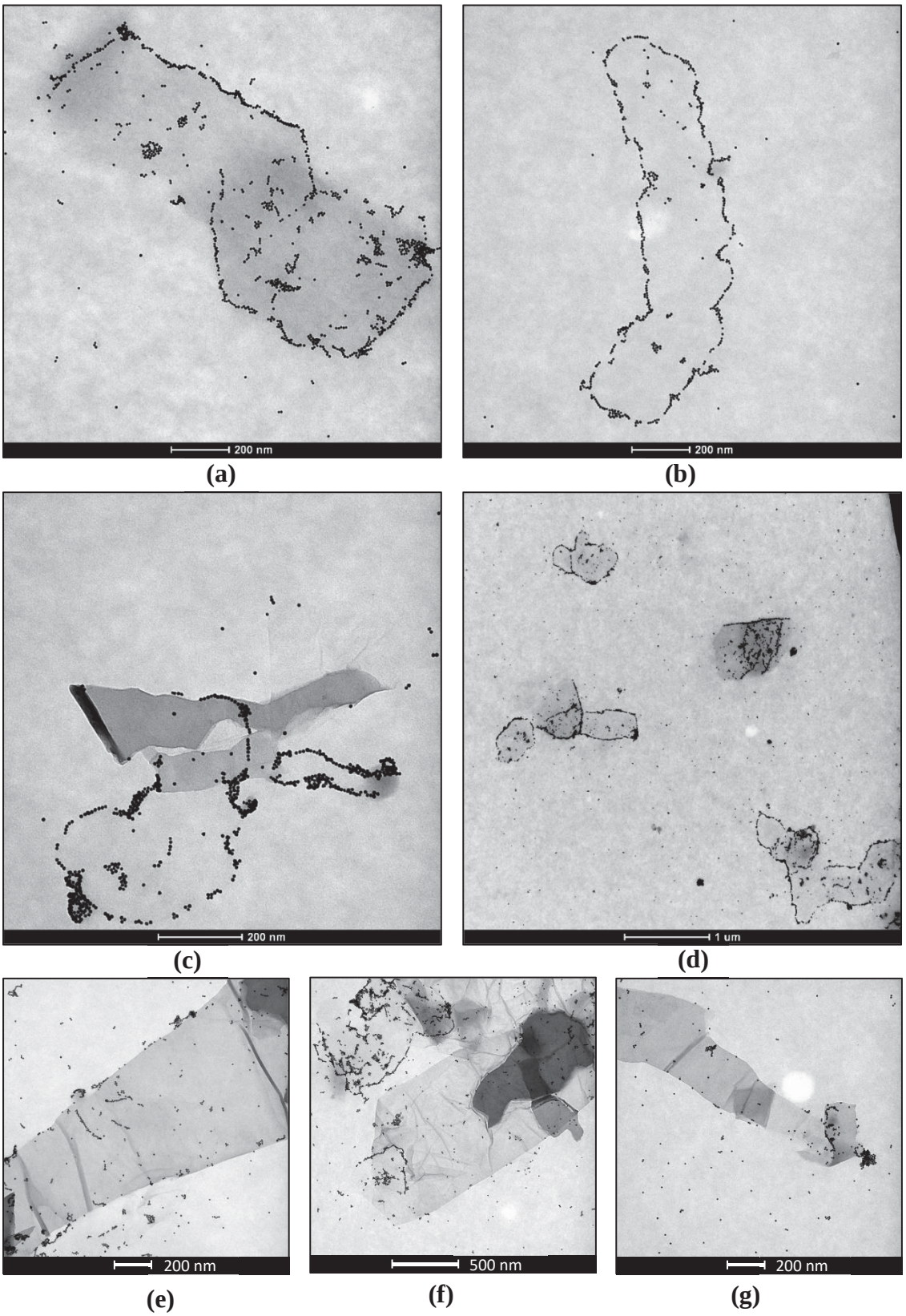

Figure 5. 8 - TEM of GNRs demonstrating oxidation-dependent functionalisation. (a) Few and (b) near-single layer GONRs with mostly edge specific functionalisation of AuNps, defining clear outlines. (c-d) Highly oxidised (rough edges, low contrast) graphene shows high-degrees of edge-specific functionalisation, while relatively pristine material shows little functionalisation. (e-g) Additional examples of pristine material exhibiting poor functionalisation.

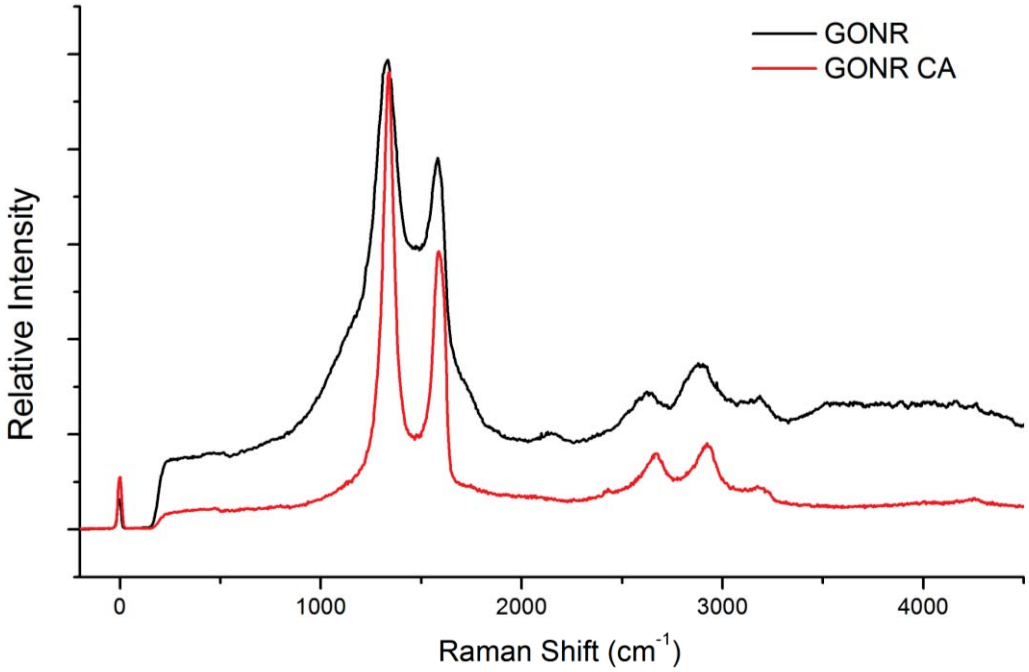

Figure 5. 9 - Raman spectra of GONR (black) and GONR-CA (red).

material. Figure 5. 8d-g shows GONRs and flakes outlined by the gold with high edge-selectivity, while pristine stacks have very little gold bound at all.

The Raman spectra of GONR and GONR-CA in Figure 5. 9 illustrates the increase in I_D:I_G ratio of oxidised material, and a further increase for GONR-CA. Though no new peaks are visible, the increase I_D:I_G ratio could be an indicator of increased edge-disorder due to functionalisation. From these results, I conclude that the oxidative processes enhances functionalisability, but does so at the cost of material quality.

Out of all the functionalised material generated by each chemical approach, this GONR method has produced the largest degree of functionalisation. It does so, however, at the expense of material quality. Less destructive chemistries have been successfully used to functionalise GNRs, but these are not as effective in general. This may be due to low densities of modifiable edge residues in as-cut material, or it may simply be a result of the extensive oxidation and edge-roughening processes which result in high densities of functionalisable residues on GONRs. Nevertheless, it has been shown that harsh oxidation is capable of generating high levels of edge-favoured functionalisation, and there is likely room for optimisation in this procedure to generate highly-functional edges while maintaining high material quality.

5.4 Filamentous Bacteriophage Functionalisation

Non-covalent functionalisation of GNRs provides an alternative route to tailoring the properties of graphene and generally maintains material quality. Non-covalent functionalisation includes the surfactant stabilisation of GNRs in solutions of water, as surfactant molecules such as CTAB and SC adsorb to the basal plane of graphene and confer increased solubility in aqueous media. In this work, filamentous bacteriophage has been used to non-covalently modify the basal plane of GNRs, which lays the groundwork for applications in both biological and non-biological fields.[144]

Filamentous bacteriophages are a class of virus which only infect *E. coli* in a non-destructive manner, allowing the bacteria to continue to function with only a small decrease in productivity.[145] F1 filamentous bacteriophages (phage) are cylindrical in shape, typically ~850 nm long and 6 nm wide, and resemble long flexible rods. The wild-type phage is negatively charged at physiological pH, due to a net negative charge of -3 on each major coat protein (pVIII, which covers the vast majority of the phage, see Figure 5. 10). GNRs have been dispersed using CTAB detergent molecules in water, which bind to the GNR surface via hydrophobic interactions using a long aliphatic chain, and contain a positively charged head group which interacts with the solvent. This facilitates solvation and stability by providing electrostatic repulsion between charged head groups on other GNRs. Hence, CTAB-stabilised GNRs contain a net positive charge. Electrostatic attraction occurs between the negatively charged phage and positively charged GNRs resulting in packing of the phage onto the GNR surface. Figure 5. 11 shows GNRs functionalised with phages in this way. Images (a/b) show GNRs interacting with an excess of phage, which are visible as the filamentous coils running across the surface. Images (c-e) show a purified sample of (a/b) in which the excess phage is removed. These images show a GNR with phages densely packed on the graphene surfaces, even coiling and bending to sit flush with the edges of the graphene basal plane. The increase in phage packing density in the purified sample compared with the impure sample is noteworthy. This shows that by removing excess phage, bound phage assumes a more ordered and tightly packed assembly, which suggests that there may be phage-phage interactions in solution, or phage-substrate interactions, which lower the association of phages with GNRs. It is clear from these images that the phages exhibit some inter-particle attractions, as illustrated by the grouping of phage bundles in (a) and (b).

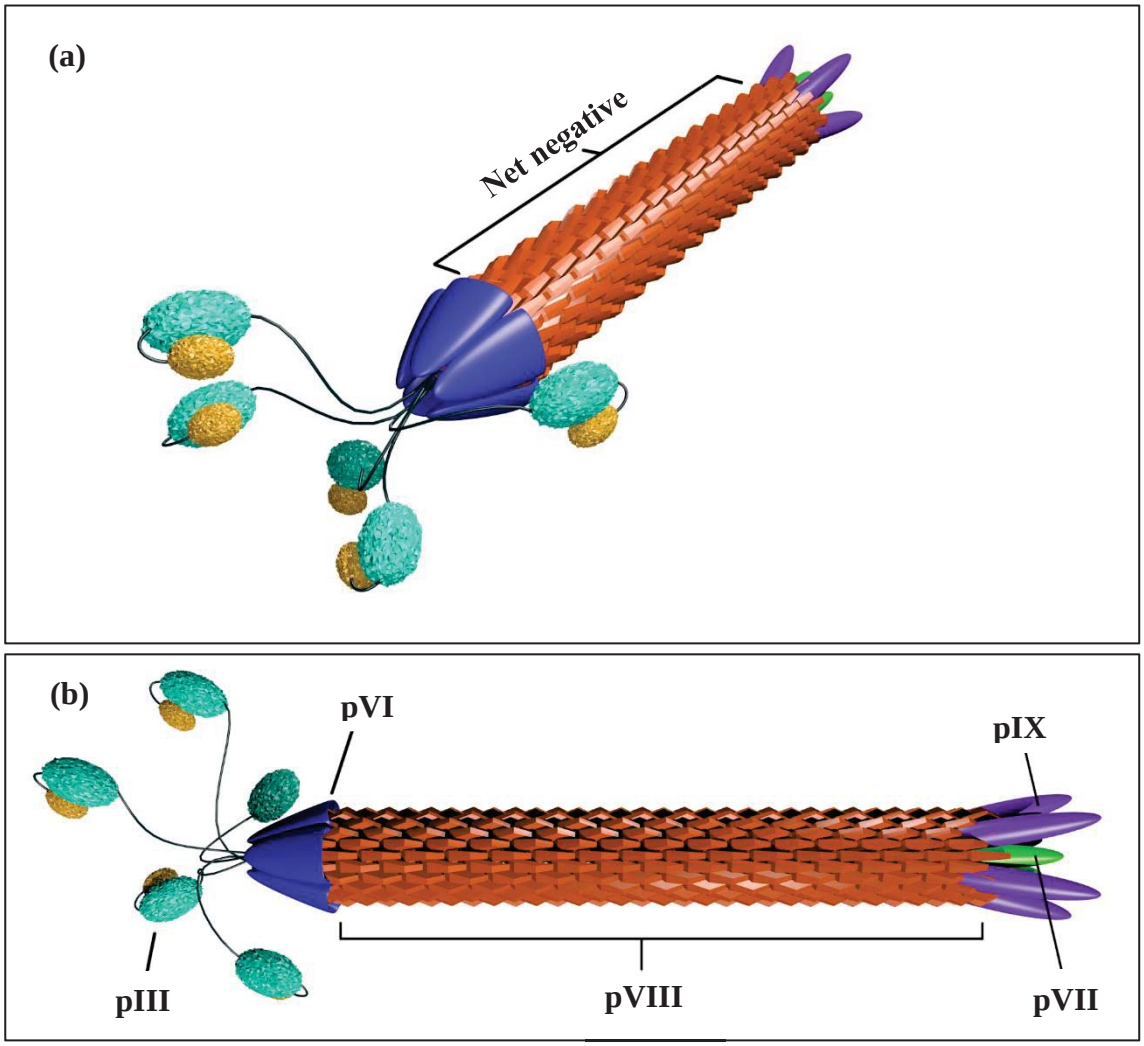

Figure 5. 10 - Schematic representations of filamentous bacteriophage. (a) Perspective view, showing the coat proteins which contribute the most to the net negative charge for f1 phage. (b) Top-down view illustrating coat proteins. In each phage particle, there are $3-5$ of pVII and pIX, 5 of pVI and pIII, and thousands of pVIII major coat proteins (their actual number depends on the size/length of genome being packaged within, but wild-type f1 phages are typically ~850 nm long and 6 nm in diameter, and contain ~2700 pVIII copies). The pVIII coat protein is a simple, rod-like alpha-helix, which overlays with its neighbours forming a fish scale-like coating around the core genome. (Image generated using Blender 3D modelling software. Creative Commons License, Sam Brooke).

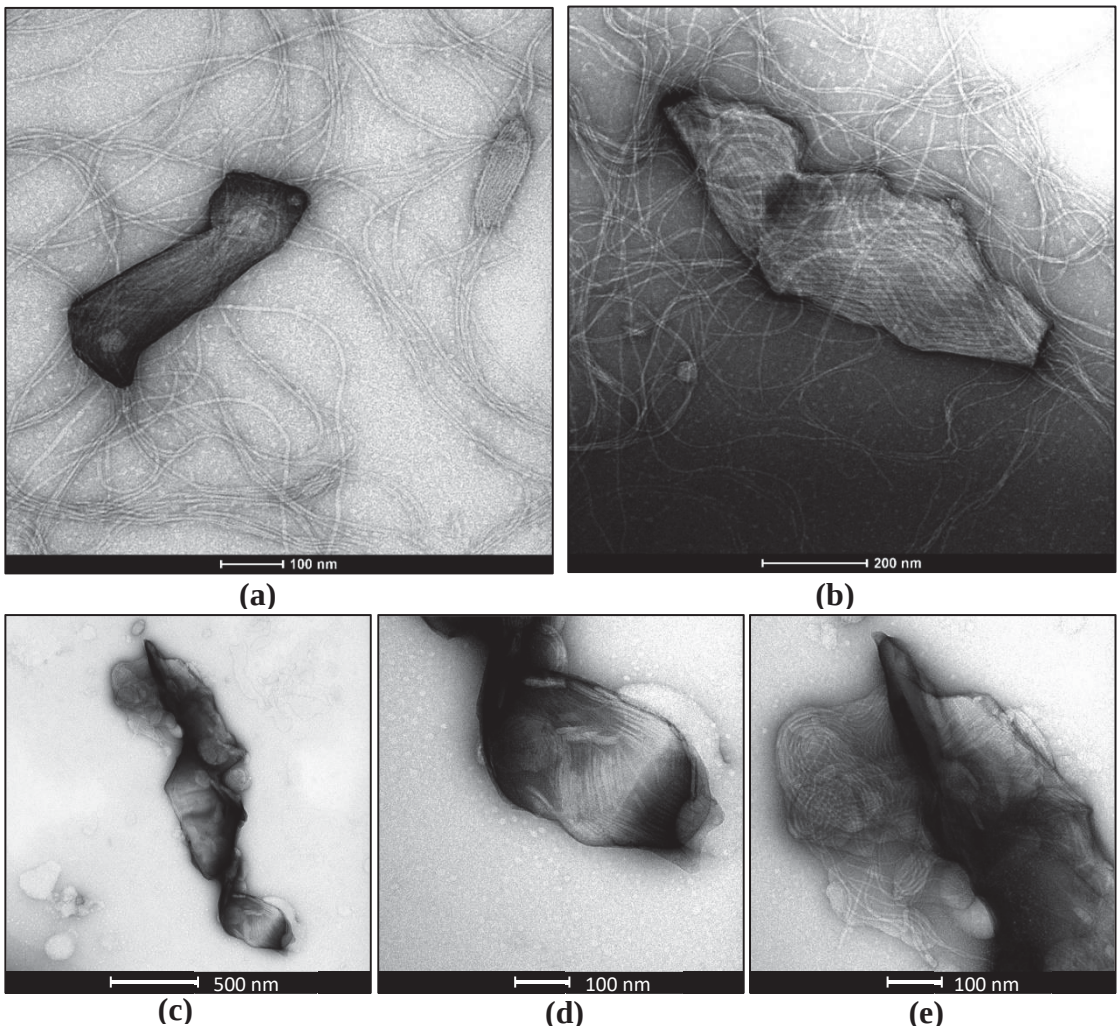

Figure 5. 11 - Filamentous bacteriophage-functionalised GNRs. (a/b) GNRs interacting with an excess of phages, which are seen spreading over the grid surface. (c) GNRs purified from (a/b), with phage now selectively bound to the surfaces. (d) Zooms of lower right and (e) upper left of (c).

This work has demonstrated the functionalisation of GNR materials via charge-based interactions, however, these results can be difficult to reproduce, and depend upon precise control of a number of variables, which suggests a more complex system of interactions may be controlling functionalisation. It has been noted that the buffer and pH of the solutions, and the detergent molecules used all play roles in achieving efficient functionalisation. As a biological material, f1 phages present a mixture of amino acids and charge groups to solution, which are affected by pH. Moreover, the aforementioned net negative charge on the major coat proteins does not mean the absence of positive charges (for example, lysine side chains are positively charged below pH 10.5, even though the overall phage is negatively charged above pH 4),[146] and the other (minor) coat proteins contain different amino acid sequences and isoelectric points altogether. While negative charges dominate the phage particle microscopically at physiological pH, positively charged residues will still be present at interfaces and will be capable of forming interactions, either with neighbouring residues, other phages, or the molecules in solution.

The role of detergent is complex, where high concentrations will cover more of the graphene surface and provide high charge densities, but may also interact with the phage particles and alter their net charges. It may also be that the highest detergent-densities on graphene are not ideal for phage binding, as excess detergent may sterically hinder phage binding, while gaps in the detergent coating may provide pockets in which phage can bind strongly. Conversely, a low concentration of detergent will limit its interaction with phage, but also lower the density on graphene surfaces, which results in lower solubility and less GNR-phage functionalisation. An ideal detergent should have a high affinity for graphene, whilst still retaining good water solubility. The methods demonstrated here used dialysis and centrifugation to isolate detergent-stabilised GNRs

from solutions of high detergent concentration, thus achieving high densities on GNRs without providing excess solvated detergent to interact with phages. These interactions will be in an equilibrium, however, which means over time the surface-bound detergent will desorb and move into solution.

Charged buffer molecules may also interact with phage and/or detergent-stabilised graphene, inhibiting GNR-phage functionalisation. Therefore, it is important to choose a buffer which will not affect the charges present. Here, HEPES is used as it is a zwitterionic buffer, meaning that from pH $3 - 7.5$ it will have both a positive and negative charge. It is used in relatively low concentrations, and if it does interact with either phage or detergent, the zwitterionic nature of the molecule means the overall charge is still maintained.

Full appreciation of the variables involved and their contributions to this system of interactions requires more research. Regardless, it has been shown that a relatively simple understanding can yield effective results. These phage-functionalised GNRs demonstrated high stability (several days) and easy dispersibility in water without damaging the highly-ordered GNR structures (unlike GONRs which are water-soluble but highly-oxidised). Literature has also demonstrated that basal plane functionalisation with phages does not impede the electronic or mechanical properties of graphene.[4] Water-soluble, high-quality graphene is highly sought after due its ease of manipulation for manufacturing processes,[106] and incorporating phage particles allows targeting of graphene with biological specificity for host of applications.[75-78] The tightly-packed assembly of phage on graphene demonstrated here is an ideal platform for the directed self-assembly of hybrid nanomaterials, and literature has demonstrated that such highly-ordered phages on graphene can be utilised in high-density energy storage applications.[4]

5.5 Summary

The functionalisation of GNRs has been investigated using organic synthetic techniques and non-covalent interactions. Due to the low edge-atom ratios of GNRs, the characterisation of edge modifications has proved challenging. Regardless, the functionalisation of pristine reduced and oxidised GNRs has been demonstrated using TEM and AuNp reporters, although the degree of reported functionalisation is much lower than anticipated. An adaptation of graphene oxide synthesis protocols has been employed and demonstrates a significant increase in AuNp functionalisation showing excellent edge-selectivity of chemical reactions. These results indicate that the initial densities of functional residues on the edges of dry-cut GNRs are relatively low, and I conclude that the chemical functionality of these GNR materials can be vastly improved via careful employment of harsh oxidation techniques. Further optimisation of the oxidative processes is expected to yield highly-functionalised edges while maintaining material quality. This approach represents a route to highly-functionalised graphene materials which can be specifically tailored to unique applications. Non-covalent functionalisation of GNR surfaces with filamentous bacteriophage has been demonstrated with high efficiency, encapsulating the surface of the GNR and laying foundations for further research into biofunctionalised GNRs and hybrid materials.

Chapter 6: Conclusion and Future Directions

This work demonstrates another step forward in the ever-advancing frontier of graphene research. Mechanical fracturing presents a unique solution to some of the pressing concerns in GNR synthesis, such as the balance between quality and quantity, and method scalability, which will need to be overcome for graphene to take a place at the core of future technologies. Mechanical fracturing provides a method to synthesise respectable quantities of high-quality graphene with controllable nanoscale dimensions and high edge-smoothness. It has been demonstrated herein that mechanical fracturing in air improves all these properties, for higher yields, better quality material and smoother edges. To my knowledge, this technique demonstrates the highest quality GNRs of any top-down synthetic approach reported in literature to date. Further, these adaptations enhance the scalability of the technique and present an opportunity for automation. The physical mechanisms of mechanical fracturing have been investigated and discussed with respect to literature, however, much of the details surrounding fracturing dynamics and edge-rearrangements remain unknown, and require further investigations. The fracturing methods have been optimised for efficient GNR synthesis, and the products generated have been characterised as bulk, multi-layer, and single-layer material, providing insights into the mechanical and structural properties of this high-aspect ratio nanomaterial. The GNRs generated by this technique are unique, in that most high-quality graphene is terminated by generally unreactive hydrogen atoms, while mechanical fracturing incorporates molecules from the surrounding environment, resulting in edge termination with functional handles that can be targeted for chemical modification.

It has been shown that these residues can be functionalised using simple organic chemistry techniques such as esterification and amidation reactions. The characterisation of these modifications has proven a challenge spectroscopically, but the use of AuNp

reporters for TEM and AFM has been successful in demonstrating edge-specific functionalisation of GNRs. The ability to specifically target easily functionalisable residues on the edges of GNR materials allows a broad range of chemistries to modify the material while preserving overall quality, opening these mechanically fractured GNRs to a wide range of applications.

Future directions for mechanical fracturing in air involve using controlled atmospheres to direct the functionalisation of as-cut material. Currently, amines dominate edge functionality, and we believe that cutting in oxygen or carbon dioxide rich atmospheres can produce a dominance of oxygenated edge species. Minor modifications to the microtomy setup such as a gas chamber or tent would be required to control the atmosphere in this way. Further steps in chemical modification of GNRs involves the optimisation of the harsh oxidation techniques to achieve high edge-functionality without significant damage to the basal plane, and the investigation of new chemistries to expand the range of functionality for this GNR material.

Appendix 1

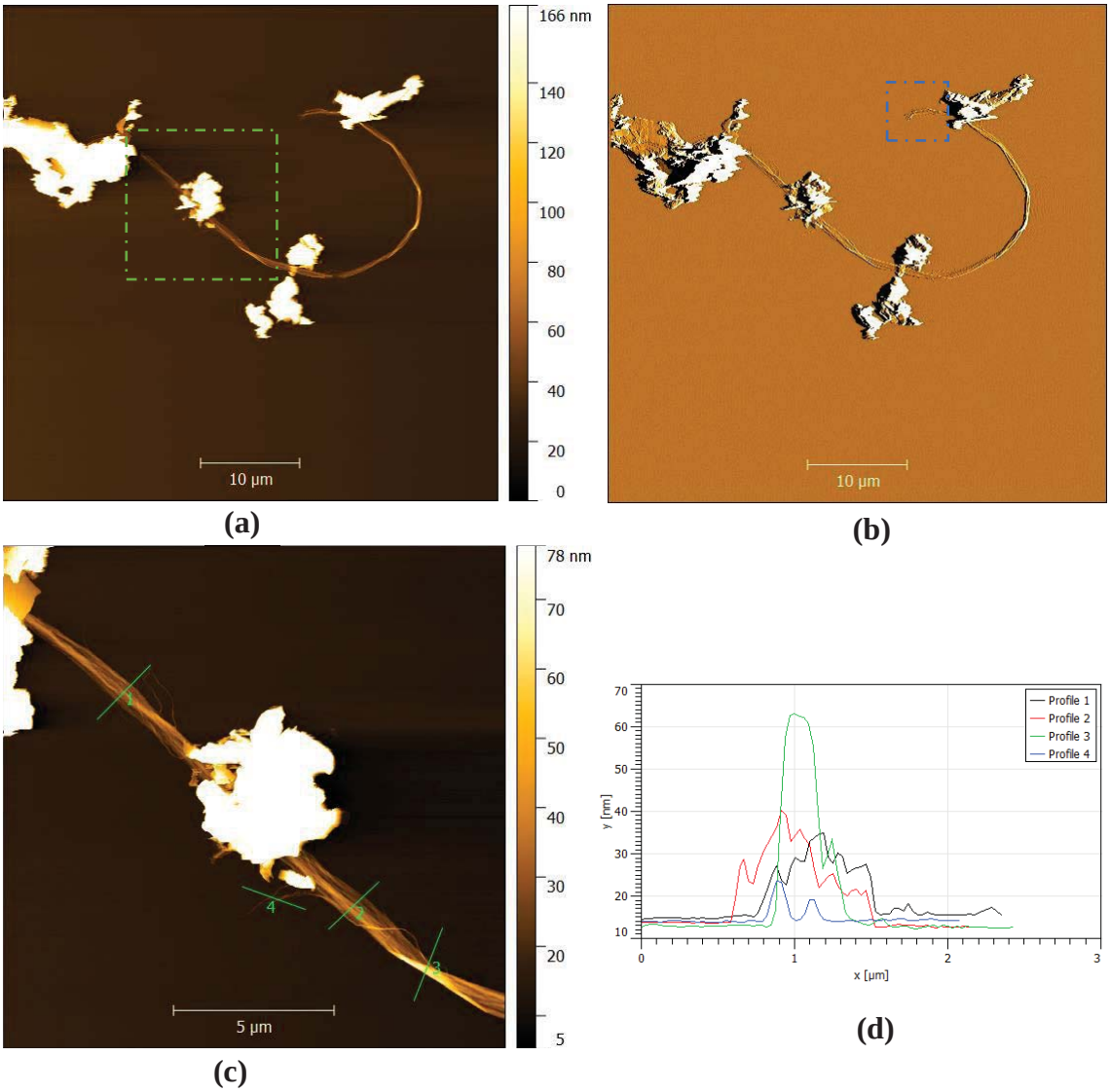

Figure A1. 1 - Additional AFM images of the GNB depicting full size and morphology. (a) Topography scan of whole GNB. (b) Amplitude scan of (a). Blue selection shows area of scan in Figure 4. 1a (inset). (c) Zoom of (a) in outlined area. (d) Profiles of corresponding marked cross-sections in (c).

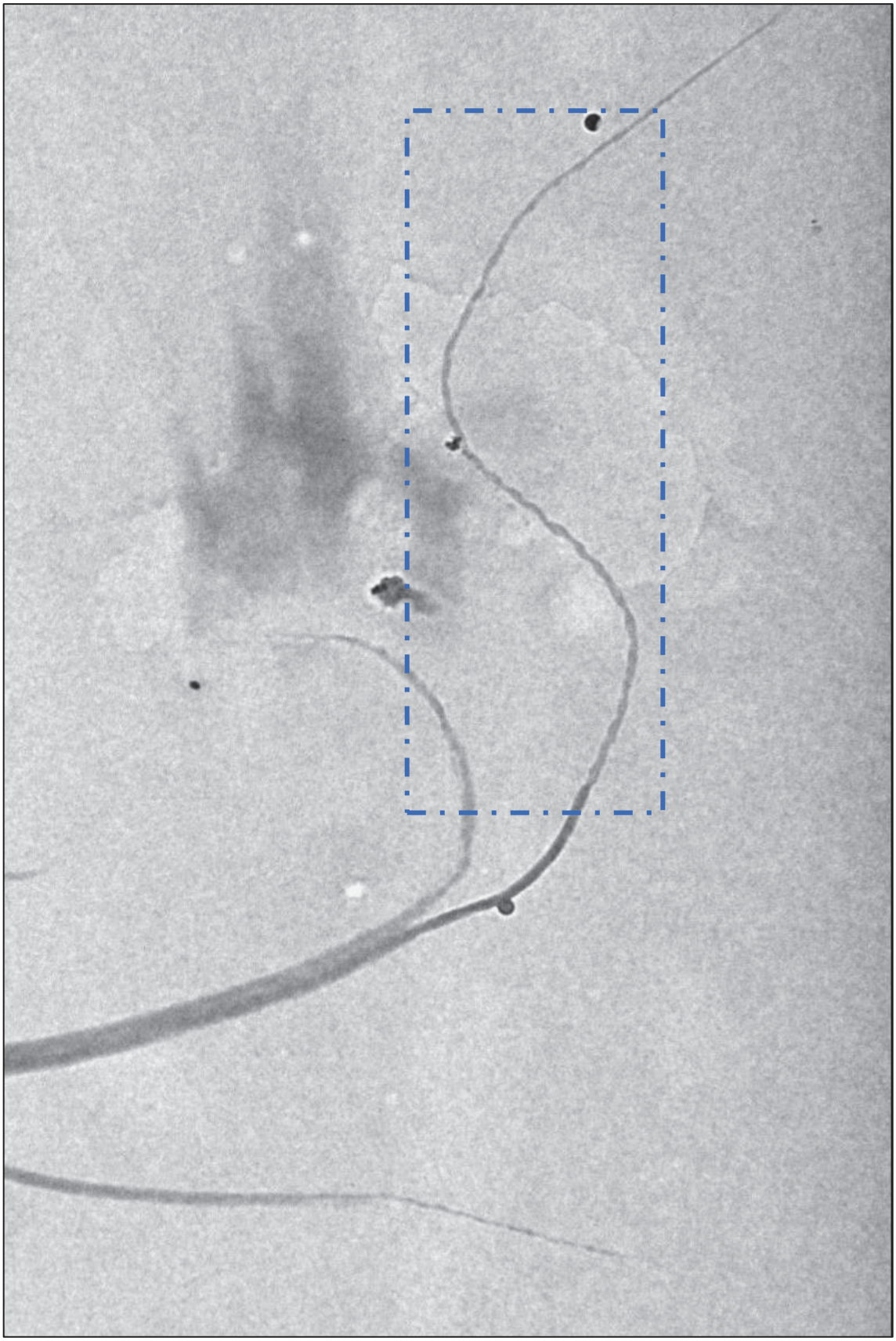

Figure A1. 2 - Zoom of TEM image showing coiling of tapering GNR stacks. Selection shows area where coiling seems to begin and end.

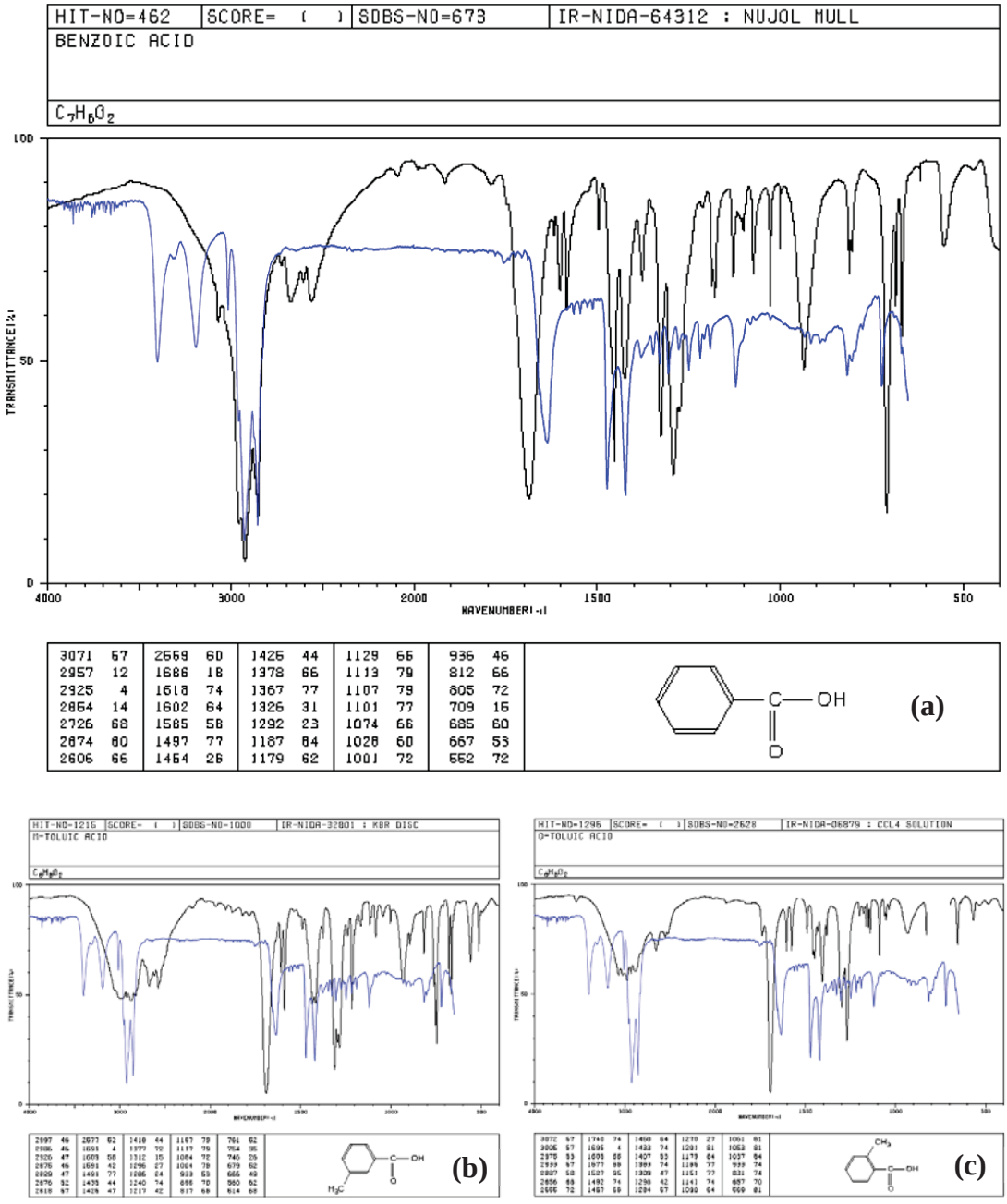

Figure A1. 3 - SDBS spectral comparisons between GNR samples and benzoic acid derivatives. (a) Benzoic acid comparison, (b) M-Toluic acid comparison, (c) *ortho*-Toluic acid comparison.

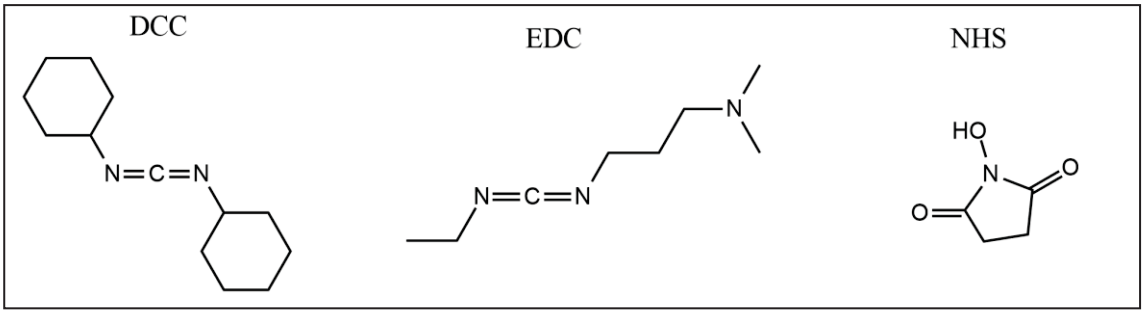

Figure A1. 4 - Structure of catalysts used in esterification and amidation reactions.

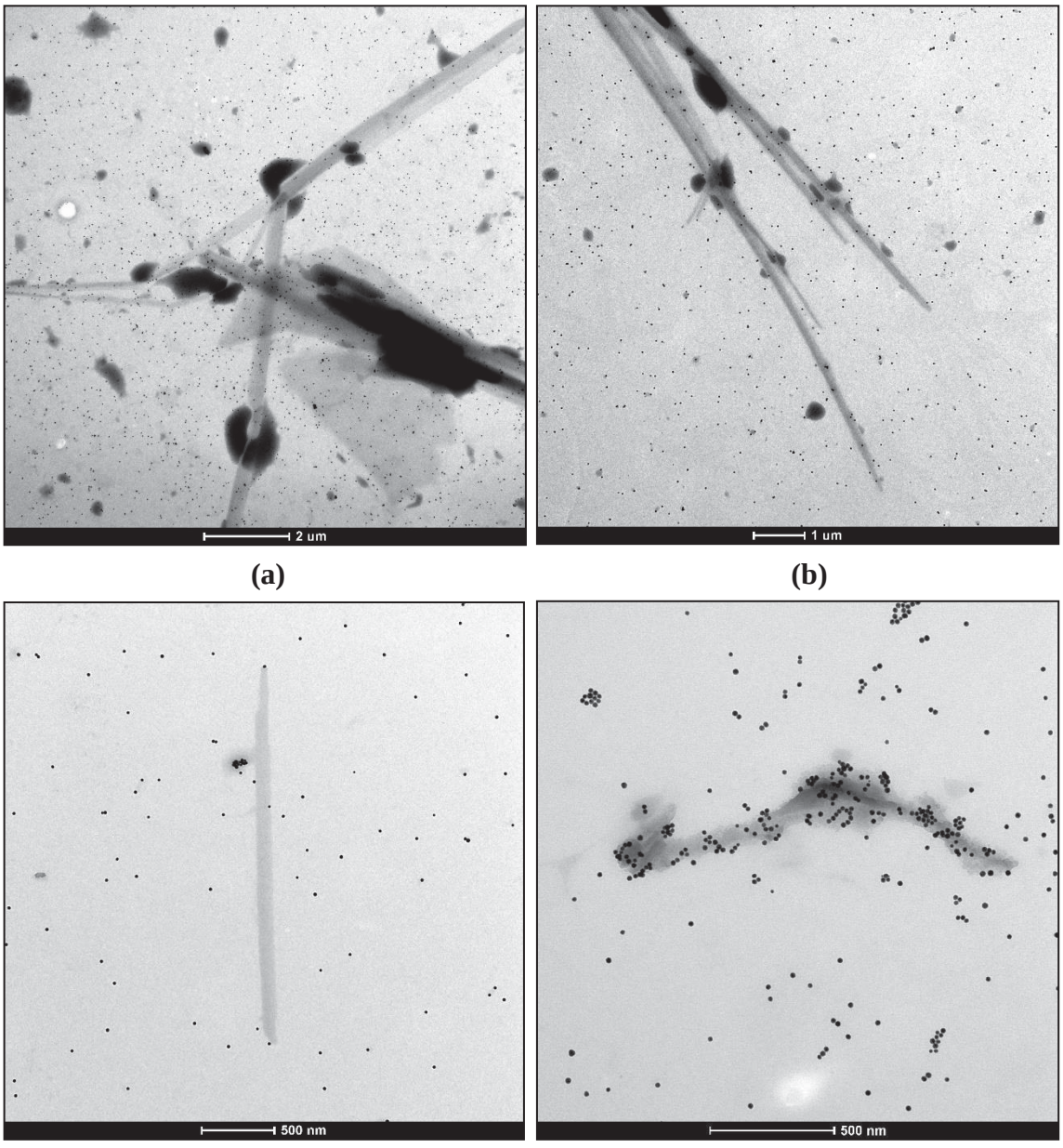

Figure A1. 5 - GONR-CA stacks and AuNps. (a-c) No specific binding of gold to GONRs. (d) AuNps bound to highly-oxidised GONR stack, as evidenced by the ridged layers and irregular edges.

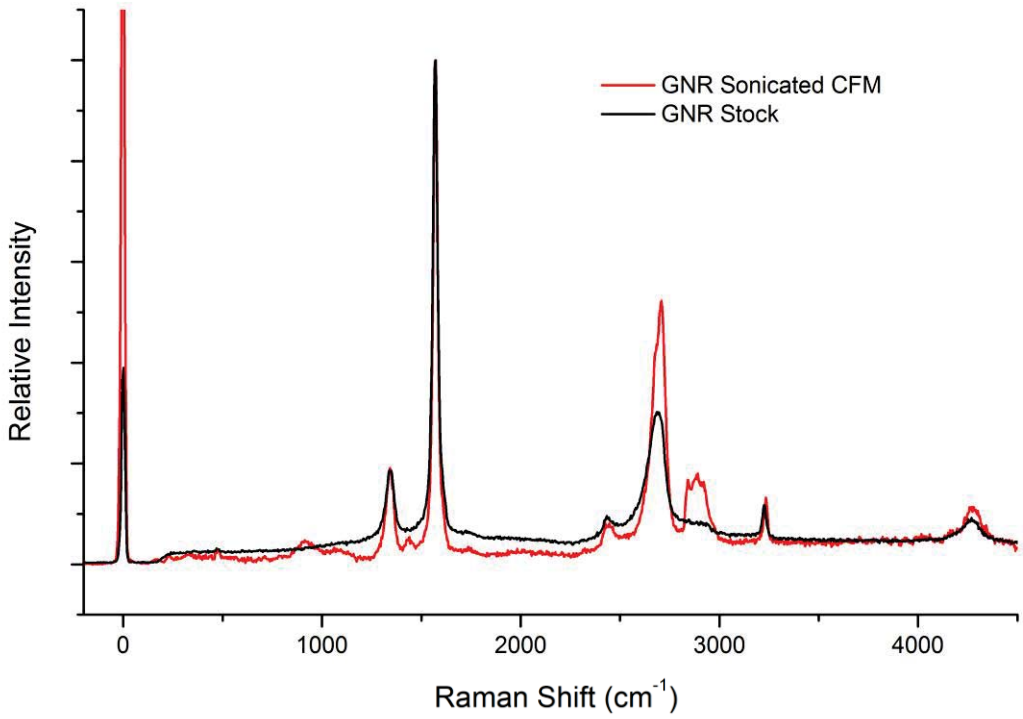

Figure A1. 6 – Raman spectra of stock GNR (black) and GNRs which have been sonicated in $CHCl_3$ for 72 hours at 50%. No significant changes are observed in the I_D:I_G ratios. The increased 2D peak ($\sim 2650\ cm^{-1}$) indicates a higher degree of exfoliation in the $CHCl_3$ sample.

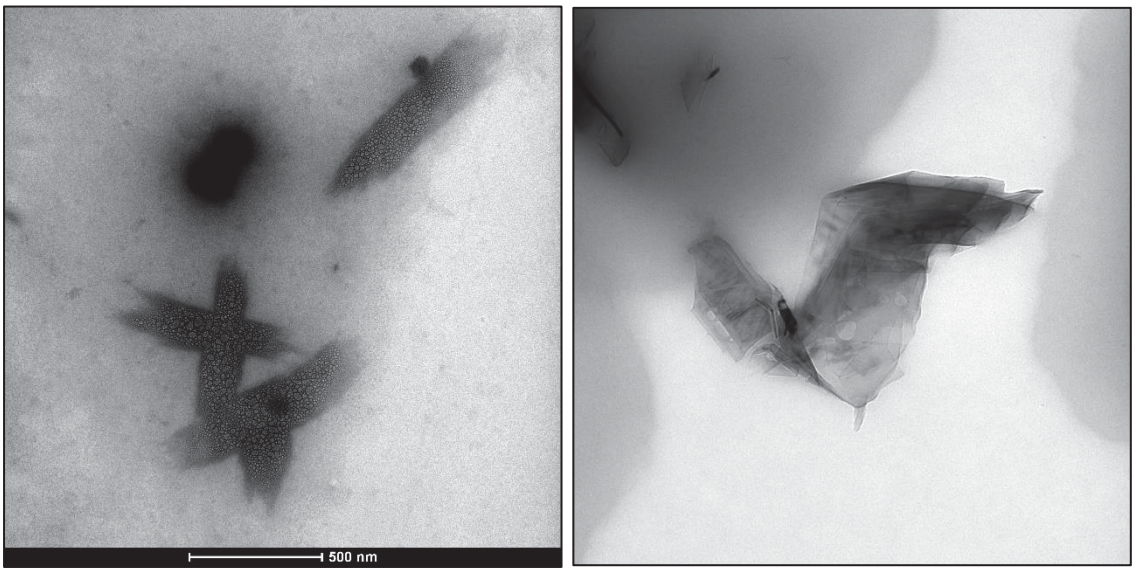

(a) **(b)**

Figure A1. 7 – TEM images showing solvent trapped between graphene layers forming bubbles of gas upon electron beam-excitation.

Appendix 2

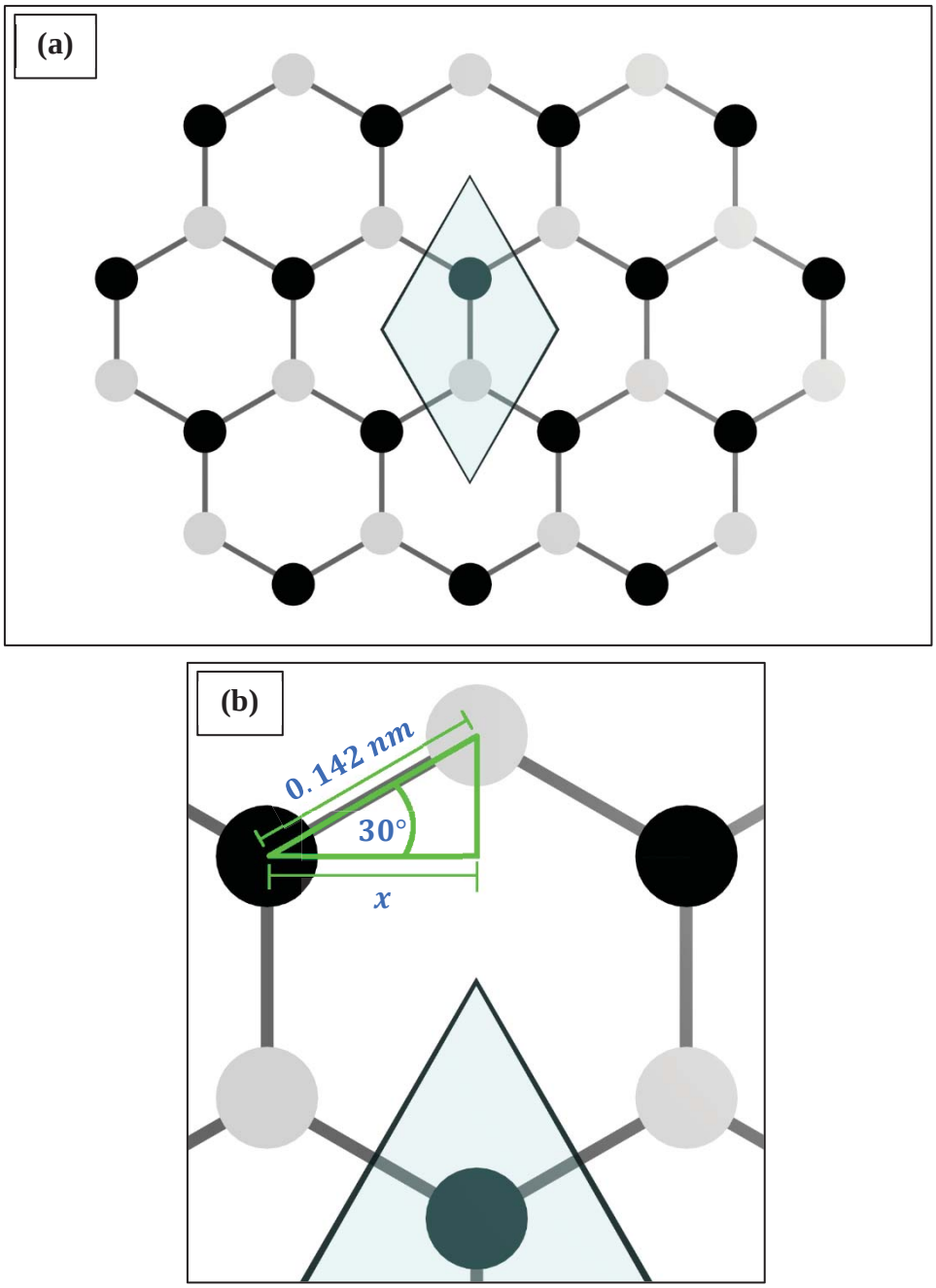

Figure A2. 1 - Schematic diagrams of (a) unit cell of graphene and (b) 6-membered ring showing angles and distances between atoms. Distance $2x$ is used as distance between zigzag edge atoms.

Edge atom calculations:

Unit cell area = 6.98498×10^{-20} m^2

Therefore, 2 carbons per 6.98498×10^{-20} m^2

GNR area (1:10 aspect ratio):

$$1\times10^{-7}\ \mathrm{m}\times1\times10^{-6}\ \mathrm{m}=1\times10^{-13}\ \mathrm{m}^2$$

Carbons per GNR:

$$\frac{1\times10^{-13}\ \mathrm{m}^2}{6.98498\times10^{-20}\ \mathrm{m}^2}\times2\ \text{carbons}=2863286.652\ \text{carbons GNR}^{-1}$$

Distance between zigzag edge atoms:

$$x=0.142\cos(30)=0.12298\ \mathrm{nm}$$

Therefore, distance between edge atoms:

$$0.12298\ \mathrm{nm}\times2=0.24595\ \mathrm{nm}$$

$$\frac{2.2\times10^{-6}\ \mathrm{m}}{0.24595\times10^{-9}\ \mathrm{m}}=8944.91$$

Therefore, ~8945 atoms on the edge (assuming perfect exclusively zigzag edges).

$$\frac{8944.91}{2863286.652}=3.124^{-3}\ \text{edge atoms per basal plane atom}$$

$$3.124^{-3}\times100\%=0.3124\%\ \text{edges on GNRs}$$

or

$$\frac{1}{3.124^{-3}}=\sim1:320\ \text{edge to basal plane atoms.}$$

Concentration of edge residues:

Mass of GNR:

$$\frac{2.863287\times10^{6}}{6.022\times10^{23}}=4.7547\times10^{-18}\ \mathrm{mol}$$

$$4.7547\times10^{-18}\ \mathrm{mol}\times12.01\ \mathrm{g\ mol^{-1}}=5.71\times10^{-17}\ \mathrm{g}$$

Therefore, 1 mg of GNRs gives:

$$\frac{1\times10^{-3}\ \mathrm{g}}{5.71\times10^{-17}\ \mathrm{g}}=1.7512\times10^{13}\ \mathrm{GNR\ mg^{-1}}$$

Max edge residues per GNR $=\sim8944$ (based on total functionalisation of every zigzag edge. Edges per mg:

$$1.7512\times10^{13} \times 8944.91 = 1.5664\times10^{17}$$

Moles of edges per mg: $\frac{1.5664\times10^{17}}{6.022\times10^{23}} = 2.6011\times10^{-7}$ mol

$$= 0.26\ \mu\text{mol}$$

Masses of reactants:

DCC: 206.33 g mol^{-1}

CA: 77.15 g mol^{-1}

$$206.33\ \text{g mol}^{-1} \times 2.601\times10^{-7}\ \text{mol} = 5.3668\times10^{-5}\ \text{g}$$

$$= 53.7\ \mu\text{g}$$

$$77.15\ \text{g mol}^{-1} \times 2.601\times10^{-7}\ \text{mol} = 2.0067\times10^{-5}\ \text{g}$$

$$= 20.1\ \mu\text{g}$$

Bibliography

1. Huang, Y.; Dong, X.; Liu, Y.; Li, L.-J.; Chen, P., Graphene-based biosensors for detection of bacteria and their metabolic activities. *J. Mater. Chem.* 2011**,** *21* (33), 12358-12362.

2. Novoselov, K. S.; Jiang, Z.; Zhang, Y.; Morozov, S. V.; Stormer, H. L.; Zeitler, U.; Maan, J. C.; Boebinger, G. S.; Kim, P.; Geim, A. K., Room-temperature quantum hall effect in graphene. *Science* 2007**,** *315* (5817), 1379-1379.

3. Katsnelson, M. I.; Novoselov, K. S.; Geim, A. K., Chiral tunnelling and the Klein paradox in graphene. *Nat. Phys.* 2006**,** *2* (9), 620-625.

4. Oh, D. Y.; Dang, X. N.; Yi, H. J.; Allen, M. A.; Xu, K.; Lee, Y. J.; Belcher, A. M., Graphene Sheets Stabilized on Genetically Engineered M13 Viral Templates as Conducting Frameworks for Hybrid Energy-Storage Materials. *Small* 2012**,** *8* (7), 1006-1011.

5. Cui, Y.; Kim, S. N.; Naik, R. R.; McAlpine, M. C., Biomimetic Peptide Nanosensors. *Acc. Chem. Res.* 2012**,** *45* (5), 696-704.

6. Kim, S. N.; Kuang, Z.; Slocik, J. M.; Jones, S. E.; Cui, Y.; Farmer, B. L.; McAlpine, M. C.; Naik, R. R., Preferential Binding of Peptides to Graphene Edges and Planes. *J. Am. Chem. Soc.* 2011**,** *133* (37), 14480-14483.

7. Kang, X.; Wang, J.; Wu, H.; Aksay, I. A.; Liu, J.; Lin, Y., Glucose Oxidase-graphene-chitosan modified electrode for direct electrochemistry and glucose sensing. *Biosens. Bioelectron.* 2009**,** *25* (4), 901-905.

8. Shan, C.; Yang, H.; Song, J.; Han, D.; Ivaska, A.; Niu, L., Direct Electrochemistry of Glucose Oxidase and Biosensing for Glucose Based on Graphene. *Anal. Chem.* 2009**,** *81* (6), 2378-2382.

9. Lin, Y. H.; Lu, F.; Tu, Y.; Ren, Z. F., Glucose biosensors based on carbon nanotube nanoelectrode ensembles. *Nano Lett.* 2004**,** *4* (2), 191-195.

10. Shao, Y.; Wang, J.; Wu, H.; Liu, J.; Aksay, I. A.; Lin, Y., Graphene Based Electrochemical Sensors and Biosensors: A Review. *Electroanalysis* 2010**,** *22* (10), 1027-1036.

11. Mao, S.; Lu, G.; Yu, K.; Bo, Z.; Chen, J., Specific Protein Detection Using Thermally Reduced Graphene Oxide Sheet Decorated with Gold Nanoparticle-Antibody Conjugates. *Adv. Mater.* 2010**,** *22* (32), 3521.

12. Kosynkin, D. V.; Higginbotham, A. L.; Sinitskii, A.; Lomeda, J. R.; Dimiev, A.; Price, B. K.; Tour, J. M., Longitudinal unzipping of carbon nanotubes to form graphene nanoribbons. *Nature* 2009**,** *458* (7240), 872.

13. Li, X. L.; Wang, X. R.; Zhang, L.; Lee, S. W.; Dai, H. J., Chemically derived, ultrasmooth graphene nanoribbon semiconductors. *Science* 2008**,** *319* (5867), 1229-1232.

14. Wei, D. C.; Liu, Y. Q.; Zhang, H. L.; Huang, L. P.; Wu, B.; Chen, J. Y.; Yu, G., Scalable Synthesis of Few-Layer Graphene Ribbons with Controlled Morphologies by a Template Method and Their Applications in Nanoelectromechanical Switches. *J. Am. Chem. Soc.* 2009**,** *131* (31), 11147-11154.

15. Cai, J. M.; Ruffieux, P.; Jaafar, R.; Bieri, M.; Braun, T.; Blankenburg, S.; Muoth, M.; Seitsonen, A. P.; Saleh, M.; Feng, X. L.; Mullen, K.; Fasel, R., Atomically precise bottom-up fabrication of graphene nanoribbons. *Nature* 2010**,** *466* (7305), 470-473.

16. Castro Neto, A. H.; Guinea, F.; Peres, N. M. R.; Novoselov, K. S.; Geim, A. K., The electronic properties of graphene. *Rev. Mod. Phys.* 2009**,** *81* (1), 109-162.

17. Novoselov, K. S.; Fal'ko, V. I.; Colombo, L.; Gellert, P. R.; Schwab, M. G.; Kim, K., A roadmap for graphene. *Nature* 2012**,** *490* (7419), 192-200.

18. Parvez, K.; Wu, Z.-S.; Li, R.; Liu, X.; Graf, R.; Feng, X.; Muellen, K., Exfoliation of Graphite into Graphene in Aqueous Solutions of Inorganic Salts. *J. Am. Chem. Soc.* 2014**,** *136* (16), 6083-6091.

19. Zhou, M.; Tang, J.; Cheng, Q.; Xu, G.; Cui, P.; Qin, L.-C., Few-layer graphene obtained by electrochemical exfoliation of graphite cathode. *Chem. Phys. Lett.* 2013**,** *572*, 61-65.

20. Jacobberger, R. M.; Kiraly, B.; Fortin-Deschenes, M.; Levesque, P. L.; McElhinny, K. M.; Brady, G. J.; Delgado, R. R.; Roy, S. S.; Mannix, A.; Lagally, M. G.; Evans, P. G.; Desjardins, P.; Martel, R.; Hersam, M. C.; Guisinger, N. P.; Arnold, M. S., Direct oriented growth of armchair graphene nanoribbons on germanium. *Nat. Commun.* 2015**,** *6*, 8.

21. Saghafi, M.; Mahboubi, F.; Mohajerzadeh, S.; Fathi, M.; Holze, R., Longitudinal unzipping of carbon nanotubes and their electrochemical performance in supercapacitors. *Curr. Appl. Phys.* 2014**,** *14* (10), 1335-1343.

22. Ilango, P. R.; Prasanna, K.; Subburaj, T.; Jo, Y. N.; Lee, C. W., Facile longitudinal unzipping of carbon nanotubes to graphene nanoribbons and their effects on LiMn2O4 cathodes in rechargeable lithium-ion batteries. *Acta Materialia* 2015**,** *100*, 11-18.

23. Wallace, P. R., The Band Theory of Graphite. *Phys. Rev.* 1947**,** *71* (7), 476-476.

24. Novoselov, K. S.; Geim, A. K.; Morozov, S. V.; Jiang, D.; Zhang, Y.; Dubonos, S. V.; Grigorieva, I. V.; Firsov, A. A., Electric field effect in atomically thin carbon films. *Science* 2004**,** *306* (5696), 666-669.

25. Boehm, H. P.; Clauss, A.; Fischer, G. O.; Hofmann, U., Das Adsorptionsverhalten sehr dünner Kohlenstoff-Folien. *Z. Anorg. Allg. Chem.* 1962**,** *316* (3-4), 119-127.

26. SleepMaker, Graphene Infused Memory Foam. http://www.sleepmaker.com.au/why-sleepmaker/technologies/graphene-infused-memory-foam (accessed 11/1/2017).

27. Head, GRAPHENE-XT. http://www.head.com/en/sports/tennis/technology/graphene-xt/ (accessed 11/1/2017).

28. He, Z. L.; Que, W. X., Molybdenum disulfide nanomaterials: Structures, properties, synthesis and recent progress on hydrogen evolution reaction. *Appl. Mater. Today* 2016**,** *3*, 23-56.

29. Zhao, J. J.; Liu, H. S.; Yu, Z. M.; Quhe, R. G.; Zhou, S.; Wang, Y. Y.; Liu, C. C.; Zhong, H. X.; Han, N. N.; Lu, J.; Yao, Y. G.; Wu, K. H., Rise of silicene: A competitive 2D material. *Prog. Mater. Sci.* 2016**,** *83*, 24-151.

30. Bonaccorso, F.; Colombo, L.; Yu, G. H.; Stoller, M.; Tozzini, V.; Ferrari, A. C.; Ruoff, R. S.; Pellegrini, V., Graphene, related two-dimensional crystals, and hybrid systems for energy conversion and storage. *Science* 2015**,** *347* (6217), 10.

31. Meyer, J. C.; Geim, A. K.; Katsnelson, M. I.; Novoselov, K. S.; Booth, T. J.; Roth, S., The structure of suspended graphene sheets. *Nature* 2007**,** *446* (7131), 60-63.

32. L. D. Landau, E. M. L., *Statistical Physics Part 1*. Third Edition, Revised and Enlarged ed.; Robert Maxwell, M.C.: 1980; Vol. 5.

33. Ishigami, M.; Chen, J. H.; Cullen, W. G.; Fuhrer, M. S.; Williams, E. D., Atomic structure of graphene on SiO2. *Nano Lett.* 2007**,** *7* (6), 1643-1648.

34. Lee, C.; Wei, X. D.; Kysar, J. W.; Hone, J., Measurement of the elastic properties and intrinsic strength of monolayer graphene. *Science* 2008**,** *321* (5887), 385-388.

35. Nobel Media AB 2014. The Nobel Prize in Physics 2010 - Advanced Information. http://www.nobelprize.org/nobel_prizes/physics/laureates/2010/advanced.html.

36. Zhang, P.; Ma, L. L.; Fan, F. F.; Zeng, Z.; Peng, C.; Loya, P. E.; Liu, Z.; Gong, Y. J.; Zhang, J. N.; Zhang, X. X.; Ajayan, P. M.; Zhu, T.; Lou, J., Fracture toughness of graphene. *Nat. Commun.* 2014**,** *5*, 7.

37. Lee, J. H.; Loya, P. E.; Lou, J.; Thomas, E. L., Dynamic mechanical behavior of multilayer graphene via supersonic projectile penetration. *Science* 2014**,** *346* (6213), 1092-1096.

38. Cooper, D. R.; D'Anjou, B.; Ghattamaneni, N.; Harack, B.; Hilke, M.; Horth, A.; Majlis, N.; Massicotte, M.; Vandsburger, L.; Whiteway, E.; Yu, V., Experimental Review of Graphene. *ISRN Condens. Matter Phys.* 2012**,** *2012*, 56.

39. Novoselov, K. S.; Geim, A. K.; Morozov, S. V.; Jiang, D.; Katsnelson, M. I.; Grigorieva, I. V.; Dubonos, S. V.; Firsov, A. A., Two-dimensional gas of massless Dirac fermions in graphene. *Nature* 2005**,** *438* (7065), 197-200.

40. Geim, A. K., Graphene: Status and Prospects. *Science* 2009**,** *324* (5934), 1530-1534.

41. Bolotin, K. I.; Sikes, K. J.; Jiang, Z.; Klima, M.; Fudenberg, G.; Hone, J.; Kim, P.; Stormer, H. L., Ultrahigh electron mobility in suspended graphene. *Solid State Commun.* 2008**,** *146* (9-10), 351-355.

42. Chen, J. H.; Jang, C.; Xiao, S. D.; Ishigami, M.; Fuhrer, M. S., Intrinsic and extrinsic performance limits of graphene devices on SiO2. *Nat. Nanotechnol.* 2008**,** *3* (4), 206-209.

43. Castro, E. V.; Novoselov, K. S.; Morozov, S. V.; Peres, N. M. R.; Dos Santos, J.; Nilsson, J.; Guinea, F.; Geim, A. K.; Castro Neto, A. H., Biased bilayer graphene: Semiconductor with a gap tunable by the electric field effect. *Phys. Rev. Lett.* 2007**,** *99* (21), 4.

44. Ohta, T.; Bostwick, A.; Seyller, T.; Horn, K.; Rotenberg, E., Controlling the electronic structure of bilayer graphene. *Science* 2006**,** *313* (5789), 951-954.

45. Pereira, V. M.; Castro Neto, A. H.; Peres, N. M. R., Tight-binding approach to uniaxial strain in graphene. *Phys. Rev. B* 2009**,** *80* (4), 8.

46. Ni, Z. H.; Yu, T.; Lu, Y. H.; Wang, Y. Y.; Feng, Y. P.; Shen, Z. X., Uniaxial Strain on Graphene: Raman Spectroscopy Study and Band-Gap Opening. *Acs Nano* 2008**,** *2* (11), 2301-2305.

47. Rani, P.; Jindal, V. K., Designing band gap of graphene by B and N dopant atoms. *RSC Adv.* 2013**,** *3* (3), 802-812.

48. Zhang, S. J.; Lin, S. S.; Li, X. Q.; Liu, X. Y.; Wu, H. A.; Xu, W. L.; Wang, P.; Wu, Z. Q.; Zhong, H. K.; Xu, Z. J., Opening the band gap of graphene through silicon doping for the improved performance of graphene/GaAs heterojunction solar cells. *Nanoscale* 2016**,** *8* (1), 226-232.

49. Sharma, P.; Bernard, L. S.; Bazigos, A.; Magrez, A.; Ionescu, A. M., Graphene Negative Differential Resistance Circuit With Voltage-Tunable High Performance at Room Temperature. *IEEE Electron Device Lett.* 2015**,** *36* (8), 865-867.

50. Liu, G. X.; Ahsan, S.; Khitun, A. G.; Lake, R. K.; Balandin, A. A., Graphene-based non-Boolean logic circuits. *J. Appl. Phys.* 2013**,** *114* (15), 10.

51. Seol, J. H.; Jo, I.; Moore, A. L.; Lindsay, L.; Aitken, Z. H.; Pettes, M. T.; Li, X. S.; Yao, Z.; Huang, R.; Broido, D.; Mingo, N.; Ruoff, R. S.; Shi, L., Two-Dimensional Phonon Transport in Supported Graphene. *Science* 2010**,** *328* (5975), 213-216.

52. Balandin, A. A., Thermal properties of graphene and nanostructured carbon materials. *Nat. Mater.* 2011**,** *10* (8), 569-581.

53. Xu, X. F.; Pereira, L. F. C.; Wang, Y.; Wu, J.; Zhang, K. W.; Zhao, X. M.; Bae, S.; Bui, C. T.; Xie, R. G.; Thong, J. T. L.; Hong, B. H.; Loh, K. P.; Donadio, D.; Li, B. W.; Ozyilmaz, B., Length-dependent thermal conductivity in suspended single-layer graphene. *Nat. Commun.* 2014**,** *5*, 6.

54. Ju, Y. S.; Goodson, K. E., Phonon scattering in silicon films with thickness of order 100 nm. *Appl. Phys. Lett.* 1999**,** *74* (20), 3005-3007.

55. Park, J.; Yan, M. D., Covalent Functionalization of Graphene with Reactive Intermediates. *Acc. Chem. Res.* 2013**,** *46* (1), 181-189.

56. Liu, H. T.; Ryu, S. M.; Chen, Z. Y.; Steigerwald, M. L.; Nuckolls, C.; Brus, L. E., Photochemical Reactivity of Graphene. *J. Am. Chem. Soc.* 2009**,** *131* (47), 17099.

57. Fang, M.; Wang, K. G.; Lu, H. B.; Yang, Y. L.; Nutt, S., Single-layer graphene nanosheets with controlled grafting of polymer chains. *J. Mater. Chem.* 2010**,** *20* (10), 1982-1992.

58. Lin, Y. C.; Lin, C. Y.; Chiu, P. W., Controllable graphene N-doping with ammonia plasma. *Appl. Phys. Lett.* 2010**,** *96* (13), 3.

59. Sinitskii, A.; Dimiev, A.; Corley, D. A.; Fursina, A. A.; Kosynkin, D. V.; Tour, J. M., Kinetics of Diazonium Functionalization of Chemically Converted Graphene Nanoribbons. *Acs Nano* 2010**,** *4* (4), 1949-1954.

60. Niyogi, S.; Bekyarova, E.; Itkis, M. E.; Zhang, H.; Shepperd, K.; Hicks, J.; Sprinkle, M.; Berger, C.; Lau, C. N.; Deheer, W. A.; Conrad, E. H.; Haddon, R. C., Spectroscopy of Covalently Functionalized Graphene. *Nano Lett.* 2010**,** *10* (10), 4061-4066.

61. Choi, J.; Kim, K. J.; Kim, B.; Lee, H.; Kim, S., Covalent Functionalization of Epitaxial Graphene by Azidotrimethylsilane. *J. Phys. Chem. C* 2009**,** *113* (22), 9433-9435.

62. Strom, T. A.; Dillon, E. P.; Hamilton, C. E.; Barron, A. R., Nitrene addition to exfoliated graphene: a one-step route to highly functionalized graphene. *Chem. Commun.* 2010**,** *46* (23), 4097-4099.

63. Ismaili, H.; Geng, D. S.; Sun, A. X. L.; Kantzas, T. T.; Workentin, M. S., Light-Activated Covalent Formation of Gold Nanoparticle Graphene and Gold Nanoparticle-Glass Composites. *Langmuir* 2011**,** *27* (21), 13261-13268.

64. Zhong, X.; Jin, J.; Li, S. W.; Niu, Z. Y.; Hu, W. Q.; Li, R.; Ma, J. T., Aryne cycloaddition: highly efficient chemical modification of graphene. *Chem. Commun.* 2010**,** *46* (39), 7340-7342.

65. Sarkar, S.; Bekyarova, E.; Niyogi, S.; Haddon, R. C., Diels-Alder Chemistry of Graphite and Graphene: Graphene as Diene and Dienophile. *J. Am. Chem. Soc.* 2011**,** *133* (10), 3324-3327.

66. Georgakilas, V.; Bourlinos, A. B.; Zboril, R.; Steriotis, T. A.; Dallas, P.; Stubos, A. K.; Trapalis, C., Organic functionalisation of graphenes. *Chem. Commun.* 2010**,** *46* (10), 1766-1768.

67. Yu, D. S.; Yang, Y.; Durstock, M.; Baek, J. B.; Dai, L. M., Soluble P3HT-Grafted Graphene for Efficient Bilayer-Heterojunction Photovoltaic Devices. *Acs Nano* 2010**,** *4* (10), 5633-5640.

68. Melucci, M.; Durso, M.; Zambianchi, M.; Treossi, E.; Xia, Z. Y.; Manet, I.; Giambastiani, G.; Ortolani, L.; Morandi, V.; De Angelis, F.; Palermo, V., Graphene-organic hybrids as processable, tunable platforms for pH-dependent photoemission, obtained by a new modular approach. *J. Mater. Chem.* 2012**,** *22* (35), 18237-18243.

69. Park, S.; Dikin, D. A.; Nguyen, S. T.; Ruoff, R. S., Graphene Oxide Sheets Chemically Cross-Linked by Polyallylamine. *J. Phys. Chem. C* 2009**,** *113* (36), 15801-15804.

70. Gong, X. Z.; Liu, G. Z.; Li, Y. S.; Yu, D. Y. W.; Teoh, W. Y., Functionalized-Graphene Composites: Fabrication and Applications in Sustainable Energy and Environment. *Chem. Mat.* 2016**,** *28* (22), 8082-8118.

71. Hao, R.; Qian, W.; Zhang, L. H.; Hou, Y. L., Aqueous dispersions of TCNQ-anion-stabilized graphene sheets. *Chem. Commun.* 2008**,** (48), 6576-6578.

72. Bai, H.; Xu, Y. X.; Zhao, L.; Li, C.; Shi, G. Q., Non-covalent functionalization of graphene sheets by sulfonated polyaniline. *Chem. Commun.* 2009**,** (13), 1667-1669.

73. Hong, W. J.; Xu, Y. X.; Lu, G. W.; Li, C.; Shi, G. Q., Transparent graphene/PEDOT-PSS composite films as counter electrodes of dye-sensitized solar cells. *Electrochem. Commun.* 2008**,** *10* (10), 1555-1558.

74. Cui, Y.; Kim, S. N.; Jones, S. E.; Wissler, L. L.; Naik, R. R.; McAlpine, M. C., Chemical Functionalization of Graphene Enabled by Phage Displayed Peptides. *Nano Lett.* 2010**,** *10* (11), 4559-4565.

75. Wang, Y.; Li, Z. H.; Wang, J.; Li, J. H.; Lin, Y. H., Graphene and graphene oxide: biofunctionalization and applications in biotechnology. *Trends Biotechnol.* 2011**,** *29* (5), 205-212.

76. Myung, S.; Solanki, A.; Kim, C.; Park, J.; Kim, K. S.; Lee, K. B., Graphene-Encapsulated Nanoparticle-Based Biosensor for the Selective Detection of Cancer Biomarkers. *Adv. Mater.* 2011**,** *23* (19), 2221.

77. Bressan, E.; Ferroni, L.; Gardin, C.; Sbricoli, L.; Gobbato, L.; Ludovichetti, F. S.; Tocco, I.; Carraro, A.; Piattelli, A.; Zavan, B., Graphene based scaffolds effects on stem cells commitment. *J. Transl. Med.* 2014**,** *12*, 15.

78. Zhang, L. M.; Xia, J. G.; Zhao, Q. H.; Liu, L. W.; Zhang, Z. J., Functional Graphene Oxide as a Nanocarrier for Controlled Loading and Targeted Delivery of Mixed Anticancer Drugs. *Small* 2010**,** *6* (4), 537-544.

79. Reuven, D. G.; Shashikala, H. B. M.; Mandal, S.; Williams, M. N. V.; Chaudhary, J.; Wang, X. Q., Supramolecular assembly of DNA on graphene nanoribbons. *J. Mat. Chem. B* 2013**,** *1* (32), 3926-3931.

80. Liu, M. K.; Tjiu, W. W.; Pan, J. S.; Zhang, C.; Gao, W.; Liu, T. X., One-step synthesis of graphene nanoribbon-MnO2 hybrids and their all-solid-state asymmetric supercapacitors. *Nanoscale* 2014**,** *6* (8), 4233-4242.

81. Zhang, C. G.; Peng, Z. W.; Lin, J.; Zhu, Y.; Ruan, G. D.; Hwang, C. C.; Lu, W.; Hauge, R. H.; Tour, J. M., Splitting of a Vertical Multiwalled Carbon Nanotube Carpet to a Graphene Nanoribbon Carpet and Its Use in Supercapacitors. *Acs Nano* 2013**,** *7* (6), 5151-5159.

82. Lin, J.; Raji, A. R. O.; Nan, K. W.; Peng, Z. W.; Yan, Z.; Samuel, E. L. G.; Natelson, D.; Tour, J. M., Iron Oxide Nanoparticle and Graphene Nanoribbon Composite as an Anode Material for High- Performance Li-Ion Batteries. *Adv. Funct. Mater.* 2014**,** *24* (14), 2044-2048.

83. Vo, T. H.; Perera, U. G. E.; Shekhirev, M.; Pour, M. M.; Kunkel, D. A.; Lu, H. D.; Gruverman, A.; Sutter, E.; Cotlet, M.; Nykypanchuk, D.; Zahl, P.; Enders, A.; Sinitskii, A.; Sutter, P., Nitrogen-Doping Induced Self-Assembly of Graphene Nanoribbon-Based Two-Dimensional and Three-Dimensional Metamaterials. *Nano Lett.* 2015**,** *15* (9), 5770-5777.

84. Evaldsson, M.; Zozoulenko, I. V.; Xu, H. Y.; Heinzel, T., Edge-disorder-induced Anderson localization and conduction gap in graphene nanoribbons. *Phys. Rev. B* 2008**,** *78* (16), 4.

85. Barone, V.; Hod, O.; Scuseria, G. E., Electronic structure and stability of semiconducting graphene nanoribbons. *Nano Lett.* 2006**,** *6* (12), 2748-2754.

86. Ruffieux, P.; Cai, J. M.; Plumb, N. C.; Patthey, L.; Prezzi, D.; Ferretti, A.; Molinari, E.; Feng, X. L.; Mullen, K.; Pignedoli, C. A.; Fasel, R., Electronic Structure of Atomically Precise Graphene Nanoribbons. *Acs Nano* 2012**,** *6* (8), 6930-6935.

87. Huang, H.; Wei, D. C.; Sun, J. T.; Wong, S. L.; Feng, Y. P.; Castro Neto, A. H.; Wee, A. T. S., Spatially Resolved Electronic Structures of Atomically Precise Armchair Graphene Nanoribbons. *Sci Rep* 2012**,** *2*, 7.

88. Fujita, M.; Wakabayashi, K.; Nakada, K.; Kusakabe, K., Peculiar localized state at zigzag graphite edge. *J. Phys. Soc. Jpn.* 1996**,** *65* (7), 1920-1923.

89. Son, Y. W.; Cohen, M. L.; Louie, S. G., Half-metallic graphene nanoribbons. *Nature* 2006**,** *444* (7117), 347-349.

90. Huang, W.; Wang, J. S.; Liang, G. C. A., Theoretical study on thermoelectric properties of kinked graphene nanoribbons. *Phys. Rev. B* 2011**,** *84* (4), 7.

91. Wang, S. D.; Wang, J. L., Quasiparticle Energies and Optical Excitations in Chevron-Type Graphene Nanoribbon. *J. Phys. Chem. C* 2012**,** *116* (18), 10193-10197.

92. Han, M. Y.; Ozyilmaz, B.; Zhang, Y. B.; Kim, P., Energy band-gap engineering of graphene nanoribbons. *Phys. Rev. Lett.* 2007**,** *98* (20), 4.

93. Chen, Z. H.; Lin, Y. M.; Rooks, M. J.; Avouris, P., Graphene nano-ribbon electronics. *Physica E* 2007**,** *40* (2), 228-232.

94. Cho, S.; Kikuchi, K.; Kawasaki, A., Radial followed by longitudinal unzipping of multiwalled carbon nanotubes. *Carbon* 2011**,** *49* (12), 3865-3872.

95. Shinde, D. B.; Majumder, M.; Pillai, V. K., Counter-ion Dependent, Longitudinal Unzipping of Multi-Walled Carbon Nanotubes to Highly Conductive and Transparent Graphene Nanoribbons. *Sci Rep* 2014**,** *4*, 6.

96. Jiao, L. Y.; Zhang, L.; Wang, X. R.; Diankov, G.; Dai, H. J., Narrow graphene nanoribbons from carbon nanotubes. *Nature* 2009**,** *458* (7240), 877-880.

97. Safron, N. S.; Kim, M.; Gopalan, P.; Arnold, M. S., Barrier-Guided Growth of Micro- and Nano-Structured Graphene. *Adv. Mater.* 2012**,** *24* (8), 1041-1045.

98. Kato, T.; Hatakeyama, R., Site- and alignment-controlled growth of graphene nanoribbons from nickel nanobars. *Nat. Nanotechnol.* 2012**,** *7* (10), 651-656.

99. Liu, Z.; Ma, L. L.; Shi, G.; Zhou, W.; Gong, Y. J.; Lei, S. D.; Yang, X. B.; Zhang, J. N.; Yu, J. J.; Hackenberg, K. P.; Babakhani, A.; Idrobo, J. C.; Vajtai, R.; Lou, J.; Ajayan, P. M., In-plane heterostructures of graphene and hexagonal boron nitride with controlled domain sizes. *Nat. Nanotechnol.* 2013**,** *8* (2), 119-124.

100. Meng, N.; Fernandez, J. F.; Vignaud, D.; Dambrine, G.; Happy, H., Fabrication and Characterization of an Epitaxial Graphene Nanoribbon-Based Field-Effect Transistor. *IEEE Trans. Electron Devices* 2011**,** *58* (6), 1594-1596.

101. Tongay, S.; Lemaitre, M.; Fridmann, J.; Hebard, A. F.; Gila, B. P.; Appleton, B. R., Drawing graphene nanoribbons on SiC by ion implantation. *Appl. Phys. Lett.* 2012**,** *100* (7), 3.

102. Wang, X.; Zhang, Y. W.; Tang, M. X.; Han, D.; Fu, E. G.; Xue, J. M.; Zhao, Z. Q., Synthesis of ultra-thin carbon layers on SiC substrate by ion implantation. *Carbon* 2015**,** *93*, 230-241.

103. Dossel, L.; Gherghel, L.; Feng, X. L.; Mullen, K., Graphene Nanoribbons by Chemists: Nanometer-Sized, Soluble, and Defect-Free. *Angew. Chem.-Int. Edit.* 2011**,** *50* (11), 2540-2543.

104. Yang, X. Y.; Dou, X.; Rouhanipour, A.; Zhi, L. J.; Rader, H. J.; Mullen, K., Two-dimensional graphene nanoribbons. *J. Am. Chem. Soc.* 2008**,** *130* (13), 4216.

105. Mohanty, N.; Moore, D.; Xu, Z. P.; Sreeprasad, T. S.; Nagaraja, A.; Rodriguez, A. A.; Berry, V., Nanotomy-based production of transferable and dispersible graphene nanostructures of controlled shape and size. *Nat Commun.* 2012**,** *3*, 8.

106. Marcano, D. C.; Kosynkin, D. V.; Berlin, J. M.; Sinitskii, A.; Sun, Z. Z.; Slesarev, A.; Alemany, L. B.; Lu, W.; Tour, J. M., Improved Synthesis of Graphene Oxide. *Acs Nano* 2010**,** *4* (8), 4806-4814.

107. Frens, G., Controlled Nucleation for Regulation of Particle-Size in Monodisperse Gold Suspensions. *Nature* 1973**,** *241* (105), 20-22.

108. Britnell, L.; Gorbachev, R. V.; Jalil, R.; Belle, B. D.; Schedin, F.; Mishchenko, A.; Georgiou, T.; Katsnelson, M. I.; Eaves, L.; Morozov, S. V.; Peres, N. M. R.; Leist, J.; Geim, A. K.; Novoselov, K. S.; Ponomarenko, L. A., Field-Effect Tunneling Transistor Based on Vertical Graphene Heterostructures. *Science* 2012**,** *335* (6071), 947-950.

109. Wang, Y.; Liu, Z. S., The fracture toughness of graphene during the tearing process. *Model. Simul. Mater. Sci. Eng.* 2016**,** *24* (8), 14.

110. Wang, S. W.; Fan, Z. C.; Cui, Y.; Zhang, S. R.; Yang, B. C.; Chen, H. Y., Fracture behaviors of brittle and ductile 2D carbon structures under uniaxial tensile stress. *Carbon* 2017**,** *111*, 486-492.

111. Seo, Y.; Jhe, W., Atomic force microscopy and spectroscopy. *Rep. Prog. Phys.* 2008**,** *71* (1), 23.

112. Williams, D. B.; Carter, C. B., The Transmission Electron Microscope. In *Transmission Electron Microscopy: A Textbook for Materials Science*, Springer US: Boston, MA, 2009; pp 3-22.

113. Fultz, B.; Howe, J. M., High-Resolution TEM Imaging. In *Transmission Electron Microscopy and Diffractometry of Materials*, Springer Berlin Heidelberg: Berlin, Heidelberg, 2008; pp 517-582.

114. Maslova, M. V.; Gerasimova, L. G.; Forsling, W., Surface properties of cleaved mica. *Colloid J.* 2004**,** *66* (3), 322-328.

115. Xu, P.; Yang, Y.; Barber, S. D.; Ackerman, M. L.; Schoelz, J. K.; Kornev, I. A.; Barraza-Lopez, S.; Bellaiche, L.; Thibado, P. M., Giant surface charge density of graphene resolved from scanning tunneling microscopy and first-principles theory. *Phys. Rev. B* 2011**,** *84* (16), 5.

116. Klar, P.; Casiraghi, C., Raman spectroscopy of graphene in different dielectric solvents. In *Physica Status Solidi C, Vol 7, No 11-12*, Correia, A.; Saenz, J. J.; Ordejon, P.; Roche, S., Eds. Wiley-V C H Verlag Gmbh: Weinheim, 2010; Vol. 7, pp 2735-2738.

117. Casiraghi, C.; Hartschuh, A.; Qian, H.; Piscanec, S.; Georgi, C.; Fasoli, A.; Novoselov, K. S.; Basko, D. M.; Ferrari, A. C., Raman Spectroscopy of Graphene Edges. *Nano Lett.* 2009**,** *9* (4), 1433-1441.

118. Ferrari, A. C., Raman spectroscopy of graphene and graphite: Disorder, electron-phonon coupling, doping and nonadiabatic effects. *Solid State Commun.* 2007**,** *143* (1-2), 47-57.

119. Dykstra, H. M. *At the Cutting Edge: Structural Analysis and Chemical Modification of the Edges of Mechanically Cleaved Graphene Nanoribbons* (Unpublished doctoral thesis). Massey University, Manawatu, New Zealand, 2017.

120. Smith, B. C., The Benzene Fingers, Part II: Let Your Fingers Do the Walking Through the Benzene Fingers. *Spectroscopy* 2016**,** *31* (9), 30-33.

121. Smith, B. C., IR Spectral Interpretation Workshop. The Infrared Spectroscopy of Alkenes. *Spectroscopy* 2016**,** *31* (11), 28.

122. SDBSWeb: http://sdbs.db.aist.go.jp (National Institute of Advanced Industrial Science and Technology) (accessed 5/1/2017).

123. Dannenberg, J. J., An Introduction to Hydrogen Bonding By George A. Jeffrey (University of Pittsburgh). Oxford University Press: New York and Oxford. 1997. ISBN 0-19-509549-9.

124. Mak, K. F.; Ju, L.; Wang, F.; Heinz, T. F., Optical spectroscopy of graphene: From the far infrared to the ultraviolet. *Solid State Commun.* 2012**,** *152* (15), 1341-1349.

125. O'Neill, A.; Khan, U.; Nirmalraj, P. N.; Boland, J.; Coleman, J. N., Graphene Dispersion and Exfoliation in Low Boiling Point Solvents. *J. Phys. Chem. C* 2011**,** *115* (13), 5422-5428.

126. Khan, U.; O'Neill, A.; Lotya, M.; De, S.; Coleman, J. N., High-Concentration Solvent Exfoliation of Graphene. *Small* 2010**,** *6* (7), 864-871.

127. Lotya, M.; King, P. J.; Khan, U.; De, S.; Coleman, J. N., High-Concentration, Surfactant-Stabilized Graphene Dispersions. *Acs Nano* 2010**,** *4* (6), 3155-3162.

128. Zhu, S. E.; Yuan, S. J.; Janssen, G., Optical transmittance of multilayer graphene. *Epl* 2014**,** *108* (1), 4.

129. Kim, H. H.; Yang, J. W.; Jo, S. B.; Kang, B.; Lee, S. K.; Bong, H.; Lee, G.; Kim, K. S.; Cho, K., Substrate-Induced Solvent Intercalation for Stable Graphene Doping. *Acs Nano* 2013**,** *7* (2), 1155-1162.

130. Wang, K. Q.; Dong, J.; Sun, L. P.; Chen, H. Y.; Wang, Y.; Wang, C. X.; Dong, L. F., Effects of elemental doping on the photoluminescence properties of graphene quantum dots. *RSC Adv.* 2016**,** *6* (94), 91225-91232.

131. Polyakova, E. Y.; Rim, K. T.; Eom, D.; Douglass, K.; Opila, R. L.; Heinz, T. F.; Teplyakov, A. V.; Flynn, G. W., Scanning Tunneling Microscopy and X-ray Photoelectron Spectroscopy Studies of Graphene Films Prepared by Sonication-Assisted Dispersion. *Acs Nano* 2011**,** *5* (8), 6102-6108.

132. Johnson, D. W.; Dobson, B. P.; Coleman, K. S., A manufacturing perspective on graphene dispersions. *Curr. Opin. Colloid Interface Sci.* 2015**,** *20* (5-6), 367-382.

133. Skaltsas, T.; Ke, X. X.; Bittencourt, C.; Tagmatarchis, N., Ultrasonication Induces Oxygenated Species and Defects onto Exfoliated Graphene. *J. Phys. Chem. C* 2013**,** *117* (44), 23272-23278.

134. Chabot, V.; Kim, B.; Sloper, B.; Tzoganakis, C.; Yu, A. P., High yield production and purification of few layer graphene by Gum Arabic assisted physical sonication. *Sci Rep* 2013**,** *3*, 7.

135. Narayan, R.; Kim, S. O., Surfactant mediated liquid phase exfoliation of graphene. *Nano Convergence* 2015**,** *2* (1), 20.

136. Xue, Y. R.; Li, X.; Li, H. B.; Zhang, W. K., Quantifying thiol-gold interactions towards the efficient strength control. *Nat. Commun.* 2014**,** *5*, 9.

137. Hong, W. J.; Bai, H.; Xu, Y. X.; Yao, Z. Y.; Gu, Z. Z.; Shi, G. Q., Preparation of Gold Nanoparticle/Graphene Composites with Controlled Weight Contents and Their Application in Biosensors. *J. Phys. Chem. C* 2010**,** *114* (4), 1822-1826.

138. Wang, Q.; Wang, Q.; Li, M. S.; Szunerits, S.; Boukherroub, R., One-step synthesis of Au nanoparticle-graphene composites using tyrosine: electrocatalytic and catalytic properties. *New J. Chem.* 2016**,** *40* (6), 5473-5482.

139. Torres-Mendieta, R.; Ventura-Espinosa, D.; Sabater, S.; Lancis, J.; Minguez-Vega, G.; Mata, J. A., In situ decoration of graphene sheets with gold nanoparticles synthetized by pulsed laser ablation in liquids. *Sci Rep* 2016**,** *6*, 9.

140. Khalil, I.; Julkapli, N. M.; Yehye, W. A.; Basirun, W. J.; Bhargava, S. K., Graphene-Gold Nanoparticles Hybrid-Synthesis, Functionalization, and Application in a

Electrochemical and Surface-Enhanced Raman Scattering Biosensor. *Materials* 2016**,** *9* (6), 38.

141. Bai, S.; Shen, X. P., Graphene-inorganic nanocomposites. *RSC Adv.* 2012**,** *2* (1), 64-98.

142. Lee, J. U.; Lee, W.; Yoon, S. S.; Kim, J.; Byun, J. H., Site-selective immobilization of gold nanoparticles on graphene sheets and its electrochemical properties. *Appl. Surf. Sci.* 2014**,** *315*, 73-80.

143. Software for Chemistry and Materials (SCM). *ADF Modeling Suite* 2016, www.scm.com/adf-modeling-suite/

144. Flynn, C. E.; Lee, S. W.; Peelle, B. R.; Belcher, A. M., Viruses as vehicles for growth, organization and assembly of materials. *Acta Materialia* 2003**,** *51* (19), 5867-5880.

145. Rakonjac, J.; Bennett, N. J.; Spagnuolo, J.; Gagic, D.; Russel, M., Filamentous Bacteriophage: Biology, Phage Display and Nanotechnology Applications. *Curr. Issues Mol. Biol.* 2011**,** *13* (2), 51-75.

146. Zimmermann, K.; Hagedorn, H.; Heuck, C. C.; Hinrichsen, M.; Ludwig, H., The Ionic Properties of the filamentous bacteriophages Pf1 and fd. *J. Biol. Chem.* 1986**,** *261* (4), 1653-1655.